Dissertation

submitted to the
Combined Faculties for the Natural Sciences and for Mathematics
of the Ruperto-Carola University of Heidelberg, Germany
for the degree of
Doctor of Natural Sciences

presented by
Specialist in Biochemistry Yury Bykov
born in: Moscow, U.S.S.R
Oral examination: December 12, 2017

Development and application of electron microscopy methods for endocytic-secretory pathway studies in cells

Referees: Dr. Anne-Claude Gavin
Prof. Dr. Michael Knop

Summary

Electron microscopy (EM) and tomography provides the most detailed view of the cellular ultrastructure and can be further extended to the structural level using cryogenic electron tomography. Fluorescent microscopy (FM) is used to complement this data with molecular identity information in a wide range of correlative microscopy techniques. In this thesis I present my work on the development of the correlative microscopy methods as well as the application of new and established electron microscopy methods to the study of the endocytic and secretory pathways.

I developed a sample parallelization approach based on the fluorescent barcoding of budding yeast cells that allows high-throughput screening of yeast mutants using EM. Cells from different strains or under different conditions are grown in parallel and then subjected to combinatorial labeling with fluorescent dyes. Labeled cells are mixed together to generate a single sample which is subjected to high-pressure freezing, freeze-substitution and sectioning. The sections are imaged with FM and EM. FM data is used to determine the fluorescent barcode of each cell and thus its strain identity or experimental conditions, and high-resolution EM data can be collected in parallel for each of the strains or conditions. The total time spent on embedding and sectioning can be reduced up to 30 times using the developed protocol. I demonstrate the utility of the method by analyzing the variation of total multivesicular body volume (MVB) in different yeast strains.

As a part of the collaborative project investigating the role of the ATPase Vps4 in the formation of MVBs, I performed correlative FM and electron tomography of MVBs containing Vps4. It showed that MVBs correlating with the Vps4 signal usually form clusters of more than one organelle and that the Vps4 signal correlates with MVBs actively forming intraluminal vesicles.

Finally, I used subtomogram averaging to determine the COPI coat structure *in situ,* within its native cellular environment. I analyzed a tomographic dataset of cryo-lamella prepared by collaborators using focused ion beam milling of vitrified *Chlamydomonas reinhardtii* cells. I determined the COPI coat structure *de novo* and analyzed its variability during uncoating and within the Golgi stack. The COPI coat preserved its structure and stoichiometry during uncoating and in different Golgi regions. However the density of bound dilysine cargo and membrane thickness varied along the stack.

In this thesis I have applied different EM methods to investigate morphological and structural aspects of the endocytic-secretory pathway. In the future such an integrative EM approach, ranging from functional genetic screens to structure determination, can be used to address multiple questions in cell biology.

Zusammenfassung

Elektronenmikroskopie (EM) und Tomographie ermöglichen es sub-zelluläre Strukturen hoch detailliert abzubilden und unter der Verwendung von Kryo-Elektronenmikroskopie können selbst Strukturen auf Proteinebene sichtbar gemacht werden. In korrelativen Methoden werden EM Daten mit Fluoreszenzmikroskopie (FM) Daten erweitert, um Moleküle spezifisch identifizieren zu können. In dieser Doktorarbeit stelle ich die Entwicklung einer neuen korrelativer Methode und deren Anwendung vor. Des Weiteren habe ich existierende EM Methoden verwendet, um endozytische und sekretorische Vorgänge zu analysieren.

Basierend auf der Idee im Hochdurchsatzverfahren Tests an Hefemutanten in EM durchzuführen, wie es in der FM möglich ist, habe ich einen Ansatz entwickelt, der auf der Verwendung fluoreszierender Barcodes in knospenden Hefezellen beruht. Hierzu werden Zellen unterschiedlicher Hefestämme oder unterschiedlicher Wachstumsbedingungen parallel herangezogen und anschließend kombinatorisch fluoreszierend markiert. Markierte Zellen werden dann in einer Probe kombiniert, hochdruckgefroren, gefriersubstituiert, als Dünnschnitte präpariert und dann sowohl im FM als auch im EM analysiert. Während die FM Daten verwendet werden, um über den Barcode den Stamm oder die Wachstumsbedingung zu identifizieren, werden für alle Bedingungen parallel hochaufgelöste EM Bilder aufgenommen. So kann die gesamte Präparationszeit für das Einbetten und Schneiden der Proben um ein 30-faches reduziert werden. Die Vorteile des Protokolls werden hier anhand der Variation des totalen Volumens multivesikulärer Körperchen (MVB) verschiedener Hefestämme demonstriert.

Als Teil eines Kollaborationsprojektes, mit dem Ziel die Rolle der ATPase Vsp4 bei der Bildung von MVBs zu untersuchen, habe ich MVBs, die Vps4 beinhalten, korrelativ untersucht. Diese Versuche haben ergeben, dass MVBs, die mit dem Vps4 Signal korrelieren, Anhäufungen von mehr als einem Organell aufweisen und dass das Vps4 Signal mit MVBs korreliert, die aktiv intraluminale Vesikel formen.

Als Teil eines weiteren Kollaborationsprojektes, habe ich Subtomogram Averaging verwendet, um die COPI Struktur in seiner nativen Umgebung zu bestimmen. Dazu habe ich tomographische Aufnahmen von Kryo-Lamellen analysiert. Zur Lamellenherstellung wurden *Chlamydomonas reinhardtii* Zellen vitrifiziert und im Anschluss Material mit Hilfe eines fokussierten Ionenstrahls abgetragen. Die COPI Struktur wurde *de novo* bestimmt und die strukturelle Variabilität für verschiedene Stadien der Vesikelentmantelung und innerhalb des Golgi Apparates analysiert. Es wurde gezeigt, dass COPI seine Struktur und Stöchiometrie während der Entmantelung und in verschiedenen Golgi Regionen behält. Allerdings verändern sich die Dichte gebundener Dilysin Cargos und die Membrandicke entlang der Golgi Stapel.

Zusammenfassend habe ich in dieser Arbeit verschiedene EM Methoden verwendet um morphologische und strukturelle Aspekte endozytisch-sekretorischer Vorgänge zu untersuchen. Zukünftig, können solche integrativen EM Ansätze, die von funktionalen genetischen Tests bis zur Proteinstrukturbestimmung reichen, verwendet werden, um verschiedenste zellbiologische Fragen zu beantworten.

Table of contents

Summary **1**

Zusammenfassung **2**

Table of contents **3**

Abbreviations **6**

Chapter 1. A review of correlative light and electron microscopy methods **9**

1.1 Introduction **9**

1.2 EM Sample Preparation **10**

1.2.1 Fixation 10

1.2.2 Embedding 13

1.2.3 Sectioning 14

1.2.4 Imaging 16

1.3 The diversity of correlative microscopy workflows **18**

1.3.1 Pre-embedding LM 19

1.3.2 Post-embedding LM 21

1.3.3 No-embedding LM (cryo-CLEM) 25

Chapter 2. High-throughput correlative light and electron microscopy of budding yeast by fluorescent barcoding **27**

2.1. Introduction **27**

2.2. General considerations **30**

2.3 Staining protocol development **31**

2.4 The staining protocol **35**

2.4.1 Materials and equipment 35

2.4.2 Yeast cultures 35

2.4.3 Staining solution preparation 36

2.4.4 Staining and freezing 38

2.5. Combining barcoding with a conventional CLEM experiment **39**

2.6. Image processing pipeline development **40**

2.7. Proof of principle experiment **43**

2.7.1 Experiment design 43

2.7.2. Overall ultrastructure comparison 43

2.7.3 MVB morphology quantification: Results 47
2.7.4 MVB morphology quantification: Discussion 49
2.8 Conclusion and Perspectives 50
2.9 Materials and Methods 51
2.9.1. Yeast strains 51
2.9.2. Cell growth 53
2.9.3 Staining 53
2.9.4 EM sample preparation 54
2.9.5 Fluorescence microscopy 54
2.9.6 Electron microscopy 56
2.9.7 Image analysis and correlation 56
2.9.8 Multivesicular body morphometry 58
Chapter 3. Ultrastructural analysis of multivesicular body biogenesis using correlative light microscopy and electron tomography 61
3.1 Introduction 61
3.2 Materials and Methods 66
3.2.1 Yeast strains 66
3.2.2 Correlative Light and Electron Microscopy 67
3.2.3 MVBs morphology measurements 68
3.3 Results 69
3.3.1 Fluorescence preservation after embedding 69
3.3.2 MVBs associate with each other and with other organelles 71
3.3.3 ILV formation quantification 72
3.3.4 3D modeling of MVBs 73
3.3.5 The geometrical model of MVB formation 73
3.4 Discussion 76
3.4.1 The role of Vps4 in the MVB biogenesis 76
3.4.2 Yeast endosome maturation and morphology 77
Chapter 4. *In situ* structural analysis of the *Chlamydomonas reinhardtii* COPI coat 83
4.1 Introduction 83
4.2 Results 87
4.2.1 The structure of the assembled COPI coat in cells 87
4.2.2 The arrangement of the COPI coat on buds and vesicles 91

4.2.3 Budding and uncoating of COPI vesicles 93
4.2.4 Variations of vesicle and cisternae morphology in the Golgi 97
4.2.6 Measurement of bilayer leaflet separation in COPI vesicles, and buds 100
4.2.7 Measurement of bilayer leaflet separation in uncoated Golgi membranes 101
4.3 Discussion 103
4.3.1 *In vitro* reconstitution of COPI budding mimics the structure determined in cell 103
4.3.2 The morphology of COPI coated vesicles changes through the stack, but the structure does not 103
4.3.3 The assembly and disassembly cycle of the COPI coated vesicle 104
4.3.4 The power of *in situ* structural biology 105
4.4 Materials and Methods 105
4.4.1 Sample preparation and electron tomography 105
4.4.2 Subtomogram averaging 106
4.4.3 Lattice map and linkage structure analysis 108
4.4.4 Measurement of vesicle coat completeness 108
4.4.5 Morphological annotation and structure variation analysis 109
4.4.6 Measurement of membrane thickness in vesicles and buds 110
4.4.7 Measurement of membrane thickness in Golgi cisternae 110
Chapter 5. Conclusions and perspectives 113
5.1 Increasing throughput of plastic EM 113
5.2 MVB morphology by CLEM tomography 115
5.3 *In situ* structural analysis of the COPI coat 115
5.4 The future of correlative microscopy 117
List of Figures 121
List of Tables 122
List of publications 123
References 125
Acknowledgements 140

Abbreviations

2D – Two-dimensional

3D – Three-dimensional

CEMOVIS – Cryogenic electron microscopy of vitreous sections

CLASI-FISH - combinatorial labeling and spectral imaging fluorescent *in situ* hybridization

CLEM – Correlative light and electron microscopy

Con a – Concanavalin a

COPI – Coat protein 1

COPII – Coat protein 2

CORVET – class C core vacuole/endosome tethering

DMSO – dimethyl sulfoxide

EE – Early endosome

EGFP – Enhanced green fluorescent protein

EM – Electron microscopy

ER – Endoplasmic reticulum

ESCRT – Endosomal protein sorting required for transport

ET – Electron tomography

FCB – Fluorescent cell barcoding

FIB – Focused ion beam

FM – Fluorescence microscopy

FS – Freeze-substitution

GA - Glutaraldehyde

GAP – Guanosine triphosphate hydrolase activating protein

GDP – Guanosine diphosphate

GEF – Guanine exchange factor

GFP – Green fluorescent protein

GTP – Guanosine triphosphate

GTPase – Guanosine triphosphate hydrolase

HOPS – Homotypic fusion and protein sorting

HPF – High-pressure freezing

ILV – Intraluminal vesicle

LE – Late endosome

LM – Light microscopy

MVB – Multivesicular body

NHS – N-hydroxysuccinimide

PBS – Phosphate buffered saline

PDB – Protein data bank

PFA – Paraformaldehyde

PtdIns(3,5)P(2) – Phosphatidylinositol 3,5-biphosphate

PtdIns(3)P – Phosphatidylinositol 3-phosphate

SBSEM – serial blockface scanning electron microscopy

SC – Synthetic complete media

SD – Synthetic depleted media

SEM – Scanning electron microscopy

SMLM – Single molecule localization microscopy

SNARE – soluble N-ethylmaleimide-sensitive factor attachment protein receptor

TEM – Transmission electron microscope

TGN – trans Golgi network

TRITC – Tetramethylrhodamine

Chapter 1. A review of correlative light and electron microscopy methods

1.1 Introduction

Light and electron microscopy are the two main tools of cell biology. The information they give is complementary, and they are often used in combination to study a particular question. Recently a lot of effort was spent to apply both methods to the same sample and gain some additional benefits from that. Such combination is usually termed correlative light and electron microscopy (CLEM).

Electron microscopy provided cell biologists with a detailed picture of cellular ultrastructure revealing its immense complexity (Walker, 2014). This method allows imaging of all organelles stained in an unspecific way with membranes, large protein complexes and nucleic acids giving the highest contrast depending on specimen preparation protocol. Such advantages come together with certain requirements and limitations: the sample should be sufficiently thin to allow the electron beam penetration (usually <500 nm), ultrastructure should be preserved close to the native state, heavy metals should be introduced in the sample to provide enough contrast deflecting the electrons, and the sample should be stable in the high vacuum of the microscope column. Data acquired with an electron microscope usually represent 2D projections of very small static cell volumes 50-500 nm thick and few microns wide. This means that getting the accurate representation of cellular ultrastructure in 3D will require selection of an appropriate imaging strategy

(serial sections, tomography or other). Another major limitation of EM is that although the general ultrastructure is well visualized, highlighting one particular protein is challenging. Genetically encoded electron-dense labels are in early stages of development and immunogold labeling is possible only on the section surface.

Light microscopy (LM) allows very specific labeling of particular components on the whole living cells. The field of view of the light microscope is much larger than that of the EM. Although the resolution limitation of LM was overcome with the introduction of new techniques, the obtained information lacks cellular context.

CLEM aims to combine the advantages of LM and EM, and is used for three basic reasons: (1) localize a rare event because EM field of view is very much smaller than that of LM, (2) complement live imaging with ultrastructural information, and (3) provide molecular specificity for EM imaging.

In this Chapter, I review most popular workflows for biological EM sample preparation and imaging with electron microscopy focusing on transmission electron microscopy (TEM). Then I review different strategies for introducing a light microscope in the workflow (Fig 1.1). The text of this Chapter was written by myself and published as a part of a review article (Bykov *et al.*, 2016), and is reproduced here with the permission from Wiley and Sons (license number 4187230475800).

1.2 EM Sample Preparation

1.2.1 Fixation

The first step in sample preparation aims to kill the cell and stabilize its components preserving it as close to the native state as possible. Most commonly used methods are chemical fixation and freezing made either under high pressure (HPF) or very quickly (plunge-freezing).

Chemical fixation is made at room temperature and does not require any special equipment. The size of the sample can be relatively large compared to

the freezing methods. Usually, a combination of glutaraldehyde (GA) and osmium tetroxide is used as a fixative (Bozzola, 2014). These chemicals crosslink and denature cellular components preserving the general ultrastructure. Osmium is also a contrasting agent due to its high electron density. The specimen quality achieved by this type of fixation can vary depending on the studied sample (Frankl *et al.*, 2015).

High-pressure freezing is performed using dedicated machines, which pressurize the sample and cool it down to liquid nitrogen temperature within few milliseconds (McDonald, 2007). This prevents ice crystal formation, instead, water forms amorphous ice and the sample is preserved in the so-called vitreous state (Moor, 1987). All cellular components are immobilized exactly like they were in the living cell. This method provides samples of the highest quality (Murk *et al.*, 2003). Frozen specimens should be further handled at cryo-temperatures or embedded into a resin to be processed at room temperature. The sample size is usually limited to 3-6 mm diameter and few hundred of micron thickness depending on the particular setup.

Plunge-freezing is one of the alternative ways for getting a vitreous sample. The sample is applied on electron microscopy grid and plunged in the liquid ethane maintained at cryogenic temperature. In such setup, the heat transfer is so fast that water does not have time to assemble into ice crystals and forms amorphous ice (Adrian *et al.*, 1984). Efficient cooling is achieved for samples thinner than 15 µm, which can be protein solution, purified virus or cells grown directly on EM grids. Sample regions thinner than 500 nm can be directly visualized with cryo-TEM, thicker regions can be further thinned using cryogenic focused ion beam (cryo-FIB) milling procedure (Rigort *et al.*, 2012a). Plunge-freezing can be performed on a simple home-made device, but commercial systems giving more reproducible results also exist. There are other methods of fast freezing including self-pressurized freezing, and propane jet freezing (Sitte *et al.*, 1987; Leunissen and Yi, 2009), but these are not very widely used and are not described here.

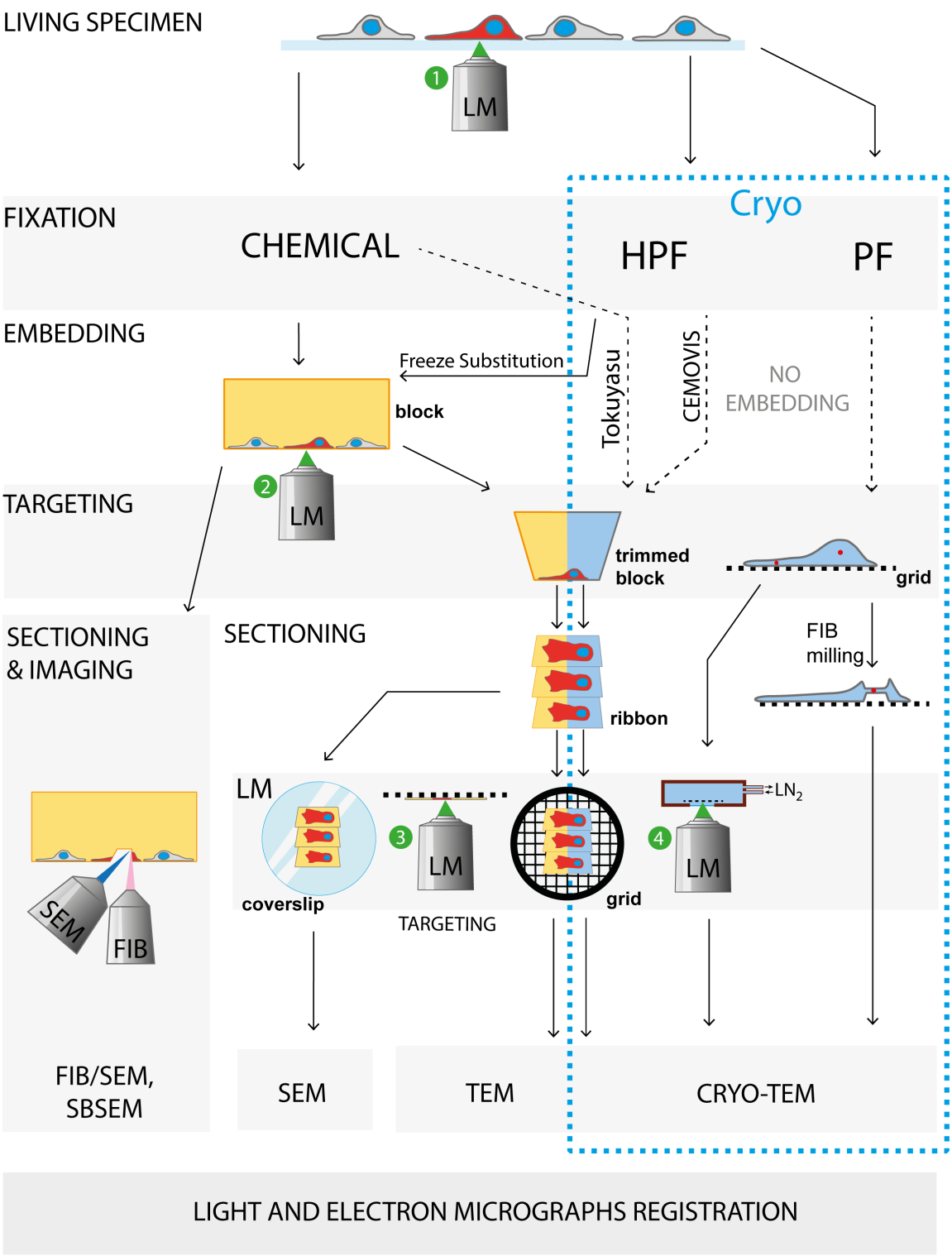
LIVING SPECIMEN
LM
Cryo
FIXATION
CHEMICAL
HPF
PF
EMBEDDING
Freeze Substitution
Tokuyasu
CEMOVIS
NO
EMBEDDING
block
TARGETING
LM
trimmed
block
grid
SECTIONING
& IMAGING
SECTIONING
FIB
milling
ribbon
LM
LN2
coverslip
LM
grid
LM
TARGETING
SEM
FIB
FIB/SEM,
SBSEM
SEM
TEM
CRYO-TEM
LIGHT AND ELECTRON MICROGRAPHS REGISTRATION

Fig. 1.1. EM sample preparation workflow with various strategies for LM incorporation. The most common EM sample preparation techniques are depicted leading from living sample to final micrograph registration step. First, the sample is fixed either chemically at room temperature or with High-Pressure freezing (HPF) or plunge-freezing (PF). HPF and PF fixed samples can be further processed at cryo- conditions (CEMOVIS, FIB-milling, or direct imaging). Chemically fixed cells can be embedded in resin or cut at cryo-conditions using Tokuyasu method to avoid embedding. HPF-fixed cells can in turn be embedded using freeze-substitution protocol to be processed at room temperature. The block is trimmed to remove the unwanted material and focus on the region of interest aided by reference marks or light microscopy. Embedded specimens are thinned with microtome and mounted on grids or coverslip and imaged with TEM or SEM. Light microscopy data are used to target the acquisition. Alternatively thinning and imaging can be done simultaneously in FIB/SEM or SBSEM instrument. At the end both datasets can be overlaid with different extent of precision. Various strategies of LM incorporation are shown: 1 —LM on living or prefixed sample, 2—LM on entire block of embedded specimen, 3—LM on sections at room temperature, or 4—cryo-LM on vitreous sections or whole vitrified cells. Further details are given in the text. Reproduced with permission from (Bykov *et al.*, 2016).

1.2.2 Embedding

After fixation, biological samples are not hard enough for thin sectioning (ultramicrotomy) and also have liquid water, which will evaporate in the vacuum of the electron microscope. That's why they are dehydrated through successive exposure to different solvents, which eventually are substituted to the liquid resin polymerized afterward. Resin tightly crosslinks the sample, substitutes the low-molecular weight components and provides additional contrast. This processing step yields a block of plastic that needs to be trimmed and sectioned before microscopy (Fig. 1.1).

High-pressure frozen samples are sufficiently hard to be sectioned at cryogenic conditions (Al-Amoudi *et al.*, 2004). They can also be embedded using the freeze-substitution (FS) procedure. For this frozen sample is transferred into the cold acetone solution containing fixative and contrasting agents (glutaraldehyde, uranyl acetate, and osmium tetroxide). Water is substituted with acetone and the sample is slowly warmed up allowing fixatives to interact with it. Acetone is substituted with the resin solution, which is polymerized afterward. Fixation at low temperature preserves the native membrane shapes and ultrastructure immobilized by high-pressure freezing (Steinbrecht and Müller, 1987; McDonald, 2007).

Resins have different chemical nature and provide various possibilities. Most popular epoxy resin Epon gives very hard samples with excellent contrast but most proteins in those are denatured and any immunolocalization experiments are not possible (McDonald, 2007; Frankl *et al.*, 2015). Methacrylate-based resins LR White and Lowicryl give less contrast and softer blocks, which are more difficult to handle. The structure of these resins allows preservation of some proteins and their localization with antibodies (Monaghan *et al.*, 1998).

An alternative approach for epitope preservation is to avoid the resin embedding completely. This is implemented in Tokuyasu method and its variations (Tokuyasu, 1973). The chemically fixed sample is infiltrated with sucrose for cryoprotection and frozen in liquid nitrogen. The resulting block is sectioned at low temperature. Sections are collected on grids and warmed up again for immunolabelling, which is very efficient with this approach, although ultrastructure preservation is worse than in embedded samples.

1.2.3 Sectioning

Microtomy should be targeted to the region of interest. In conventional EM sample preparation, this targeting and trimming step has different importance depending on the experimental object, but in CLEM this can be a very crucial step in the whole workflow (see below) (Kolotuev *et al.*, 2012). After all unwanted parts of the resin block are removed the remaining resin pyramid is sectioned. The section thickness depends on the desired EM imaging strategy. A series of successive ultrathin sections (50-100 nm) can be collected for 2D imaging or 3D reconstruction by alignment of successive images. Semi-thick sections (100-500 nm) are collected for electron tomography. Sectioning of resin embedded samples at room temperature is mostly free of any artifacts and can be done relatively quickly.

Microtomy at cryogenic temperatures is more challenging. Cryo-electron microscopy of vitreous sections (CEMOVIS) has significantly lower throughput than room temperature methods: the section size is smaller and

the process is slower. Various artifacts are introduced during sectioning (Al-Amoudi *et al.*, 2002, 2005; Dubochet *et al.*, 2007). However, method development continues in this area and some equipment is available that makes the process easier (Ladinsky, 2010; Pierson *et al.*, 2010; Studer *et al.*, 2014). For some samples, this remains the only method which allows imaging those in the most native state.

After microtomy, the section ribbons are applied on EM grids. A glass coverslip can be also used if the studied question can be addressed by scanning electron microscopy (SEM). Sections are post-stained with heavy metals (uranyl acetate and lead citrate are usually used). Analysis of consecutive sections by SEM and LM is termed array tomography (Wacker and Schroeder, 2013). An automatic microtome was developed to facilitate serial section deposition on a special tape (Hayworth *et al.*, 2006). Gold fiducial markers are applied on the section surface as alignment markers for electron tomography.

Cryo-samples do not undergo contrasting. In this case, the native cellular environment provides all contrast, which is dramatically reduced compared to the plastic-embedded specimens. Gold fiducials are added directly to the sample on plunge-frozen grids before freezing. Deposition can be also performed at cryo-conditions, which is particularly important for tomography of vitreous sections (Gruska *et al.*, 2008; Harapin *et al.*, 2015).

Plastic embedded sample can be sectioned and imaged at the same time in the scanning electron microscope equipped with a microtome (serial blockface SEM, SBSEM) (Denk and Horstmann, 2004) or in the dual beam system with SEM column and focused ion beam column (Fig. 1.1) (Heymann *et al.*, 2006, 2009). In these setups the sample surface is imaged, the thin layer is removed from it by knife or ion beam milling and the new surface is imaged again. The sample is destroyed during acquisition. These methods allow reconstructing large cell or tissue volumes and FIB/SEM gives the highest resolution (5 nm isotropic voxel size) (Peddie and Collinson, 2014).

A special FIB/SEM instrument equipped with a cryo-stage and a sample transfer system can be used for thinning of vitreous samples which are too thick for direct EM imaging (Hayles *et al.*, 2010). FIB is used to remove unwanted material producing thin electron-transparent lamella suitable for electron tomography. The throughput of this method is reduced compared to vitreous sectioning but it leaves much fewer artifacts and the sample state is very close to native (Rigort *et al.*, 2012b; Harapin *et al.*, 2015; Mahamid *et al.*, 2015; Schaffer *et al.*, 2017).

1.2.4 Imaging

Ultrathin sections (50-100 nm) can be imaged in 2D or used to reconstruct the volume with serial sectioning approach. For this successive sections are collected and the same position is imaged on each section. The resulting images are stacked and aligned so that they make a volume (Cardona *et al.*, 2012). The z-resolution of this technique is limited by the ultrathin section thickness, although very large areas can be imaged. This allows a detailed description of tissue architecture and morphology of large cellular organelles. However many structures like small secretory vesicles and fine membrane shape smaller than 50 nm cannot be accurately visualized in 3D using this approach.

Electron tomography (ET) provides the highest possible isotropic 3D resolution (Lučić *et al.*, 2005; Gan and Jensen, 2012). Usually, slightly thicker sections (200-300 nm) are collected to acquire the data. The sample is rotated in the microscope column so that electron micrographs represent its projections at different angles. These images are computationally aligned and re-projected back into a 3D space to create a volume reconstruction. ET can reveal the finest details of membrane ultrastructure but this method has relatively low throughput. Collection of one tomogram could take 30-60 minutes. The reconstructed volume is also relatively small and is limited by the section thickness. Collection of serial tomograms is possible but even

more laborious. The larger volumes can be imaged with FIB/SEM or SBSEM at the expense of resolution (see above).

Tomographic reconstructions collected on frozen-hydrated specimens prepared by plunge-freezing, vitreous sectioning, or FIB-milling contain all the high-resolution structural information. However direct observation is not possible due to low signal-to-noise ratio. Structural information can be extracted from tomographic reconstructions by subtomogram averaging methods (Wan and Briggs, 2016). Small portions of the volume are extracted, averaged and iteratively aligned to this average to improve the resolution of the reconstruction (Nickell *et al.*, 2005). Subtomogram averaging can achieve atomic resolution and describe conformations and positions of macromolecular complexes within the cells (Asano *et al.*, 2015a, 2015b; Mahamid *et al.*, 2016; Schur *et al.*, 2016).

1.3 The diversity of correlative microscopy workflows

How to incorporate light microscopy into the EM workflow? Light Microscopy usually deals with entire living or fixed hydrated cells at ambient temperature. Such samples cannot be readily observed with EM. From the other side, samples prepared for EM do not usually retain fluorescence needed for light microscopy. This occurs because of the harsh chemical treatments applied on all steps of EM sample preparation, especially resin embedding. Still, LM can be incorporated into the EM workflow on almost any stage (Spiegelhalter *et al.*, 2014). For simplicity, we subdivide different CLEM methods into three main strategies for overcoming inherent LM-EM incompatibility: LM before embedding, LM after embedding and cryo-LM (LM without embedding). Additional steps are brought in by the CLEM workflow: *targeting* during sample preparation and image acquisition, and *registration* – a precise overlay of LM and EM data (Fig. 1.1).

LM before embedding is usually performed on living or pre-fixated cells and is not much different from conventional light microscopy protocols (Polishchuk *et al.*, 2012; Sjollema *et al.*, 2012). The imaged region position is marked in some way and the sample is processed for EM using conventional or slightly modified protocol. This method allows using almost unmodified LM and EM protocol, but the observed structures may change between LM and EM steps.

LM after embedding is usually performed on the ready sections either on EM grids or coverslips but the whole block can also be imaged using confocal microscopy. EM sample preparation is modified to preserve fluorescence in resin and obtaining high-quality LM data is more challenging than with conventional approach (Kukulski *et al.*, 2012b; Watanabe *et al.*, 2014). The advantage of this method is that exactly the same state of the specimen is imaged with both LM and EM.

Cryo-LM can be performed directly on the vitreous sample before imaging it in the EM. Fluorescence is perfectly preserved under cryo conditions because all molecules are immobilized in the native state (Briegel *et al.*, 2010). This

method requires special cryo-LM setups, which are more difficult to use and have lower resolution than room temperature microscopes.

All strategies better suit different biological questions and have some requirements and limitations. We discuss this below in more detail.

1.3.1 Pre-embedding LM

This method allows the most flexible combination of LM and EM because both protocols can stay almost unchanged. Light microscopy can be performed on living specimen as usual. Afterwards, cells are fixed for electron microscopy. Any type of fixation can be used. Some applications aim to decrease the time lapse between LM and fixation to ensure that observed structure or its position does not change much between two acquisitions. Fast addition of chemical fixation reagents right after the LM is finished does not present a difficulty, but it takes several minutes for the cellular components to stop moving. Freezing techniques fix the cells much faster, but some time is needed to transfer the sample from the microscope to the freezing device. One of the notable technical developments in this field is a microscope stage accommodating a holder for the Leica EMPACT2 high-pressure freezer rapid transfer system (Verkade, 2008; McDonald, 2009). This can shorten the time lapse to a couple of seconds, which is still not enough for some cellular processes.

Pre-fixation before LM step is another more often-used solution for minimizing the difference between the two imaging steps. Usually, the cells are pre-fixed with paraformaldehyde (PFA) (Braet *et al.*, 2014), which is a classic fixative for light microscopy, or with a mix of PFA and GA (Kobayashi *et al.*, 2012; Polishchuk *et al.*, 2012). After this, LM data is acquired and the cells are post-fixed for EM. PFA and GA do not act exactly in the same way, so the preservation quality may be worse with this approach, but one always should check if it suits the particular biological question.

After embedding is complete, the region of interest should be found back. This is the first step of targeting: including the imaged cell in the resin pyramid for sectioning and trimming away unwanted material. That's why pre-embedding LM protocols usually contain some type of coordinate system that survives the embedding procedure (Sjollema *et al.*, 2012). For example, glass around imaged cells is etched with a laser, or cells are just grown on a homemade or commercial etched coverslip or culture dish. The position of the imaged cell relative to these markers is recorded (Polishchuk *et al.*, 2012; Spiegelhalter *et al.*, 2014; Hellström *et al.*, 2015). After embedding the glass is removed leaving a negative imprint of the coordinate system on the block surface. Then the region is chosen to be included in the pyramid according to the known cell positions. After the sample is sectioned the marks can still be visible in TEM allowing more precise targeting for high-resolution data acquisition. In FIB/SEM the acquisition spot can be found using the marks directly visualized by SEM (Lucas *et al.*, 2014).

The strict requirement for such a coordinate system would limit the sample type to adherent cell culture only, but this is not the case. Any landmarks can be used for targeted microtomy and EM acquisition. The morphological features observed in the intact mouse ear and in the embedded sample are used for precise targeting of the microtomy and EM. The initial identification of the region can be facilitated by near-infrared laser branding of the tissue (Maco *et al.*, 2013; Karreman *et al.*, 2014).

The other reason that pre-embedding LM and EM data do not represent exactly the same structure is the deformation of the sample during dehydration and embedding. Shrinking is usually the most common artifact, which also can be not isotropic and different to correct for. This is especially crucial when a very small region should be found in a large and complex sample (like a piece of tissue or a small organism). That's why an additional LM imaging step can be introduced after embedding to calculate the sample deformation and the exact position of the region of interest (Kolotuev *et al.*, 2012; Karreman *et al.*, 2015).

To summarize, the pre-embedding LM approach is particularly suitable for "find a needle in a haystack" side of CLEM. Indeed it is very often used for localizing a transfected or infected fluorescent cell or an organelle that does not move too fast. Even relatively small region can be found back in a large 3D specimen. The other possibility presented by this approach is the combination with live imaging, which can be performed right before the fixation. This is the way to obtain some dynamic measurements of a process complemented by high-resolution characterization of the result (Stepanek and Pigino, 2016). However, displacements of the specimen components occurring between LM and EM steps do not allow precise localization of small and fast moving objects like virus particles or organelles. For this purposes, post-embedding LM protocols can be utilized.

1.3.2 Post-embedding LM

Retaining fluorescence in the embedded sample requires some compromises. Organic dyes can be preserved even in chemically fixed Epon-embedded cells (Rieder and Bowser, 1985), but fluorescent proteins require more subtle sample preparation protocol. One of the approaches relies on using cryo-fixation and freeze-substitution in hydrophilic resins. High-pressure freezing immobilizes all cellular components in the state close to native and freeze-substitution allows preserving it because chemical fixation is performed at low temperatures before resin infiltration. Methacrylate resins Lowicryl and LR white are most widely applied in post-embedding CLEM protocols (Nixon *et al.*, 2009; Kukulski *et al.*, 2011; Watanabe *et al.*, 2011; Peddie *et al.*, 2014). They are used to preserve protein epitopes to allow immunolabeling. During polymerization, these compounds do not crosslink with all macromolecules in the cell causing denaturation but rather with themselves. Hydrophilic nature of these resins allows keeping embedded proteins in a more hydrated state (Griffiths, 1993). An additional advantage of Lowicryl is that it can be polymerized at low temperatures, so the sample is not warmed up until the block is completely solid. Another important adjustment made in this

protocol is the reduction of fixatives amount. At least for Lowicryl resins, omitting GA and osmium tetroxide completely, and reducing the concentration of uranyl acetate does not significantly decrease the quality of ultrastructure preservation. Some protocols recommend adding up to 5% water to the freeze-substitution media to keep the sample partially hydrated claiming improved fluorescent protein preservation and better-contrasted membranes (Peddie *et al.*, 2014; Johnson *et al.*, 2015). After light microscopy sections can be contrasted with lead citrate or imaged without post-staining because the resin itself and uranyl acetate used for freeze substitution provide contrast. These adjustments allow preservation of fluorescent proteins but the sample still undergoes dehydration and interacts with anhydrous resin. This leads to variable preservation of different fluorescent proteins and even different fusion constructs with the same protein.

Careful selection and testing of fluorescent proteins are crucial for the successful imaging. The properly preserved fluorescent protein may allow very sensitive imaging of in-resin fluorescence. Diffraction-limited spots with the number of EGFP molecules as small as 25 can be observed.

In-resin CLEM aims to provide better molecular specificity assignment than traditional immunolabeling approaches. Constructing fluorescently labeled strain is easier than optimizing the immunolabeling protocol, and CLEM can be truly performed on 3D specimens while antibodies label only its surface. But still, immunolabeling provides more precise localizations. To compete with it, CLEM should allow specific localization of fluorescently labeled proteins with precision higher than the diffraction limit of the LM. Various super-resolution imaging techniques were developed during the last 10 years to break this barrier on regular samples. Some of them were applied for CLEM. The single molecule localization microscopy (SMLM) approach relies on the stochastic induction of fluorophore blinking (Betzig *et al.*, 2006; Sochacki *et al.*, 2014). Very few of them are active simultaneously during the long imaging period, which allows separation of their point spread functions and precise localization of single emitters. Right blinking periodicity and high

optical quality of the imaging setup is very important for precise localization. Both of these instances are altered in resin-embedded samples on EM grids.

Fluorophore blinking can be a result of the conformational change (mostly for photoswitchable or photoactivatable fluorescent proteins) or chemical reactions (mostly for organic dyes) (Fukaminato, 2011; Ha and Tinnefeld, 2012; Kozankiewicz and Orrit, 2014). Resin embedding crosslinks the molecules making the conformational change more difficult and alters the fluorophore environment and its chemical reactions. However recent works have shown that super-resolution microscopy is possible on resin-embedded samples both with standard and specially designed fluorescent proteins as well as with organic dyes (Watanabe *et al.*, 2011, 2014; Kopek *et al.*, 2012; Perkovic *et al.*, 2014; Johnson *et al.*, 2015; Paez-Segala *et al.*, 2015). Additional adjustments of sample preparation protocols are required to achieve good imaging quality. For example, the introduction of water and tannic acid in the freeze-substitution solution enhances blinking of standard fluorescent proteins in resin-embedded samples (Johnson *et al.*, 2015).

Localization precision in SMLM depends on the number of photons collected from each fluorophore. The use of high numerical aperture objectives is important for getting the highest numbers. Sections on EM grids are also imaged with the best available objectives but the conditions differ from conventionally fixed cells. Increased distance to the lens due to the EM grid curvature and additional refractive interface between water solution and the resin decreases the number of collected photons. To cope with this the TEM grid is sandwiched between the two coverslips to bring the section as close to the lens as possible. Another solution is to apply the sections directly on the coverslip. This enhances the quality of LM images but the resulting sample can be studied only with SEM. To obtain the TEM sample, the layer of support film (Pioloform) is deposited on the coverslip before applying the sections. After LM imaging the film with sections is floated away with hydrofluoric acid and mounted on the TEM grid (Watanabe *et al.*, 2014).

After imaging is completed, the LM and EM data can be overlaid. Since there is almost no distortion between the two datasets, very high registration precision is required. Usually, general morphological features are not enough to do this. For this purpose fiducial markers are introduced on the sample surface. These can be either plastic beads or gold particles which are both fluorescent and can be located in the electron micrograph. Relatively bright fluorescence allows subpixel localization of the bead center on the light micrograph. This, in turn, allows precisely mapping the centroids of spot-like signals of interest on the EM micrograph. For example, when using plastic beads 50 % of the signals were localized with the precision better than 50 nm (Kukulski *et al.*, 2011, 2012b).

To summarize, the post-embedding LM approach performs best for precise correlations and molecular characterization of fast events and relatively small structures. This is possible because almost no sample deformation occurs between LM and EM. This method also suits well for finding rare events, but the sample size is limited to the size of an EM grid (3 mm in diameter), which can be very small compared to large cell culture dishes that are observed by pre-embedding LM before choosing the region for sample preparation. However small sample on the same carrier makes it relatively easy to find back the region of interest in the post-embedding LM approach. No coordinate system needs to survive the sample preparation. The challenging side of this approach is to preserve the fluorescence in the resin-embedded sample. This may require testing few different labeling strategies and adjusting the EM sample preparation protocol. However, it was shown that even super-resolution imaging techniques can be implemented in the CLEM protocols. Further development of its application and especially wider implementation of isotropic 3D SMLM methods will make give CLEM additional advantages over the classic immunolabeling approaches in EM.

1.3.3 No-embedding LM (cryo-CLEM)

Cryo-CLEM allows observation of the specimen in the near native state with both LM and EM. Both fluorescence and ultrastructure are well preserved. The challenges here are in sample handling, the need for special cryo-light microscopy and cryo-EM setups, and in the low contrast of resulting EM images.

There are many technical solutions for cryo-LM imaging (Briegel *et al.*, 2010; Rigort *et al.*, 2012b; Kaufmann *et al.*, 2014). The typical cryo-LM setup is an inverted or upright microscope equipped with a stage cooled by liquid nitrogen or cold nitrogen gas. The stage is usually constructed to simplify transfer of the frozen EM grid. Long working distance objective is kept at the room temperature. The objective can be immersed in the cryo-stage cooled by nitrogen gas or placed behind the glass window; both solutions prevent the objective from cooling down. The need to keep the objective relatively far from the sample eliminates the possibility to use high NA and short working distance immersion objectives (Briegel *et al.*, 2010), so the resolution of the cryo-LM is usually lower than that of room temperature microscopes. A prototype cryo-immersion microscope was designed but there are no commercially available solutions (Le Gros *et al.*, 2009).

Although the resolution of cryo-LM is lower due to the lens restrictions, the fluorophore properties are enhanced (Moerner, 1999; Kozankiewicz and Orrit, 2014). Their fluorescence is preserved, and bleaching rates are dramatically reduced. This allows increasing exposure times and imaging sensitivity. The implementation of super-resolution techniques in cryo-LM does not only compensate the reduced resolution but comes close to the capabilities of the room temperature SMLM techniques. The major challenges for super-resolution imaging at cryogenic temperatures are the altered mechanisms of fluorophore blinking, cryo-stage instabilities, strong refraction of vitreous ice, and the sample sensitivity to high-intensity illumination (Kaufmann *et al.*, 2014). However the recent works show that all of these

difficulties could be overcome and methods development continues in this area (Chang *et al.*, 2014; Johnson *et al.*, 2015; Liu *et al.*, 2015).

Rapid progress in the cryo-EM field suggests that cryo-CLEM soon would be a good alternative to the room temperature methods.

Chapter 2. High-throughput correlative light and electron microscopy of budding yeast by fluorescent barcoding

2.1. Introduction

In light microscopy, functional studies can be extended from individual proteins to the whole-genomic level using genetic tools and automated workflows. Budding yeast (*Saccharomyces cerevisiae*) is a widely used model organism for high-throughput studies. Easy and scalable genetic manipulation allowed creating such tools as the systematic deletion library and the GFP collection (Giaever *et al.*, 2002; Ghaemmaghami *et al.*, 2003; Huh *et al.*, 2003; Ohya *et al.*, 2005; Giaever and Nislow, 2014). Combined with automatic microscopy these systematic libraries help to address a large variety of questions in cell biology (Cohen and Schuldiner, 2011; Breker *et al.*, 2014).

With the introduction of fully computer-controlled instruments, automated and large-scale data collection became available in electron microscopy as well. This particularly benefited the field of 3D electron microscopy which relies on the collection of a large number of projections (tomography) or serial sections (Mastronarde, 2005; Peddie and Collinson, 2014). However, in terms of the number of individual samples that can be analyzed, electron microscopy throughput remains relatively low because sample preparation procedures include manual steps. For example, to obtain the best preservation of both ultrastructure and fluorescence in yeast, the following workflow is used (Fig. 2.1). Yeast biomass is collected and manually inserted

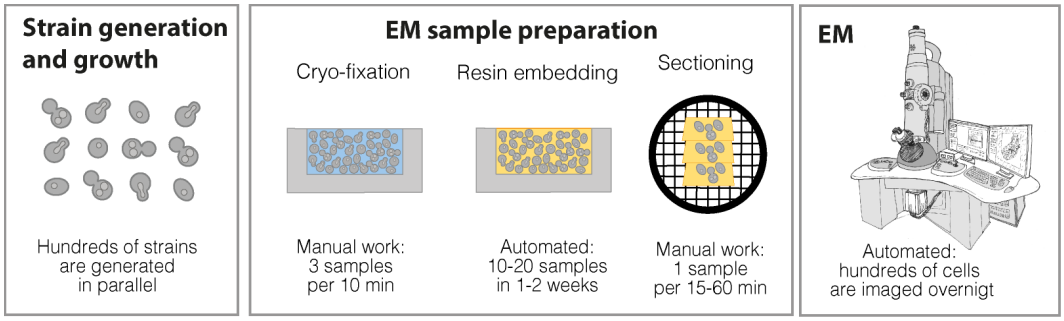

Fig. 2.1. Electron microscopy sample preparation workflow and its limitations. Compared to the process of strain generation, sample preparation is slow and manual. The limiting stage of the process is sectioning which requires a lot of manual operations per sample, while imaging of one sample in EM is well automated.

in a high-pressure freezing machine for cryo-fixation. Fixation of each sample can take 3-5 minutes and is entirely manual. After that, frozen samples are freeze-substituted. This process is automated; the freeze-substitution processor accepts 20 samples simultaneously. A typical freeze-substitution protocol can take up to a week. After that, each plastic block needs to be sectioned. For this, it is manually inserted in the microtome, trimmed, aligned with the knife, and sections are produced which need to be mounted on electron microscopy grids. This manual procedure can take from 15 minutes to 1 hour per block depending on sample quality. Such time limitations prevent applying light microscopy-style high-throughput screening paradigms to the ultrastructural features which can be observed only by EM.

Light and electron microscopy are more and more often applied to the same exact sample in a widening variety of correlative workflows to strengthen each other (see Chapter 1). For example, light microscopy can provide protein identity information from multicolor fluorescent labeling, or living cell dynamics data acquired right before the fixation (Kukulski *et al.*, 2012a; Stepanek and Pigino, 2016). We propose to use correlative microscopy to increase the throughput of electron microscopy experiments. To overcome the low throughput of the EM sample preparation workflow we aimed to develop a protocol for combining many independent experiments in one EM sample, so that fixation, resin embedding, and sectioning could be performed once for all experiments simultaneously. We decided to use fluorescent combinatorial labeling (barcoding) to encode cells' identity in the fluorescent

staining pattern, which can be deciphered using light microscopy prior to high-resolution EM imaging. The general workflow is illustrated in Fig. 2.2A. First, cells from different strains or under different experimental conditions are grown in parallel. Then, each of them is treated by a unique combination of fluorescent labels.

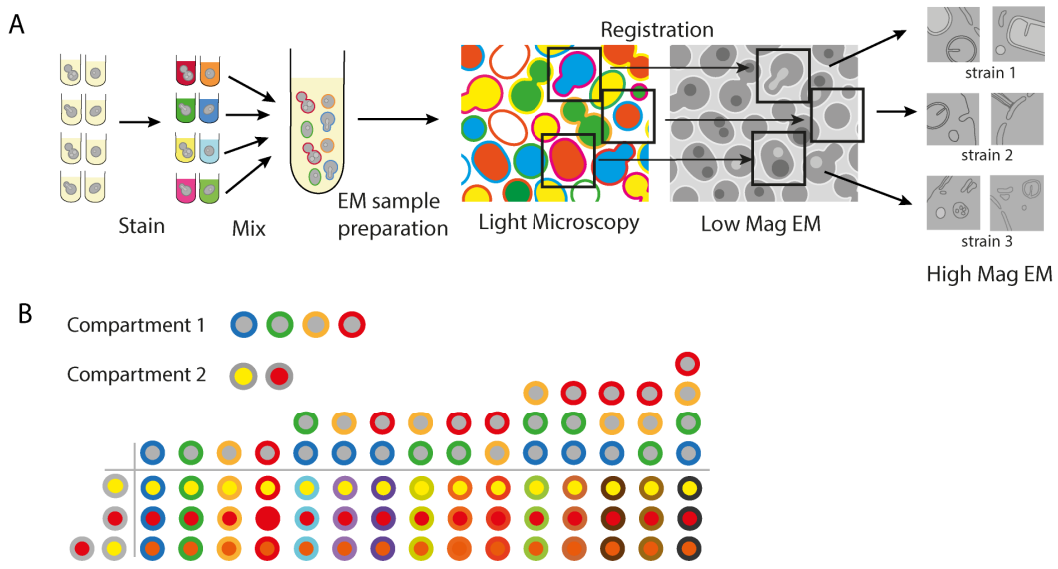

Fig. 2.2. Correlative light and electron microscopy with our fluorescent barcoding workflow. (A) Workflow schematic: strains or cells in different experimental conditions are grown in parallel and each is stained with unique combinations of labels; after that, strains are mixed together and processed for EM. The EM sample is imaged in the light microscope and EM at medium magnification, correlation is performed and cell identities determined, and the high-resolution information is collected if needed. (B) The number of barcodes assessment for two separate cell compartments. One compartment has four fluorophores giving 15 combinations (table columns), the other compartment has two fluorophores giving three combinations (rows), and their independent combination gives 45 barcodes.

After that, cells from parallel experiments can be mixed together and undergo EM sample preparation. Prior to EM, the sample is imaged under the light microscope to obtain staining patterns for each cell. Correlation is performed between fluorescent and EM images, and cell positions and identities determined.

2.2. General considerations

Sample barcoding is a common parallelization approach in biology. This idea was already applied in flow cytometry to develop the fluorescent cell barcoding technique (FCB) to parallelize experiments (Krutzik and Nolan, 2006). In microscopy, the Brainbow (Livet *et al.*, 2007; Weissman and Pan, 2015) and CLASI-FISH (Valm *et al.*, 2011, 2012) methods are used to discriminate individual cells and lineages in heterogeneous samples. These methods use different variations of combinatorial labeling to achieve the maximal number of reliably discriminated barcodes. We used similar reasoning to develop our protocol. The number of samples that can be combined together depends on the number of recognizable staining patterns that can be achieved. The staining pattern number is defined by the number of fluorescent reporters, the number of staining levels, and reporter localization within the cell. Staining levels are defined as different staining intensities that can be reliably recognized. The simplest case is two levels: stained or not. Three levels can be: not stained, stained with intensity *X*, and stained with intensity *2X*. The number of combinations for each cell compartment is therefore equal to L^N-1, where N is the number of fluorescent channels and L is the number of staining levels used for each reporter (the case without any staining at all is excluded by subtracting 1). In the case of two staining levels (stained/unstained), *L=2* and the maximal number of color combinations for one compartment is seven combinations for three fluorescent channels, 15 combinations for four channels, and 31 combinations for five channels. If staining of different compartments can be independently combined, the total number of combinations will be a multiple of those for all compartments. For example, 4 reporters in compartment I, and 2 reporters in compartment II, give in total 15×3=45 combinations (Fig. 2.2B).

What are the requirements for a model organism and fluorescent reporters used for barcoding? In principle, our proposed workflow can be applied to multiple different model systems experiencing throughput limitations at sample preparation but not at the imaging stage. Reporters can be chemical

dyes or genetically encoded intrinsically fluorescent proteins. The main requirements for the reporters used in our proposed post-embedding CLEM protocol are: they are bright, they survive resin embedding, they stain the same compartment exactly the same way in different fluorescent channels, and they can be easily delivered to the stained compartments in a combinatorial way. Partial labeling of a subset of cells in one channel but full labeling in another will create a large number of false or ambiguous patterns. Compartments used for staining should be abundant (large) enough to appear in most cross-sections through the cells. Otherwise, the exact staining patterns of a large number of cells will remain undefined. The total number of combinations and therefore the throughput increase will depend on the number of reporters and compartments satisfying these requirements.

2.3 Staining protocol development

We tested a number of chemical dyes for barcoding of budding yeast. None of the dyes for any intracellular compartments we tested satisfied the conditions discussed above (Table 2.1). However, fluorescent conjugates of concanavalin a (con a) proved to be very convenient cell wall reporters suitable for barcoding. Many conjugates are commercially available already, and other dyes can be easily attached to con a using a simple protocol. We selected five con a conjugates that can be resolved on many conventional wide-field microscopes: Alexa 350, Alexa 488, tetramethylrhodamine (TRITC), Alexa 647, and Cy7. We applied a binary approach with two levels of labeling for each dye (YES or NO) and allowing all possible combinations. This gives 7,15, and 31 staining patterns for three, four, and five dyes respectively.

Table 2.1. List of fluorescent dyes tested for labeling of yeast organelles. Color is given according to filter set used for imaging, see Table 2.7.

Dye	**Compartment**	**Color**	**Solvent**	**Problem**
Calcein Blue AM	Cytoplasm, Vacuole	Blue	PBS	Very dim cytoplasm, few vacuoles labeled
CellTracker Green CMFDA	Cytoplasm	Green	PBS	Weak, uneven staining
CellTracker Red CMTPX	Cytoplasm	Red	PBS, Diluent C, Sucrose solution	In PBS does not go in cells, in Diluent C and sucrose stains only subpopulation of cells; Impossible to use with other dyes
DiOC16	Membranes	Green	Diluent C	Does not go in cells
DiIC12	Membranes	Orange	Diluent C, sucrose solution	Stains all membranes, but cells display highly various overall fluorescence intensity
LysoTracker Red	Lysosomes (Vacuole?)	Red	PBS	Stains a very small subset of cells
MitoTracker Green	Mitochondria	Green	Diluent C, PBS, sucrose solution	Variable staining, including unspecific, not well-preserved in resin
MitoTracker Orange CMTRos	Mitochondria	Orange	PBS	No problems, stains all mitochondria very well, preserved in resin
MitoTracker Deep Red	Mitochondria	Red	Diluent C, sucrose solution	Bad cell penetration, dim staining, not well-preserved in resin
FM 6-64	Endosomes/Vacuoles	Blue ex./Red em.	Media	Spectrum is not well suited for regular wide-field microscope; not observed after embedding
FM 1-43FX	Endosomes/Vacuoles	Green	Media	Preserved in resin, but not observed in many enough sections
CellTracker Blue CMAC	Vacuole	Blue	HEPES, according to manual	Bright fluorescence in almost all vacuoles in living cells, not well enough preserved in resin
Carboxy-DCFDA	Vacuole	Green	HEPES	Stains ~80% of vacuoles
CMAC-Arg	Vacuole	Blue	HEPES	Too dim
CMAC-Ala-Pro	Vacuole	Blue	HEPES	Too dim
MDY-64	Vacuolar membrane	Green	Media	Bright staining, not tested in resin
Hoechst	Nucleus	Blue	PBS	Very dim staining even at high concentrations
DRAQ5	Nucleus	Red	PBS	Internalized, but not fluorescent. Fluorescence activates after ~1 minute of excitation and is relatively dim. The dye is expensive.

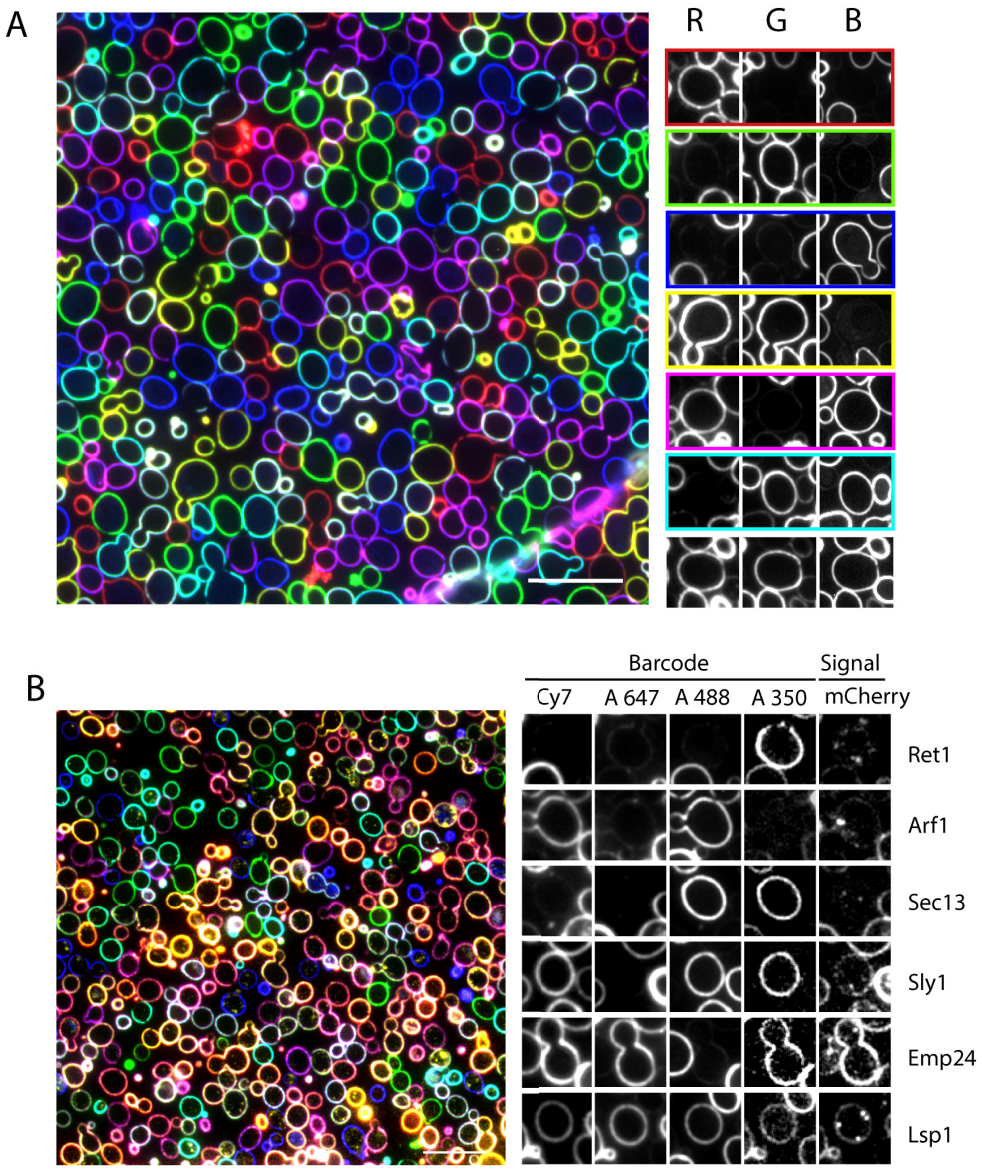

Fig. 2.3. Barcodes imaged by light microscopy. (A) Three-fluorophore example of seven well-discriminated combinations. On the right: pseudocolor composite image of a 100 nm thick Lowicryl section of embedded cells labeled with con a conjugated to Alexa Fluor 350, Alexa Fluor 488, and TRITC. On the left: examples of individual cells with all possible barcodes, each column corresponds to one fluorescent channel. (B) Using four fluorophores for barcoding strains with mCherry fused to secretory pathway proteins. On the left: pseudocolor composite image of a 150 nm thick Lowicryl section of yeast labeled with different combinations of con a conjugated to Alexa Fluor 350 (blue), Alexa Fluor 488 (green), Alexa Fluor 647 (red), and Cy7 (magenta). On the right: examples of individual strains with different barcodes and mCherry fusions. Each column represents one fluorescent channel, and each row is a different ORF fused to mCherry, labeled on the right. Scale bars 10 μm.

We optimized dye mix preparation and staining conditions to achieve the bright and uniform cell wall staining necessary for automated image processing (see section 2.6). As a result, we developed an easy-to-use barcoding protocol (listed in section 2.4). The best results are achieved when concanavalin is diluted in phosphate buffered saline (PBS) and not subjected to alterations of pH and temperature. To reduce its aggregation and make combining dyes easier, we prepare intermediate stock solutions of each dye from the frozen con a stocks and ultracentrifuge to remove aggregates. Intermediate stock solutions are used to produce working staining solutions with all dye combinations. Sample fixation, resin embedding, and light microscopy imaging did not need modification and were performed as described before (Kukulski *et al.*, 2012b).

To demonstrate the barcoding principle we prepared a sample with three fluorescent dyes and seven color combinations (Fig. 2.3A). When all channels are displayed on pseudocolor overlay of red, green, and blue it is easy for the human eye to recognize all seven possible combinations of three primary colors (red, green, blue, cyan, magenta, yellow, white). The cell walls demonstrate bright homogeneous staining.

Our staining protocol achieves a relatively modest number of staining patterns (maximum – 31), which can be increased using previously developed barcoding methods. For example, FCB and Brainbow make use of different staining levels for each fluorophore. This allows Brainbow to achieve at least 100 unique staining patterns (Weissman and Pan, 2015). CLASI-FISH uses only binary combinations of fluorophores to increase the method reliability which reduces the number of combinations, but at least six fluorophores with overlapping spectra are used together and discriminated with the help of linear unmixing (Valm *et al.*, 2012). Applying more staining levels or fluorophores is possible but would require staining protocol modification to achieve brighter and more even staining. Image processing workflow would need to be modified to allow more sensitive and reliable staining pattern discrimination.

2.4 The staining protocol

2.4.1 Materials and equipment

- Tubes or plates (with gas-permeable membrane)
- Yeast media
- Spectrophotometer
- Spectrophotometric cuvettes (plastic)
- Yeast incubator
- Centrifuge for plates
- Phosphate buffered saline (PBS)
- Con a stock solutions, 2.5 mg/ml in PBS
- Ultrasonic bath
- Centrifuge for 1.5 ml tubes
- (Optional) Ultracentrifuge and rotor,1.5 ml tubes
- 0.3 mm and 0.1/0.2 mm aluminum membrane carriers for HPM010
- HPM010 high-pressure freezing machine
- Fresh YPAD agar plate
- Small flat metal spatula
- Razor blade
- Pipet (under 10 µl)
- MILLIPORE filtering setup with 0.45 um filter
- Tweezers and forceps

2.4.2 Yeast cultures

For one freezing the total amount of cells should be 15-20 ml of OD_{600}=0.6. This means that for a 15-fold multiplexed experiment each strain should be grown in 1 ml to OD_{600}=0.6. This can be done in separate tubes or in a 24-well plate. Separate tubes are more difficult to handle but easier to grow (in a normal incubator). 24-well (or 96-well) plates require smaller amplitude and higher speed orbital shaker (they cannot be properly mixed with a normal incubator for flasks). One can do it by using a plate shaker, or by sticking a plate to the top of the Eppendorf Thermomixer which is in turn placed inside of a regular incubator to get to 30°C. The cultures can be prepared the day before to reach the OD_{600}=0.6 in the morning, so staining can be started

immediately, or grown from diluted overnight cultures during the day. We use the following growth protocol to achieve desired cell density before freezing in the afternoon:

1. Dilute the overnight cultures in tubes or in a plate. To get OD_{600}=0.6 at 14:00 one would need 0.15 at 9:30 for relatively fast growing strains.
2. If using a plate, seal it with a gas-permeable membrane, and install on the thermomixer or plate shaker inside the incubator at 30°C. The shaking speed should be 500-600 rpm.

2.4.3 Staining solution preparation

1. Thaw concanavalin a stock solutions (2.5 mg/ml in PBS) and sonicate for 5 minutes in an ultrasonic bath to dissolve the aggregates.
2. Spin down the remaining large aggregates on a tabletop centrifuge, max rpm (16000 rcf), 4°C. The amount of pellet indicates the aggregation propensity of the particular stock.
3. Prepare 5× stock solutions for fast mixing. These solutions are afterwards mixed in the same amounts. To compensate for different conjugate brightness the concentrations can be adjusted at this stage (Table 2.2).
4. Optional: ultracentrifuge 5× stocks 30 min at 200000 g (45000 rpm) on TLA55 rotor of Beckmann tabletop centrifuge to remove more aggregates.
5. Mix the 5× stocks with PBS to get final staining solutions (Table 2.3). They are numbered and arranged as the first two columns of a 96-well plate. The scheme can easily be extended to 5 colors with the same total volume of one solution – 600 µl – by adding extra 120 µl of the fifth stock solution.

Table 2.2. An example of intermediate 5× con a stocks composition. The total volume of each stock is ~ 1 ml for convenient ultracentrifugation, the amount of each con a storage stock can be adjusted depending on the conjugate quality and brightness (in this example Alexa 488 conjugate was the brightest and required 40 µl of the storage stock, while the Cy7 conjugate was very dim and required a larger amount).

Stock	**Con a, µl**	**PBS, µl**	**Total, µl**
B: Con a Alexa 350	120	930	1050
G: Con a Alexa 488	40	1010	1050
O: Con a TMR 555	50	1000	1050
R: Con a Alexa 647	100	950	1050
IR: Con a Cy7 (home made)	250	800	1050

Table 2.3. Combinatorial mixing of the working staining solutions. Solutions are numbered like the first two columns of the 96-well plate. B, G, O, and R are the names of 5× stock solutions from Table 2.2. All amounts are given in µl.

Solution	**B**	**G**	**O**	**R**	**PBS**	**Solution**	**B**	**G**	**O**	**R**	**PBS**
1A	120	0	0	0	480	**2A**	0	120	0	120	360
1B	0	120	0	0	480	**2B**	0	0	120	120	360
1C	0	0	120	0	480	**2C**	120	120	120	0	240
1D	0	0	0	120	480	**2D**	120	120	0	120	240
1E	120	120	0	0	360	**2E**	120	0	120	120	240
1F	120	0	120	0	360	**2F**	0	120	120	120	240
1G	120	0	0	120	360	**2G**	120	120	120	120	120
1H	0	120	120	0	360	**2H**	0	0	0	0	600

Table 2.4. A scheme of staining of a 24-well plate with the working solutions of combinatorial labels. Rows and columns of the table correspond to rows and columns of a 24-well plate, in each cell name of the applied solution (as assigned in Table 2.3) is given.

	1	**2**	**3**	**4**	**5**	**6**
A	1A	1E	2A	2E	-	-
B	1B	1F	2B	2F	-	-
C	1C	1G	2C	2G	-	-
D	1D	1H	2D	-	-	-

2.4.4 Staining and freezing

1. Check the OD_{600} of all or a selection of strains. It should be 0.5-0.6. When the right OD is achieved, start filling HPM010 with nitrogen before doing the next steps. Filling takes 15-20 minutes.
2. Spin down the cells at 1500 rcf for 5 min.
3. Carefully remove the plate from the centrifuge and discard the supernatants without disturbing the pellets. The pellets are very loose at this stage! Immediately after removing the supernatant fill the well with the staining solution and mix well. The scheme of solution application to the 24-well plate is shown in Table 2.4.
4. Make sure the pellets are resuspended well and put the plate on the mixer in the incubator for 5-10 minutes. Avoid exposing to bright light.
5. Remove the plate from the incubator and spin it down at 1500 rcf for 5 min. Discard the supernatants and resuspend pelleted cells in medium. The pellets with con a cover the whole well bottom and are stronger. Better mixing is required in order to collect all of the cells.
6. During the resuspension or afterwards pool everything in one 50 ml falcon tube. Vortex it well.
7. Proceed with freezing immediately. Collect the yeast on the filter using the MILLIPORE filtering device, and immediately put the filter on a fresh YPAD plate. Make sure it is wetted by plate and there are no bubbles in-between the filter and the agar surface.
8. Scrape the cells from the filter into a denser clump with a spatula. To make them more dilute, press with a spatula to squeeze water from the plate. To concentrate the cells lift the filter for a short time.
9. Cut off the end of the pipet tip to make the hole wider, and suck 1.5-1.75 µl of suspension with this tip, holding the clump with a spatula. Do not press too much for not to dilute the suspension.
10. Apply the suspension to the 0.1 mm cavity of a membrane carrier, cover with a flat side of a 0.3 mm cavity carrier, and freeze immediately.

2.5. Combining barcoding with a conventional CLEM experiment

To demonstrate an application of our parallelization protocol for conventional in-resin CLEM, we designed an experiment to visualize different proteins functioning in the early secretory pathway. We selected a set of 14 proteins that had punctuate cellular localization and bright signal on the images from the yeastgfp and LoQate databases (Ghaemmaghami *et al.*, 2003; Breker *et al.*, 2014). We obtained strains with mCherry fused to these ORFs and barcoded them using four fluorescent con a conjugates (Alexa 350, Alexa 488, Alexa 647, and Cy7). We selected mCherry because of its lower pH-sensitivity which results in better preservation after resin embedding compared to GFP fusions (Chudakov *et al.*, 2010; Xiong *et al.*, 2014). Despite crosstalk between mCherry and Alexa 647 fluorescent channels, spot-like signals can be discriminated from the background and the strain identity can be successfully determined (Fig. 2.3B). This result demonstrates that the proposed method can be used to increase the throughput of conventional in-resin CLEM experiments and analyze many cell strains at once. However, a significant proportion of strains used in this study did not show good preservation of mCherry signal after embedding. This could be the result of insufficient protein copy numbers or mCherry destabilization by the protein to which it is fused. Uncovering this variability using a single-sample approach would take a long time, while multiplexing allowed us to identify five proteins listed in Fig. 2.3B (in addition to Lsp1, which was the positive control for preservation) as good targets for subsequent in-depth CLEM analysis. Multiplexing also allowed direct comparison of sample fluorescence with a positive control within one micrograph.

2.6. Image processing pipeline development

Our approach can be used to analyze large sets of cells at high resolution using electron microscopy. We developed a workflow for automation of analysis, correlation, and targeting of high-resolution acquisition. The workflow makes use of SerialEM software (Mastronarde, 2005) for EM imaging, ilastik software (Sommer *et al.*, 2011) for EM image processing, and Matlab for correlation and all other processing (Fig. 2.4).

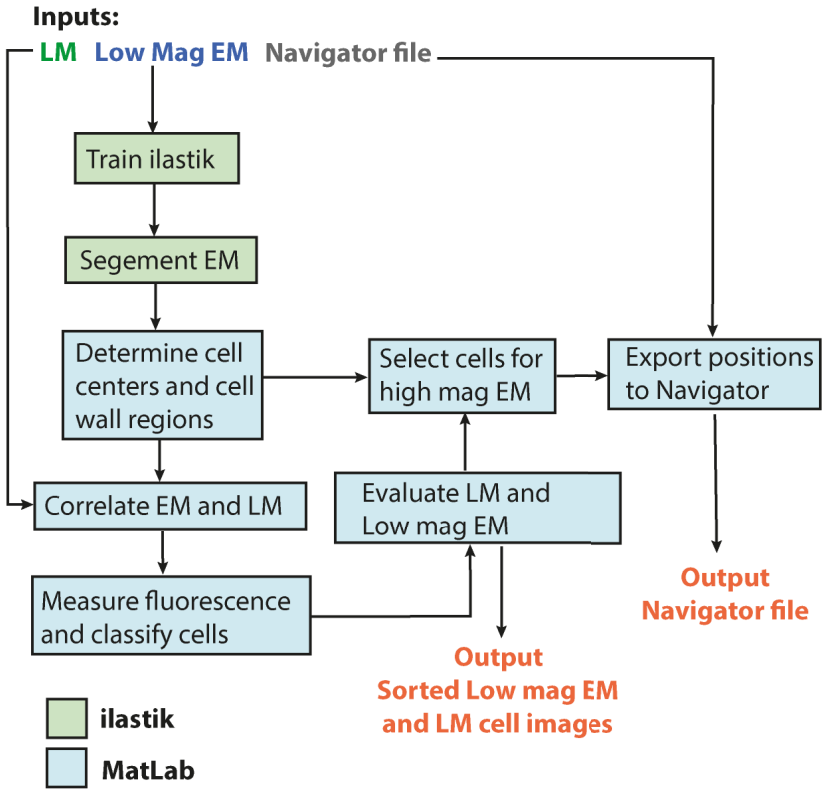

Fig. 2.4. Image processing and correlation workflow. Steps performed using different software packages are denoted by color. Further explanation is available in the text.

After light microscopy, medium magnification EM montages are acquired at the same sample regions using SerialEM software and saved as Navigator maps (Fig. 2.5A,B). This feature allows the microscope to reliably return to these positions later. Light and electron microscopy images are correlated using Matlab to generate an overlay of LM and EM data (Fig. 2.5C,D). The standard point selection tool and 7-10 registration points are sufficient to

generate an overlay of enough precision. The EM image is segmented in ilastik and further processed in Matlab to identify centers and outlines of individual well-preserved cells. Center coordinates are used to import them back to the EM maps as points for high-resolution acquisition. Outlines are used to generate masks for the measurement of fluorescent signal intensity for each cell. The algorithm accounts for intersections of mask regions of neighboring cells to avoid bias (Fig. 2.5F).

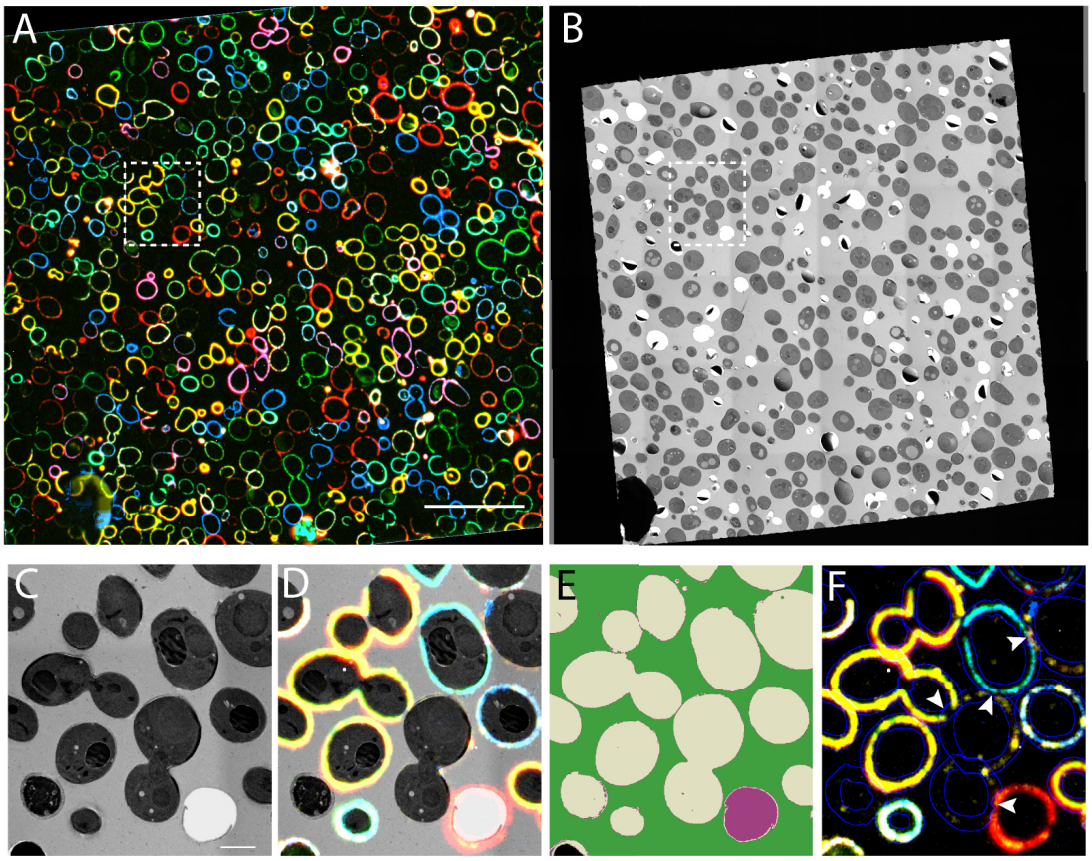

Fig. 2.5. Image processing for cell and barcode identification. (A) Transformed light microscopy pseudocolor image of a 100 nm thick Lowicryl section of the sample with yeast labeled with con a conjugated to Alexa Fluor 350 (blue), Alexa Fluor 488 (green), TRITC (yellow), and Alexa 647 (red) matching the same region as depicted in panel B. (B) Medium magnification montage of the same sample region as depicted on panel A. (C) Close up EM view of the sample region marked by dashed rectangle in panels A and B. (D) Overlay of EM and fluorescent data shown in panels A and B by dashed rectangles. (E) Ilastik segmentation of the EM image. Cells good for imaging are shown in gray, resin in green, holes in the resin are in purple, electron-dense regions are in black. (F) Cell wall outlines determined from EM image segmentation and used to measure fluorescent intensities are shown in blue and overlaid with the composite fluorescent image, white arrow heads show regions excluded from masks due to intersections with neighboring cell walls. Scale bars are 20 μm in A and 2 μm in C.

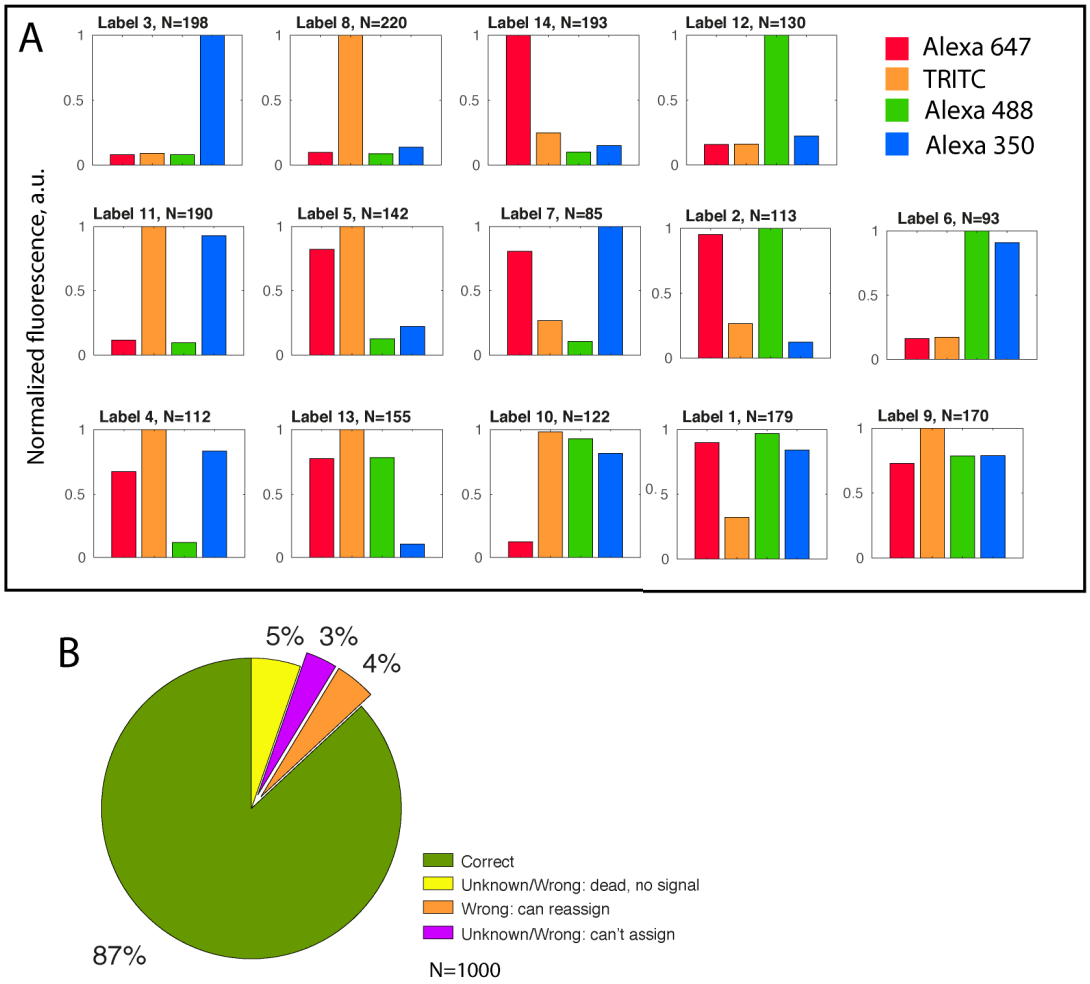

Fig. 2.6. Barcode determination and verification. (A) Normalized intensity plots are shown for each cluster of intensity combinations determined by k-means clustering. Label number is the arbitrary number assigned by k-means to a cluster; correspondence with strains is given in Fig. 2.7. (B) The result of manual barcode verification. Details are available in the text.

Measured fluorescent intensities are normalized and used to perform k-means clustering to separate staining patterns from each other (Fig. 2.6A). To assess the precision of this approach, we visually determined barcodes for 1000 cells and compared them to automated prediction (Fig. 2.6B). Almost 90 % of cells showed agreement, 5 % of the cells had abnormal morphology and no cell wall signal detectable by eye, 4 % of cells were classified incorrectly and image quality allowed correct assignment by eye, and the remaining 3 % could not be identified by eye due to the poor quality of the fluorescence data. Since the 5 % of cells with aberrant morphology are excluded from further analysis, the barcode determination accuracy is >90%. We find this suitable

for an initial screening experiment. The precision can be further improved by the introduction of additional quality control steps. We propose removing cells with overall low fluorescent intensity, and developing a pipeline to identify bright con a aggregates that obscure the barcode signal.

2.7. Proof of principle experiment

2.7.1 Experiment design

To show the utility of the method for parallelizing both different strains and experiments we explored how different yeast strains and deletion mutants vary in ultrastructural morphology and respond to mild hyperosmotic shock with subsequent restoration of osmolarity. We selected 7 yeast strains (reference lab strain, two wild type wine yeast isolates PRICVV50 and SFB2, and four deletion mutants with defects in stress response and endomembrane system organization *Δhog1*, *Δtcb1*, *Δvps35*, *Δlpl1*), grew them in parallel and then subjected them to hyperosmotic shock (1 M sorbitol) for 45 minutes. The same control set of strains without shock and strains under shock were barcoded, combined together and high-pressure frozen. In addition to a 14-fold increase in throughput, simultaneous fixation and processing within one sample helped us to avoid any variation arising between different samples during fixation and embedding.

2.7.2. Overall ultrastructure comparison

We acquired a gallery of high-resolution micrographs for each cell strain and experimental condition (Fig. 2.7). The ultrastructure was well preserved and was comparable to the literature examples of high-pressure frozen yeast embedded in Lowicryl (McDonald, 2007; McDonald *et al.*, 2010). In total for this experiment, we acquired images of 1748 cell sections (around 100 sections per experimental condition). By visual inspection, all cells had a similar ultrastructural phenotype to the reference strain S90, with slight

variation. However striking differences were observed for mitochondria and multivesicular bodies (MVBs).

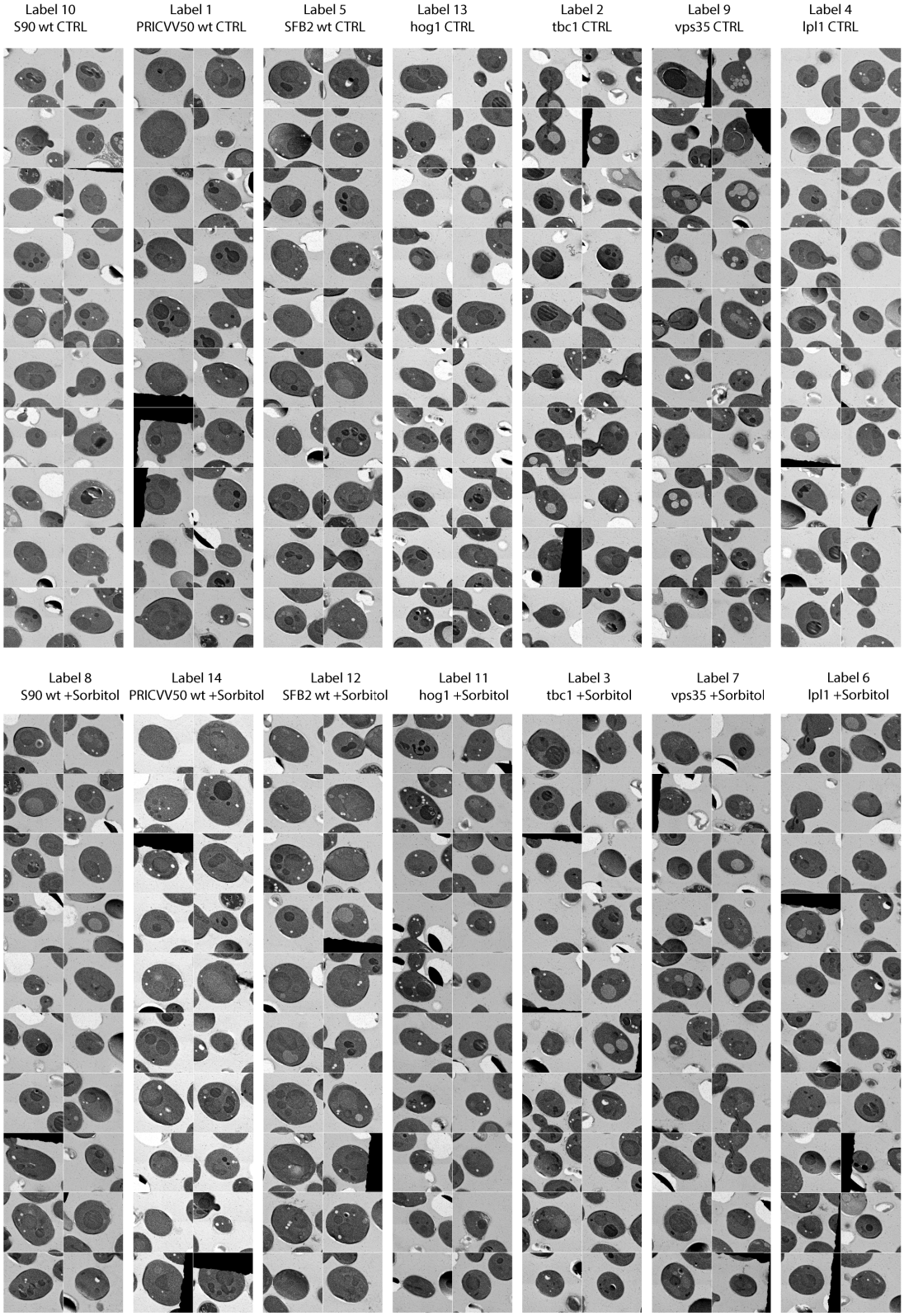

Fig. 2.7. A gallery of yeast cell sections from different strains and experimental conditions. For each group 20 random examples of images from the final high-resolution dataset are given. All cells display good preservation, and larger maximal cross-section diameter is apparent for the wine yeast.

One of the wine yeast strains (SFB2) showed a remarkable alteration of mitochondria ultrastructure compared to S90 strain in both control and osmotic stress conditions (Fig. 2.8). Mitochondria in this strain appear swollen and lack electron density in the matrix. It is not clear how such dramatic morphological alteration might be linked to mitochondria function.

MVBs in different strains demonstrated different shapes and abundance (Fig. 2.9). We chose to study these differences in more detail.

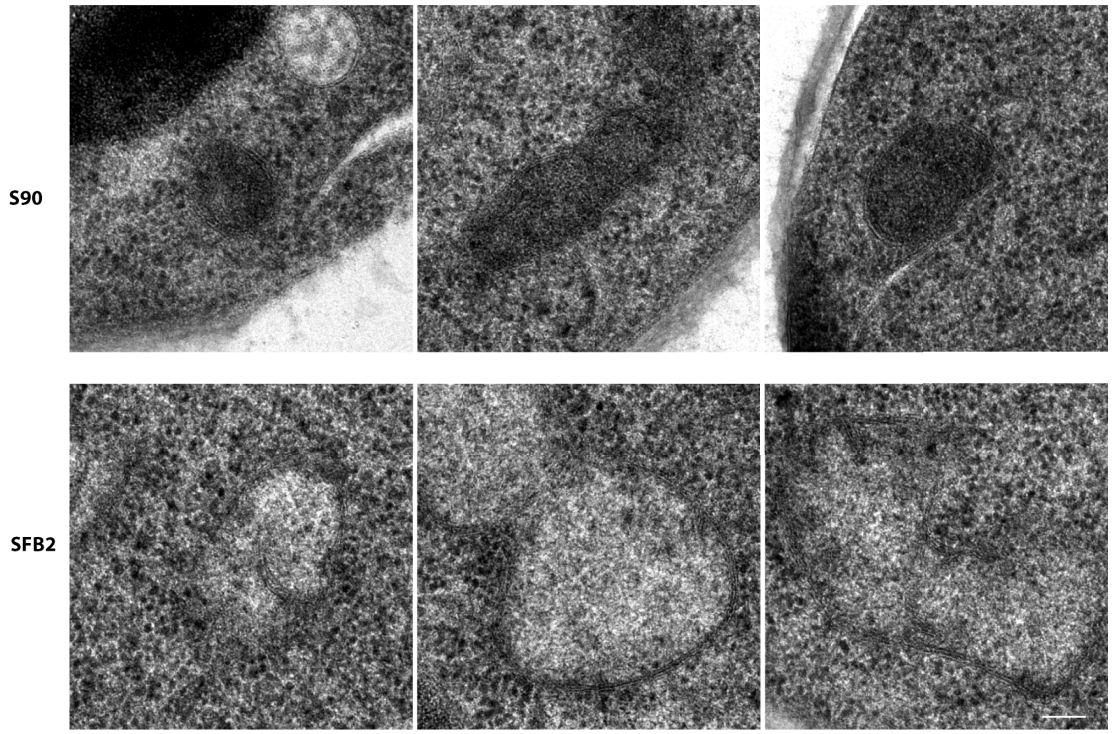

Fig. 2.8. Abnormal mitochondria phenotype in the SFB2 strain. Examples of mitochondria ultrastructure in S90 reference strain (top) and SFB2 wine yeast isolate under normal osmotic conditions. Scale bar is 100 nm.

S90

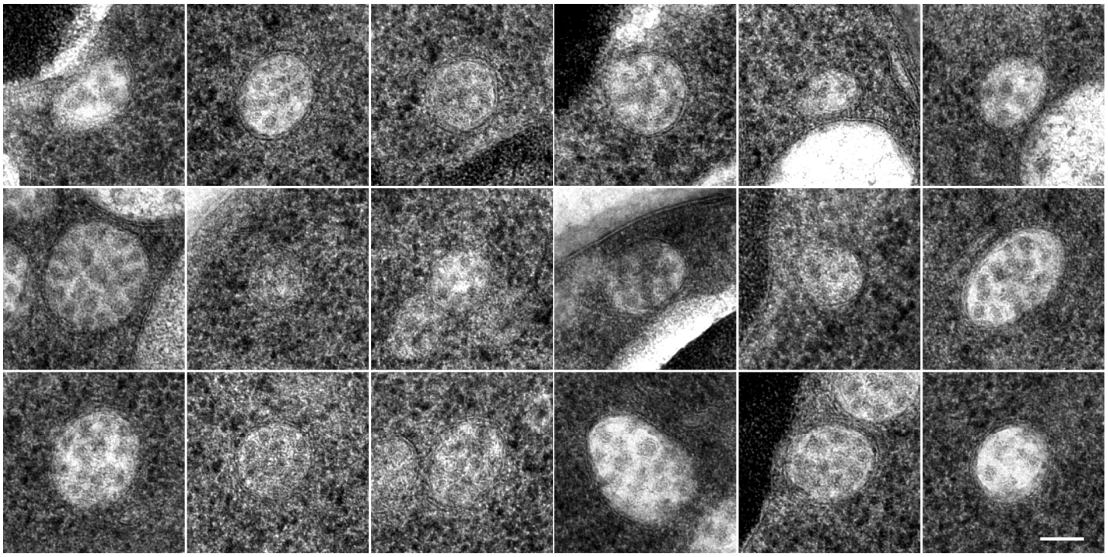

PRICVV50

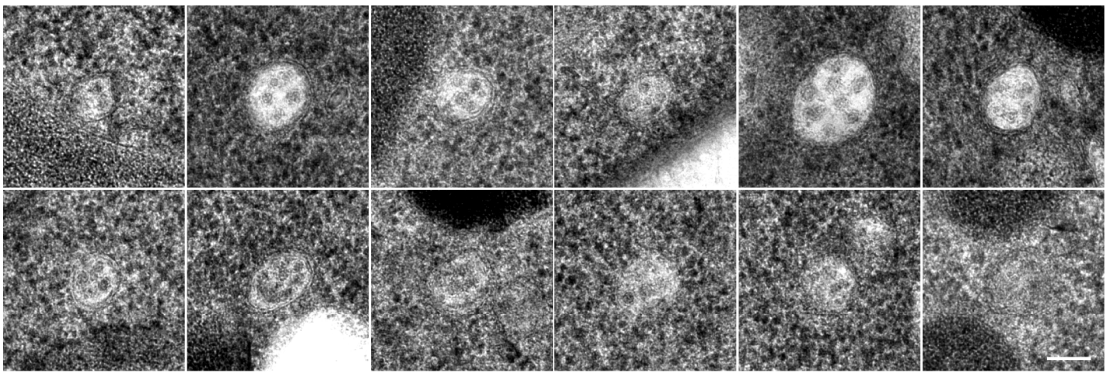

Δhog1

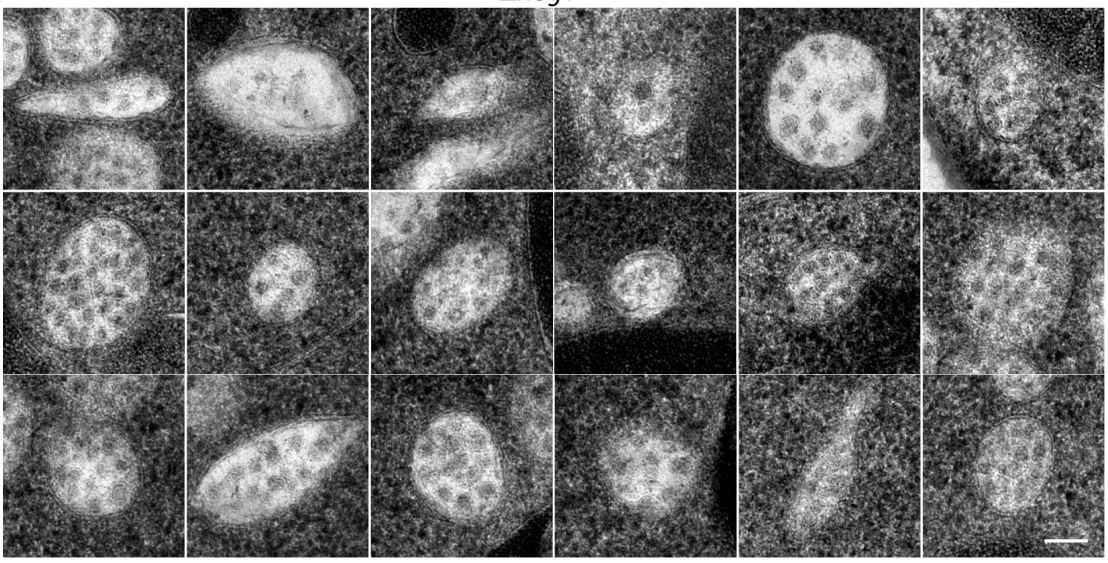

Fig. 2.9. Multivesicular body ultrastructure variation. Examples of 18 MVB cross-sections from the reference S90 strain (top), 12 cross-sections from the PRICVV50 strain, and 18 cross-sections from the hog1 deletion mutant under normal osmotic conditions. The 12 examples from PRICVV50 are all MVBs found in the dataset of 179 micrographs obtained for this strain under normal osmotic conditions. Scale bar is 100 nm.

2.7.3 MVB morphology quantification: Results

Using single 2D sections taken at random orientation through the cells it is possible to estimate such quantities as organelle volume fraction in the total cell volume and their surface to volume ratio using a stereology-like approach (Howard and Reed, 2005). We performed these measurements for MVBs observed in our dataset.

First, we measured areas of cell cross-sections for each strain and condition (Fig. 2.10A). It is not possible to estimate mean cell volume from these data, but distributions can be compared with each other. PRICVV50 and SFB2 strains were characterized by increased cross-section areas, which signifies larger cells. PRICVV50 is reported as diploid (Novo *et al.*, 2009), which explains their larger cell size. The similar size distribution for the SFB2 strain shows it might be diploid as well. The sum of all cell cross-section areas for each strain was used to calculate MVB volume fraction.

In each MVB image, we measured the length of the organelle's longest axis and the maximal length of the perpendicular axis. MVB cross-section areas and circumference were calculated by approximating each outline as an ellipse (Fig. 2.10B). Total areas of MVB and cell cross-sections were used to calculate MVB volume ratios in total cell volume (Fig. 2.10C) and the ratio between MVB area and the circumference was used to estimate the average MVB surface to volume ratio (Fig. 2.10D). Investigated strains showed dramatic variation in MVB volume fraction. Wine yeast strains were characterized by very low fractions, less than 1%, while the hog1 deletion strain has the highest fraction of about 6%. Other strains had similar MVB volume fractions – about 4%. Sorbitol treatment did not influence MVB volume fraction in most strains, with an apparent difference noticeable only in the lpl1 deletion mutant. The MVB surface to volume ratio was similar in all

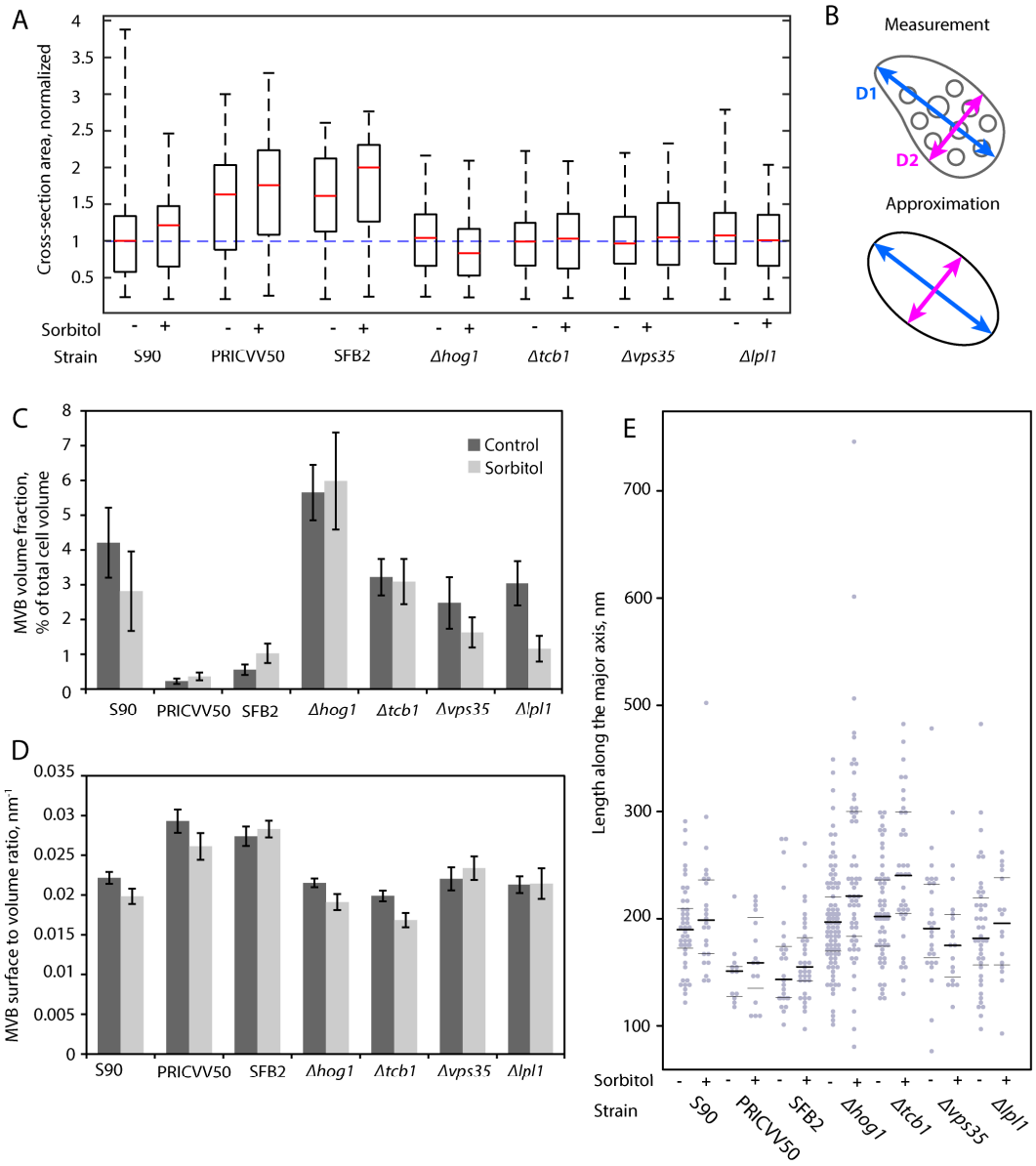

Fig. 2.10. Quantitative analysis of MVB morphology. (A) Distributions of total cell cross-section areas for different strains and conditions, normalized to the S90 control (blue dashed line); boxes show the 25th, 50th, and 75th percentiles, whiskers show the range. (B) MVB major and minor axis measurement example and approximation of its shape as an ellipse with the same major and minor axes. (C) MVB volume fractions in total cell volume in different strains and conditions, error bars show standard error of mean calculated as described in Materials and Methods. (D) MVB outer surface to volume ratio in different strains and conditions, error bars show standard error of the mean. (E) Major axis length variation in individual MVB cross-sections measured in different strains and conditions. Lines indicate the 25th, 50th, and 75th percentiles.

strains and was slightly higher (~20%) in wine yeast. We analyzed the variability of individual cross-sections by plotting distributions of major axis length (assuming MVBs are spherical or ellipsoid) (Fig. 2.10E). Deletion mutants tend to have larger and more variable MVBs.

2.7.4 MVB morphology quantification: Discussion

MVBs are important intermediates of the endosomal-lysosomal pathway. Membrane proteins delivered from endosomes and the trans Golgi network (TGN) are sorted in MVBs. They are either recycled back to the plasma membrane and TGN or are included in intraluminal vesicles (ILVs) for degradation in the lysosome (in mammals) or vacuole (in yeast and plants) (Huotari and Helenius, 2011; Hanson and Cashikar, 2012). MVB biogenesis and morphology are reviewed in more detail in Chapter 3.

These processes occur on a very small size scale, making electron microscopy an important technique for characterizing MVB morphology and biogenesis (Nickerson *et al.*, 2010). Yeast genetics, light and electron microscopy played important roles in elucidating the whole endosomal sorting and recycling pathway and its mechanistic details. However, some aspects of its regulation remain unknown. Among those are the mechanisms that determine the number and size of these organelles. Endosome size and number are important factors in receptor tyrosine kinase signaling pathways (Collinet *et al.*, 2010; Villaseñor *et al.*, 2015). In mammalian cells EGF signaling was shown to increase MVB biogenesis and ILV budding (White *et al.*, 2006), however little is known about MVB size and number regulation in yeast. In this work, we show that the relative volume fraction occupied by MVBs in yeast cells can vary considerably between strains. The most proliferated and heterogeneous MVBs were found in the *hog1* deletion mutant. Hog1 protein is a MAP kinase responsible for osmotic shock response, and also it is involved in responses to starvation and oxidative stress (Hohmann *et al.*, 2007; Piao *et al.*, 2012; Lee *et al.*, 2017). The MVB expansion could be an unspecific reaction and a consequence of cell morphogenesis dysregulation occurring after the loss of such important regulator, even without osmotic stress conditions. The other three deletion mutants showed similar MVB volume ratios under control conditions, probably reflecting the value characteristic of the background strain (which was not included in the experiment). In this respect, dramatically reduced MVB volume ratios in wine yeast can be considered a manifestation of the lower stress level experienced by these

cells. Indeed, a large scale genotypic and phenotypic survey of industrial yeast elucidated that wine and wild yeasts are characterized by superior stress tolerance compared to beer yeasts (Gallone *et al.*, 2016). Endosome volume could also be differentially regulated in haploid and diploid cells.

Surface to volume ratio is a crucial parameter for organelle function (Chan and Marshall, 2012). The ratio of MVB outer membrane surface area to its total volume was similar for all strains we studied. This quantity could be limited by the mechanism of MVB biogenesis, where the outer membrane is constantly relocated to the lumen in the form of ILVs. Measurements of ILV number, volume, and surface area were not possible in this experiment due to their small size compared to section thickness. As a part of a collaborative project investigating the MVB biogenesis, we performed additional tomographic studies presented in Chapter 3.

2.8 Conclusion and Perspectives

We developed a protocol that allows the speeding up and parallelizing of electron microscopy experiments. We demonstrated its utility for a conventional CLEM experiment using fluorescent protein fusions and for a morphological screening experiment using different experimental conditions and genetic backgrounds.

Our protocol can be used for the parallelization of a wide range of yeast experiments using deletion mutants, stress conditions, and different drugs. Parallel processing of samples ensures a lack of bias from variations of conditions during fixation and embedding. Subsequent treatments, like immunogold labeling, can be applied to the ready sample in a highly reproducible way using the same antibody for systematically constructed tagged libraries. This workflow is developed by our collaborators in the M. Schuldiner laboratory (Weizmann Institute of Science). Their preliminary experiments demonstrated the feasibility of this approach.

A further increase of throughput can be achieved by modifying the protocol, though this can put forward the limitations imposed by the rate of high-resolution EM imaging. This can be avoided by designing a more complicated workflow, where high-resolution data acquisition is targeted more precisely using intermediate magnification or fluorescent imaging data. Automatic image analysis will be required to cope with increasing amounts of EM data. Extracting information from EM images is still challenging, but rapid progress in the area of image analysis and machine learning makes this problem solvable in the near future.

The protocol can be easily expanded to other model systems like mammalian or bacterial cells by using genetically encoded fluorescent barcodes or fluorescent stains. Our preliminary experiments, not included in this thesis, demonstrated that fluorescent conjugates of wheat germ agglutinin can be used in a similar way to barcode bacterial cells. Alternatively, high-throughput transformation with fluorescent proteins is accessible for a bacterial system as well.

We believe that this work will lay some foundation for expanding systematic screening and high-throughput imaging approaches to ultrastructural level using correlative light and electron microscopy.

2.9 Materials and Methods

2.9.1. Yeast strains

The yeast strains used in this study are listed in Table 2.5. The set of strains with mCherry fusions was a kind gift of the Michael Knop laboratory (University of Heidelberg). Wine yeast, S90 strain, and deletion mutants were provided by Natalia Gabrielli Lopez of the Kiran Patil group (EMBL, Heidelberg). Lsp1 and Abp1 fusions were obtained from the Marko Kaksonen group (EMBL, Heidelbderg, now University of Geneva).

Table 2.5. Yeast strains used in this work and their characteristics. GOI – gene of interest.

Name	**Properties**	**Source, Reference**
Ret1-mCherry	GOI::mCherry-SceIsite-Tcyc1-ScUra3-SceIsite-mCherryΔN-sfGFP can1Δ::STE2pr-Sp_his5 lyp1Δ::STE3pr-LEU2 MATa	Knop lab, (Khmelinskii et al. 2011)
Uso1-mCherry		
Gcs1-mCherry		
Sec13-mCherry		
Sfb3-mCherry		
Bug1-mCherry		
Arf1-mCherry		
Gea1-mCherry		
Sec18-mCherry		
Sly1-mCherry		
Emp24-mCherry		
Rer1-mCherry		
wt Y8205	MATa can1Δ::STE2pr-Sp_his5 lyp1Δ::STE3pr-LEU2	
Lsp1-mCherry Pil1-EGFP	MKY504, MATa his3200, leu2-3, ura3-53, lys2-801	Kaksonen lab, (Kaksonen, Toret, and Drubin 2005)
Abp1-mCherry	MKY0154, his3200, leu2-3, ura3-53, lys2-801	
S90	MATα GAL2	Patil lab, (Steinmetz et al. 2002)
PRICVV50	Lalvin EC1118, Commercial wine strain sold by Lallemand, diploid	Patil lab, (Novo et al. 2009)
SFB2	S.cerevisiae wine isolate	Patil lab
Δhog1	Strains from prototrophic yeast deletion collection.	Patil lab, (Mülleder et al. 2012)
Δtcb1		
Δvps35		
Δlpl1		

2.9.2. Cell growth

Cells were grown in YPAD medium or synthetic complete medium without tryptophan (SC-Trp). For parallel growths of more than 7 strains we used 24-well plates. To ensure equal gas exchange rate in all wells, the plate was sealed with a gas-permeable membrane (Sigma-Aldrich) and placed on a plate shaker set to 600 rpm to achieve proper mixing of the suspension. The shaker was in turn placed in a conventional incubator kept at 30°C. Most experimental cultures were inoculated from colonies on agar plates, grown overnight and in the morning diluted to OD_{600} 0.1-0.2. Diluted cultures were grown to OD_{600} 0.5-0.8 and then were stained.

2.9.3 Staining

We tested a number of dyes for staining yeast intracellular compartments (Table 2.1). All dyes were purchased from Life Technologies. We tested different concentrations and staining times similar to those recommended by the manufacturer. The critical condition for performance of hydrophobic dyes was the solution used to deliver them to cells. Using Diluent C (Sigma-Aldrich) or 9.25 % sucrose solution improved staining with CellTracker Orange and DiC12. However, none of the dyes proved to be useful for the barcoding protocol. For cell wall staining we purchased concanavalin a conjugated with Alexa Fluor® 350, Alexa Fluor® 488, Tetramethylrhodamine, and Alexa Fluor® 647 from Life Technologies. Stock solutions with concentration 2.5 mg/ml were prepared in phosphate buffered saline (PBS) and stored at -20°C in small aliquots. Con a conjugated to Cy7 stock solution was prepared using the following protocol (Mund *et al.*, 2014). Sulfo-Cy7 NHS ester (Lumiprobe) was diluted in dimethylsulfoxide (DMSO) to concentration of 10 mM. Concanavalin a (type IV, Sigma-Aldrich) 2.5 mg/ml solution was prepared in 0.2 M NaHCO3 with pH 8.2. Dye and protein solutions were mixed 6:100 and incubated for 4 hours at room temperature. Conjugated concanavalin was separated from the reaction on a disposable Sephadex G-25 column and buffer exchanged to PBS. The stock solution was stored frozen in

small aliquots. Before mixing of the staining solutions for barcoding, intermediate concanavalin stock solutions were produced.

2.9.4 EM sample preparation

We followed a standard sample preparation protocol used for in-resin CLEM (Kukulski *et al.*, 2012b). After staining, the yeast biomass was collected using a Millipore filtering setup on a 0.45 µm nitrocellulose filter. The cell slurry was transferred to the 0.1 mm deep cavity of a 0.1/0.2 mm aluminum membrane carrier for an HPM 010 high-pressure freezing machine. The cavity was covered by the flat side of a 0.3 mm carrier, and the sandwich was inserted in the HPM 010 and high-pressure frozen. Resin embedding was performed using a Leica AFS2 freeze-substitution machine equipped with a processing robot. Samples were embedded in Lowicryl HM20 resin using the standard freeze-substitution and embedding protocol outlined in Table 2.6. Dry acetone with 0.1 % uranyl acetate was used as the freeze-substitution medium (FS medium). The blocks were trimmed with a razor blade and 100 nm thick sections were produced using a Diatome 35° knife on a Leica Ultracut UCT or UC7 microtome. The sections were mounted on 200 mesh copper grids with continuous carbon support film (Electron Microscopy Sciences). Grids were imaged under the light microscope the same day.

2.9.5 Fluorescence microscopy

Fluorescence microscopy was performed using a protocol for in-resin CLEM imaging (Kukulski *et al.*, 2012b). The grid was sandwiched between two coverslips with a droplet of distilled water or PBS and mounted on the microscope stage using a holder. We used a Zeiss Cellobserver microscope to image all samples without Cy7 staining and a Leica AF7000 for imaging samples containing Cy7. Filter sets and other characteristics for each setup are outlined in Table 2.7. Usually, five to ten positions were imaged on each grid. Between those, exposure times and other conditions were kept the

same. After imaging, coverslips were separated and the grid was carefully recovered and dried. If the imaging was performed in PBS the grid was washed in distilled water after recovery.

Table 2.6. Freeze-substitution and Lowicryl HM20 embedding protocol for the Leica AFS2 machine used in this study.

Stage	**Tstart, °C**	**Tend, °C**	**Duration, h:min**	**Solution**	**Concentration**	**Action**	**Additional**
1	-90	-90	55:00	FS media	100%	stay	
2	-90	-45	9:00	FS media	100%	stay	
3	-45	-45	5:00	FS media	100%	stay	
4	-45	-45	0:10	Acetone	100%	exch/fill	
5	-45	-45	0:10	Acetone	100%	exch/fill	
6	-45	-45	0:10	Acetone	100%	exch/fill	
7	-45	-45	2:00	Lowicryl	10%	mix	aglt on
8	-45	-45	2:00	Lowicryl	25%	mix	aglt on
9	-45	-35	2:00	Lowicryl	50%	mix	aglt on
10	-35	-25	2:00	Lowicryl	75%	mix	aglt on
11	-25	-25	10:00	Lowicryl	100%	exch/fill	
12	-25	-25	10:00	Lowicryl	100%	exch/fill	
13	-25	-25	10:00	Lowicryl	100%	exch/fill	
14	-25	-25	48:00	Lowicryl	100%	stay	UV on
15	-25	+20	9:00	Lowicryl	100%	stay	UV on
16	+20	+20	24:00	Lowicryl	100%	stay	UV on

Table 2.7. Fluorescent microscopes and filters used in this study. For each filter set, excitation filter transmission range, dichroic mirror splitting wavelength and emission filter transmission range are given in nm.

	Zeiss Cellobserver	**Leica AF7000**
Objective	63X, Oil immersion	63X glycerol immersion, or 100X Oil immersion
Alexa 350 filter set	335-383, 395, 420-470	380-391, 436, 446-468
Alexa 488 filter set	450-490, 495, 500-550	484-504, 514, 520-540
TMR filter set	553-577, 585, 594-646	540-564, 570, 572-638
Alexa 647 filter set	625-655, 660, 665-715	630-640, 650, 690-750
Cy7 filter set	-	672-748, 750, 765-855

2.9.6 Electron microscopy

Prior to electron microscopy, grids were stained for 2 minutes in Reynolds lead citrate. EM imaging was performed on a TF30 electron microscope (FEI) operating at 100 kV, equipped with a Gatan OneView detector. SerialEM software was used for data collection (Mastronarde, 2005), and the detector was operated in the full frame mode (4096x4096 pixels). Regions imaged using light microscopy were localized and maps were produced at the medium magnification (pixel size around 5 nm). Each region contained one grid square and required a 5×5 to 7×7 montage to cover it completely. The resulting montages were saved as maps in the SerialEM Navigator file and used for identification of cells during the intermediate processing stage (see below). After processing, cell positions for high-resolution imaging were imported to the Navigator file and used to acquire a 2×2 montage of each cell with the pixel size 1 nm.

2.9.7 Image analysis and correlation

Cell detection

We used medium magnification montages to obtain positions and outlines of cells. Montages were blended using blendmont software from the IMOD package (Kremer *et al.*, 1996) to produce a single grid square overview. This overview was segmented using the pixel classification workflow in ilastik software (Sommer *et al.*, 2011). Ilastik was used to reliably distinguish well-preserved cells from resin, holes in resin where cells detached from it, and dark regions containing cell debris and grid bars. The segmentation was loaded into Matlab (Mathworks) and all processing was performed using custom scripts. Cell outlines were produced by smoothing the raw segmentation from ilastik using image opening operation and applying watershed segmentation. Cells were identified based on the object size and circularity. Outline and center coordinates for each cell were saved.

Fluorescence measurement

To measure the fluorescent signal on cell walls we used their positions (cell outlines) determined from the electron microscopy montages. The Matlab control point selection tool was used to correlate fluorescent and EM images and calculate the transformation between them. Affine transformation using 5-10 registration points was sufficient to overlay EM-derived outlines with fluorescent data and collect all signal for most cells. Outlines were converted to masks by a morphological dilation procedure. The intersections of masks with masks of neighboring cells and holes were subtracted from each mask to avoid measurement bias. Background was subtracted from fluorescent images using morphological opening operation.

Signal processing

Median intensity was measured for each cell in all fluorescent channels within the mask. Median was used instead of mean to reduce the contribution of outliers. To bring the values for different channels to similar ranges and distributions the values were normalized first for each channel by subtracting the minimum value and dividing all values by interquartile range. Interquartile range was used instead of minimum-maximum range because it better characterized the distribution shape and did not depend on outliers. Since all cells displayed a variable total amount of labeling, but the ratios between dyes in each population were constant, we normalized intensities for each cell by dividing all values for each cell by the value of the channel with maximal intensity. After the second normalization, k-means clustering was performed with the number of clusters corresponding to the expected number of color combinations. The coordinates of cells selected for high-resolution acquisition were imported to the SerialEM Navigator file. High-resolution montages were blended using blendmont, sorted according to their staining patterns and visually annotated. All data analysis was performed in Matlab.

2.9.8 Multivesicular body morphometry

Each cell micrograph was examined in IMOD without knowledge of its barcode. If an MVB was present on the cross section, it was approximated by eye as an ellipse and its major axis and minor axis perpendicular to it (as the widest place in the direction perpendicular to the major axis) were identified (Fig. 2.10B). An IMOD model was created with four points: (1) start of the major axis, (2) end of the major axis, (3) start of the minor axis, (4) end of the minor axis. These coordinates were imported in Matlab and used to calculate the length of the major and minor axis – D_1 and D_2 respectively. Area (A) and circumference (C) of each MVB cross section were calculated according to the following formulas:

$$A = \pi \frac{D_2 D_1}{4}$$

$$C = \pi \left[3\left(\frac{D_1}{2} + \frac{D_2}{2}\right) - \sqrt{\left(3\frac{D_1}{2} + \frac{D_2}{2}\right)\left(3\frac{D_2}{2} + \frac{D_1}{2}\right)} \right]$$

Areas of cell cross sections were determined from medium magnification montage segmented using ilastik (see above). The volume ratio of MVBs in total cell volume (V_r) was determined using a well-known stereology relation of cross-section area occupied by studied compartment to the total cell cross-section area using areas measured above instead of using traditional stereology point counts (Howard and Reed, 2005):

$$V_r = \frac{\sum A_{MVBs}}{\sum A_{cells}}$$

The standard error of this measurement was estimated according to the method described in Howard and Reed, 2005:

$$SE = V_r \sqrt{\frac{k}{k-1}\left\{\frac{\sum u^2}{\sum u \sum u} + \frac{\sum v^2}{\sum v \sum v} + \frac{\sum uv}{\sum u \sum v}\right\}}$$

Where k is a total number of cross-sections, and u and v are vectors with values of cell cross-section areas and MVB cross-section areas for each cell, respectively. Each summation is over 1 to k. MVB surface to volume area was

estimated as the relation of the sum of MVB cross-section areas to the sum of circumferences. Data processing and plotting were performed in Matlab, Libre Office Calc, and R (R Core Team, 2013).

Chapter 3. Ultrastructural analysis of multivesicular body biogenesis using correlative light microscopy and electron tomography

3.1 Introduction

Multivesicular bodies (MVBs) are organelles on the crossroads at the secretory, endocytic, and lysosomal pathways. They accept endocytosed material from the plasma membrane, and sort it either for recycling, degradation in lysosomes, or exosomal secretion. At the same time they play a crucial role in the biogenesis of lysosomes as transport intermediate for lysosomal proteins delivered from the trans Golgi network (TGN). In mammalian cells endosomal sorting of activated receptors plays important roles in signaling mechanisms, and the regulation of endosome maturation was found to be involved in the development of cancer, neurological, and infectious diseases (Hanson and Cashikar, 2012).

The general (simplified) picture of the endosomal pathway is similar in all eukaryotic cells (Fig. 3.1). Membrane and soluble material is taken up at the plasma membrane and delivered to the early endosome (EE). Some proteins and membrane components are recycled from it to the plasma membrane; endosomal proteins are delivered to it from the TGN and their transport receptors recycled back. Other proteins and membranes are sorted into intraluminal vesicles (ILVs) created by inward invagination of the endosomal membrane. The lumen of the endosome becomes acidified. An early

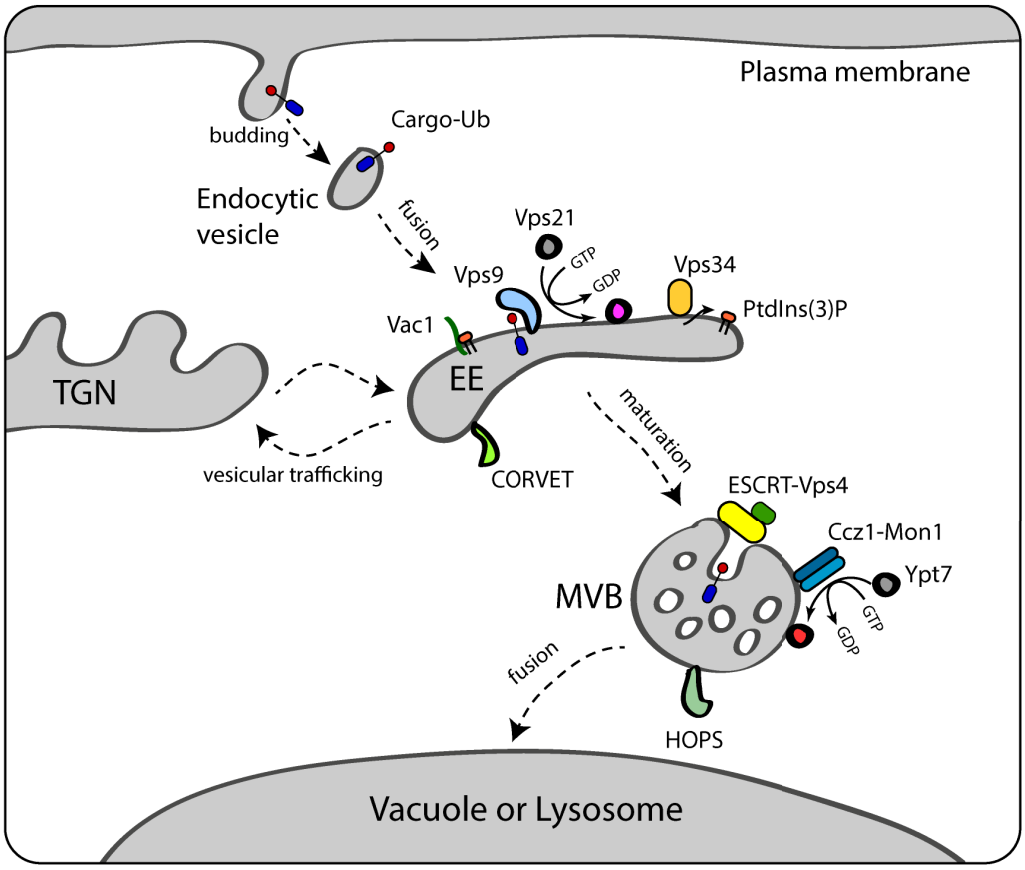

Fig. 3.1. Overview of the endosome maturation process based on yeast data. EE – early endosome, MVB – multivesicular body, TGN – trans Golgi network. Multiple trafficking pathways connecting TGN with late endosomes and vacuole are omitted for clarity. All protein names are in yeast notation. Explanations are available in the text.

endosome accumulates intraluminal vesicles and gradually matures into a late endosome (LE), fusing with the vacuole, where its contents are degraded. Alternatively, an endosome can fuse with the plasma membrane releasing ILVs as exosomes. "Multivesicular body" is a morphological term describing a rounded endosomal compartment containing intraluminal vesicles. The exact morphology of the endosome maturation intermediates, as well as the terms used to denote them, depends on the particular model system (Scott *et al.*, 2014).

In mammalian cells the early endosome is a complex tubular-vesicular compartment, constantly accepting endocytic vesicles delivered from the plasma membrane and endosomal proteins delivered from the TGN. Proteins recycled back to the plasma membrane are sorted into the tubules, while ILVs already start to form in the vesicular parts of the EE. In plants, the TGN takes

most of the early endosome functions, and MVBs mature directly from the TGN compartments (Contento and Bassham, 2012). The yeast endosomal system was proposed to be similar to the mammalian (Pelham, 2002; Bowers and Stevens, 2005), however comparisons should be made with care. The basic molecular mechanisms of the endosome maturation process are conserved in all eukaryotes. The budding yeast was one the most important model organisms for the identification of genes responsible for the functioning of the endosomal system. Many of them were first discovered as the *vps* mutants deficient in the delivery of vacuolar hydrolases to the vacuole (Raymond *et al.*, 1992).

The molecular identity of the endosomal pathway compartments is determined by Rab GTPases, which are the key regulators of the cellular endomembrane system (Hutagalung and Novick, 2011). Rab GTPases cycle between an active, GTP-bound state, and an inactive, GDP-bound state. Multiple accessory proteins regulate these transitions. GTP exchange factors (GEFs) promote dissociation of GDP and binding of GTP, which activates the GTPase. GTPase activation proteins (GAPs) promote GTP hydrolysis by Rabs, switching them to the inactive, GDP-bound state. Activated GTP-bound Rabs perform their function through a wide range of effector proteins (Cherfils and Zeghouf, 2013).

Two GTPases, Rab5 (Vps21 in yeast) and Rab7 (Ypt7 in yeast) are the key players in the functions of the endosomes. Rab5 localizes to early endosomes and is important for their subsequent maturation. Partial depletion of Rab5 in mammalian cells leads to reduction of the early endosome number (Zeigerer *et al.*, 2012). Rab5 GEF, Vps9 binds ubiquitinated proteins on the endosome cytoplasmic surface and mediates the localization and activation of Rab5 (Mattera *et al.*, 2006; Barr and Lambright, 2010). Activated Rab5 recruits Vps34, which produces PtdIns(3)P promoting binding of other effectors, such as the tethering factor Vac1 (ortholog of mammalian EEA1) . Vac1 promotes docking of endocytic vesicles to endosomes. Another tethering factor, multisubunit tethering complex CORVET, mediates fusion of endodomes with each other and with TGN-derived vesicles (Balderhaar and Ungermann, 2013;

Cabrera *et al.*, 2013). PtdIns(3)P and ubquitinated proteins recruit the ESCRT pathway components, which mediates formation of ILVs and protein sorting (Katzmann *et al.*, 2003).

The ESCRT pathway plays multiple roles in protein sorting and membrane remodeling processes, such as membrane scission during cytokinesis, virus budding, and MVB biogenesis (Henne *et al.*, 2011). The four ESCRT complexes (-0, -I, -II, and -III) are successively recruited to the membrane of the endosome to drive protein sorting and membrane remodeling to form an ILV (Katzmann *et al.*, 2001; Babst *et al.*, 2002; Hanson and Cashikar, 2012). ESCRTs are accompanied by a number of accessory proteins and complexes, including an AAA-type ATPase Vps4 (Babst *et al.*, 1997). Initially, Vps4 was reported to act in the ESCRT complex disassembly process (Katzmann *et al.*, 2001; Babst *et al.*, 2002). However, more recent data suggests that Vps4 can act during the whole ESCRT-driven membrane constriction process, not only at the end (Adell *et al.*, 2014). Consistent with this hypothesis, it was shown that during the cell division, Vps4 promotes membrane scission by dynamically remodeling ESCRT-III filaments (Mierzwa *et al.*, 2017). The deficiency of the ESCRT components, as well as Vps4, inhibits the formation of MVBs and the endosome maturation process. Vps4- and ESCRT-deficient yeast strains form so called class E compartments instead of endosomes. Class E compartments do not undergo maturation and comprise stacks of flattened cisternae accumulating a mix of early and late endosomal proteins. It was shown that endosome maturation process is disturbed in the class E compartments due to the massive hyper-activation of Rab5 by the ubiqutinated proteins accumulating on the endosomal membranes in the absence of the ESCRT-mediated sorting (Russell *et al.*, 2012). However the exact link between morphological transitions in endosomes and their Rab-governed maturation remains elusive.

The major event in the endosome maturation process is a switch from Rab5 to Rab7, which is thought to determine the transition from late to early endosomes (Rink *et al.*, 2005; Poteryaev *et al.*, 2010). Activated Rab5 recruits the Ccz1-Mon1 complex, the Rab7 GEF, promoting the Rab switch (Nordmann

et al., 2010). Transition to Rab7, in turn, drives recruitment of Rab7 effectors such as Fab1 PI3-kinase producing PtdIns(3,5)P(2) (Gary *et al.*, 1998), and substitution of the CORVET tethering complex with the HOPS complex. CORVET and HOPS have the same core subunits (Vps11, Vps16, Vps18, Vps33a/b). In addition to the core subunits, the CORVET complex includes Vps8 and the HOPS complex includes Vps39, TRAP1, and Vps41. When recruited, the HOPS complex switches the endosomal membrane fusion specificity to the vacuole (Balderhaar and Ungermann, 2013). The yeast endosome maturation process ends, when the MVB fuses with the vacuole and contents of the MVB are degraded in the lumen.

Despite budding yeast being one of the most productive model systems for the elucidation of the molecular mechanisms described above, relatively little is known about the morphology and spatiotemporal dynamics of its endocytic compartments. These topics were mostly addressed in the immunoelectron microscopy and fluorescent microscopy studies, the most relevant of which are reviewed below.

Early immunoelectron microscopy studies relied on tracing the progression of positively charged nanogold particles taken up by yeast spheroplasts (Prescianotto-Baschong and Riezman, 1998, 2002). These studies revealed that nanoparticles pass at least two types of compartments before reaching perivacuolar MVBs. Both compartments have similar tubular-vesicular ultrastructure, but differ in the SNARE proteins found on them. SNAREs (soluble N-ethylmaleimide-sensitive factor attachment protein receptor) are the key factors promoting the membrane fusion and the specificity of this process (Jahn and Scheller, 2006). First, nanoparticles arrived in compartments labeled with antibodies against the yeast SNARE Tlg1, and after this to the compartments containing Pep12 SNARE proteins. Perivacuolar MVBs were shown to react neither with anti-Tlg1, nor with anti-Pep12 antibodies. Due to the poor preservation of compartment lumen in such experiments, it was difficult to relate endosome maturation with the ILV biogenesis process on an ultrastructural level. More recent investigations using an improved sample preparation protocol confirmed previous results,

and additional tomographic studies visualized early endosomes as flattened cisternae (Griffith and Reggiori, 2009; Mari *et al.*, 2014).

Diffraction-limited and super-resolution fluorescent microscopy was used to study the yeast endosome maturation process (Puchner *et al.*, 2013; Arlt *et al.*, 2015). The diffraction-limited study followed the uptake of the fluorescently labeled α-factor, the yeast pheromone which is endocytosed and degraded in the vacuole. Arlt *et al.* (2015) revealed that almost all of the early endosomal factors, including ESCRT and Vps4 colocalize with cargo in the same time window, and the Ypt7-positive (the yeast Rab7 ortholog) late endosomes are relatively rare. Puchner *et al.* (2013) used super-resolution microscopy and molecule counting to measure endosome surface areas and PtdIns(3)P concentration in endocytic vesicles, early, and late endosomes. The study revealed that endosome maturation is accompanied by an increase in the PtdIns(3)P concentration without an increase in surface area until the Rab5/Rab7 conversion. After conversion to Rab7, the endosome surface area starts to increase while the PtdIns(3)P level stays constant (Puchner *et al.*, 2013). However a small number of endosomes was found to be Ypt7-positive already at low concentrations of PtdIns(3)P and a small surface area.

We used correlative light microscopy and electron tomography (Kukulski *et al.*, 2012b) to visualize morphology of Vps4-positive endosomes. This study was performed as a part of collaborative project investigating the role of Vps4 in MVB biogenesis and led by David Teis (Innsbruck Medical University). The results are submitted for publication (Adell *et al*.) and included in PhD thesis (Migliano, 2017). I performed all the work below except when explicitly stated.

3.2 Materials and Methods

3.2.1 Yeast strains

The Vps4-EGFP and Vps4-mNeonGreen yeast strains were generated by Simona Migliano (D. Teis laboratory) from wild type strain with the following

genetic background: Mat a leu2-3, 112 ura4-52 his3-Δ200 trp1-Δ901 lys2-801 suc2-Δ9 (Migliano, 2017).

3.2.2 Correlative Light and Electron Microscopy

The experiments were performed as previously described with minor modifications (Kukulski *et al.*, 2011; Suresh *et al.*, 2015). The Vps4-EGFP/Mup1-mCherry strain was grown in SD-Met media and the Vps4-mNeonGreen strain in SC-Trp at 30°C. Yeast were harvested by filtration and high-pressure frozen with the HPM010 (Abra Fluid AG). Samples were freeze-substituted into Lowicryl HM20 using the Leica AFS2 (a more detailed protocol is available in section 2.9.4 of this thesis). Blocks were sectioned and 200-300 nm thick sections were collected on 200 mesh copper grids with continuous carbon film (Electron Microscopy Sciences). TetraSpeck™ beads of 50 nm diameter (Invitrogen) were deposited on the sample surface to be used as markers for the correlation procedure. Grids were imaged on the Olympus IX81 inverted microscope equipped with 100×/1.45 objective and Orca-ER camera (Hamamatsu). Three channels (blue with excitation filter 377/50 nm, and emission filter 473/30 nm, green with excitation filter 470/22 nm, and emission filter 520/35 nm and red with excitation filter 556/20 nm, and emission filter 624/40 nm) were acquired for each field of view. Before electron tomography 15 nm protein A coated gold beads were applied on the section surface as fiducial markers for tomogram alignment, and the samples were contrasted with Reynolds lead citrate. Electron tomography was performed using the SerialEM software (Mastronarde, 2005) on the FEI F30 transmission electron microscope operated at 300 KV, equipped with the FEI Eagle 4K CCD camera and a dual tilt holder. For each spot the dual-axis high-magnification tomogram with pixel size 1.20 nm, tilt range -60° to +60°, and tilt angle increment 1° was acquired as well as a low magnification tomogram with the pixel size 2.59 nm, tilt range -60° to +60°, and tilt angle increment 2°. The tomograms were reconstructed and analyzed

using IMOD software package (Kremer *et al.*, 1996). Correlation was performed as described using Matlab (Kukulski *et al.*, 2012b).

3.2.3 MVBs morphology measurements

Selected MVBs were traced using IMOD. Outer surface area and total MVB volume were calculated using the utility programs provided in IMOD package (Kremer *et al.*, 1996). For ILV volume and surface area calculation, the model was converted in text form and processed in Matlab. For each ILV, a contour with the longest perimeter (P) was extracted and the ILV radius was estimated as $R = P/2\pi$. The radius was used to calculate the surface area and the volume of the ILV assuming it is spherical. Geometrical modeling of the MVB biogenesis was performed in Matlab. Plotting was performed in Matlab and Libre Office Calc.

3.3 Results

3.3.1 Fluorescence preservation after embedding

We performed CLEM analysis of the two yeast strains with Vps4 protein endogenously tagged with fluorescent proteins. One stain was tagged with EGFP and another with mNeonGreen characterized by better fluorescence and photostability (Shaner *et al.*, 2013). Yeast cells were high-pressure frozen, freeze-substituted in Lowicryl resin and sectioned. The section thickness was 250-300 nm. Light microscopy of these sections revealed multiple spot-like signals in the cells (Fig. 3.2). We found 187 spots in 1390 cross-sections. This translates to ~ 2 spots per 4 μm thick cell. Compared to 5-10 spots reported for living cells by D. Teis group (Migliano, 2017) and in literature (Arlt *et al.*, 2015) our data shows signal preservation about 20-50%.

Table 3.1. Statistics of the CLEM dataset.

	Total	Vps4-eGFP	Vps4-mNeonGreen
Cells studied	31	10	21
Number of spots	38	12	26
Cells without spots	4	2	2
MVB clusters without signal	11	3	8
MVBs in those	14	4	10
complete MVBs	2	1	1
MVB clusters with signal	36	11	25
MVBs in those	83	26	57
complete MVBs	15	8	7
Clusters associated with			
vacuoles	42	13	29
mitochondria	2	1	1
other organelles	15	7	8
Total clusters	47	14	33
Total MVBs	97	30	67
Total complete	17	9	8
Mean MVBs per cluster	2.1	2.1	2.0
Invaginations (MVBs quantified)	59 (87)	28 (24)	31 (63)
Mean invaginations per MVB	0.7	1.2	0.5

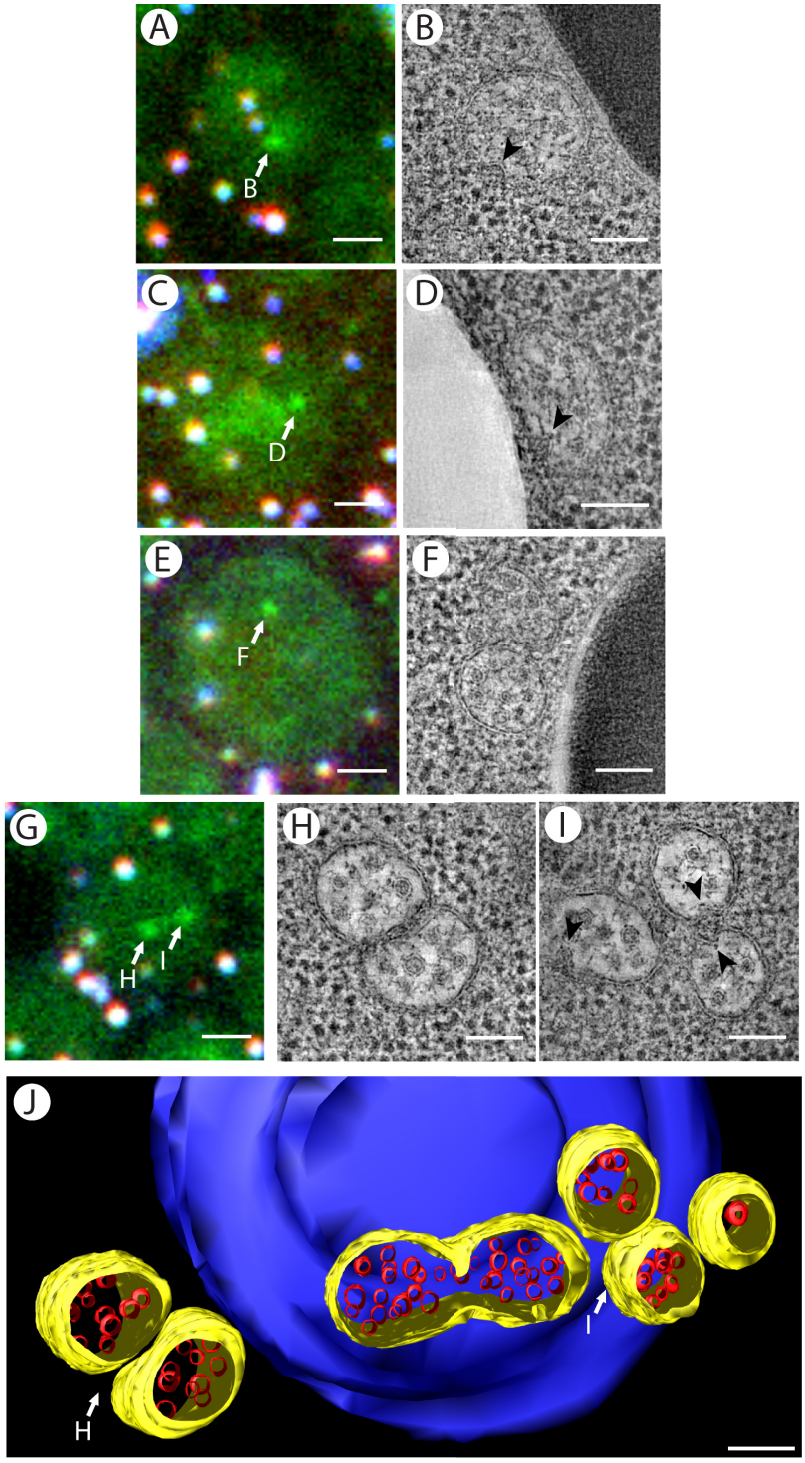

Fig. 3.2. Correlative light microscopy and electron tomography of Vps4-EGFP.
(A-I) Representative examples from the dataset. (A,C,E,G) Fluorescence composite images, Vps4-EGFP signal is in green, TetraSpeck beads used for correlation appear white in purple because they are fluorescent in green, red and blue channels. Sites of corresponding tomographic slices are marked with arrows; scale bar 1 µm. (B,D,F,H,I) Electron tomographic slices of the regions marked by white arrows in fluorescent data; membrane invaginations at the sites of ILV formation are marked with black arrowheads; scale bars 100 nm (J) 3D model of MVB cluster shown on panels G,H,I; MVB limiting membrane is shown in yellow, ILV membrane in red, vacuole in blue; MVBs corresponding to panels H and I are marked with arrows; scale bar 100 nm

3.3.2 MVBs associate with each other and with other organelles

We used electron tomography to analyze 38 fluorescent spots and regions without any signal in 31 cells (Table 3.1). One fluorescent spot usually correlated to more than one MVB clustered together (Fig. 3.2). We found 36 such clusters. In our tomographic dataset we additionally found 11 clusters without any fluorescent signal. The total 47 clusters contained 97 MVBs with the mean number of MVBs per cluster around 2. Most of the MVB clusters in our dataset were located in close proximity to vacuoles (around 90% of the clusters) but also contacted other organelles like mitochondria and ER (Table 3.1, Fig. 3.3A). We found three examples of MVBs contacting unknown fenestrated cisterna. We suggest that it might be the TGN or the early endosome (Fig. 3.3B-E).

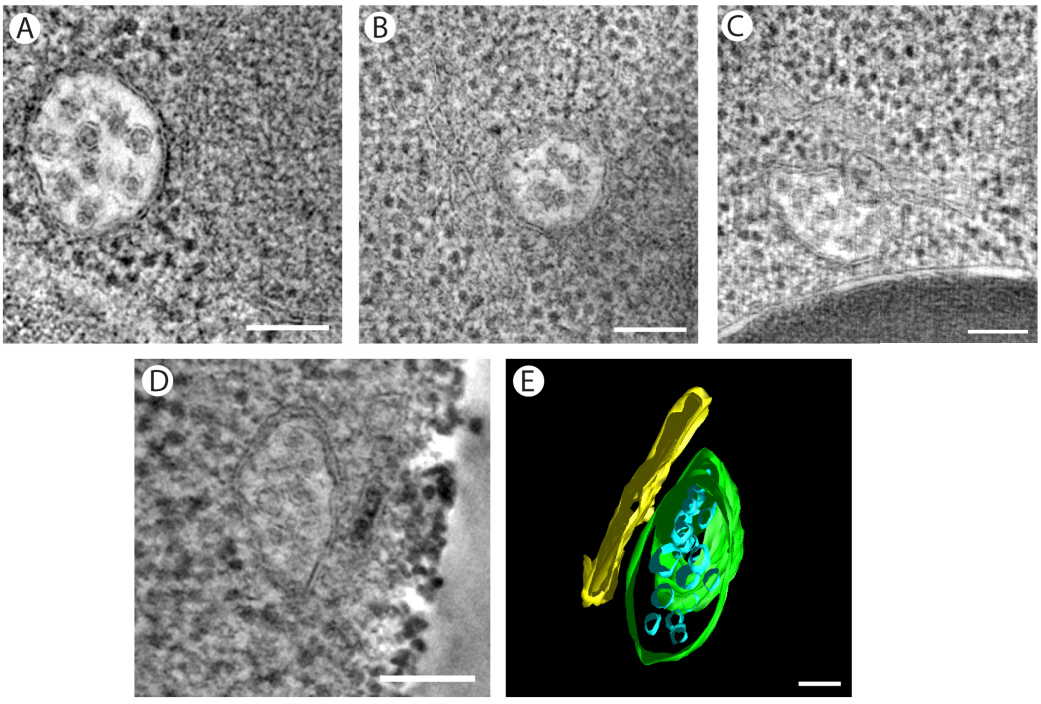

Fig. 3.3. Contacts made by MVBs. (A) tomographic slice of the MVB (left) found in a close proximity to the mitochondria (right). (B-D) Tomographic slices of MVBs contacting with unidentified cisterna. (E) 3D model of MVB and accompanying cisterna depicted on panel D; the MVB limiting membrane is shown in green, ILVs are shown in blue, the membrane of the cisterna is shown in yellow. Scale bars are 100 nm.

3.3.3 ILV formation quantification

We quantified the number of MVB membrane invaginations found in our dataset. These invaginations are likely to be intermediates of the ILV formation (Table 3.1, Fig. 3.2). The mean number of invaginations per MVB was 0.7, and MVBs with more than one invagination were very rare (Fig. 3.4A). Electron tomography does not allow us to clearly visualize top and bottom surfaces of MVBs due to the missing wedge artifact. This can decrease observed number of membrane invaginations, so we estimate the actual mean number of invaginations per MVB to be around 1. A large number of MVBs with invaginations proves that our analysis includes maturing MVBs actively performing membrane protein sorting. Mean radius of ILVs was 13±3 nm (±SD, N=329 ILVs) with distribution close to normal (Fig. 3.4B). The radius is consistent with the value 12 nm reported in epoxy-resin embedded yeast cells (Adell *et al.*, 2014). An interesting example of two MVBs contacting each other at the sites of ILV formation suggests that in some cases the formation of ILVs can be spatially coordinated on the neighboring endosomes (Fig. 3.2I).

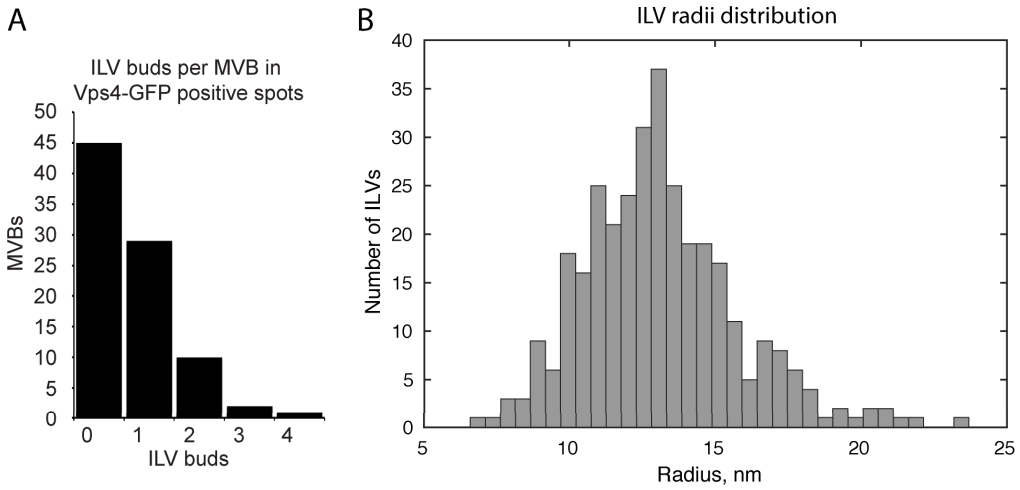

Fig. 3.4. Morphology of MVB membrane buds and ILVs. (A) Number of MVBs with different numbers of outer membrane invaginations; MVBs with no or one invagination comprise most of the population, while MVBs with more than one invaginations are relatively rare. (B) Distribution of ILV radii measured by tracing the ILVs in IMOD and calculating the radius from the area of the largest model contour; N=329.

3.3.4 3D modeling of MVBs

We created 3D models for a number of MVBs to measure their morphological properties (Fig. 3.1J, Fig. 3.3E). We selected a small subset of MVBs completely or almost completely contained in resin and calculated their outer surface areas, volumes, numbers of ILVs, and volume fractions of ILVs in the total MVB volume. The number of ILVs per MVB varied from 1 to more than 60, showing preference for smaller MVBs, because of the completeness requirement. The total volume and surface area of the MVBs scaled rather

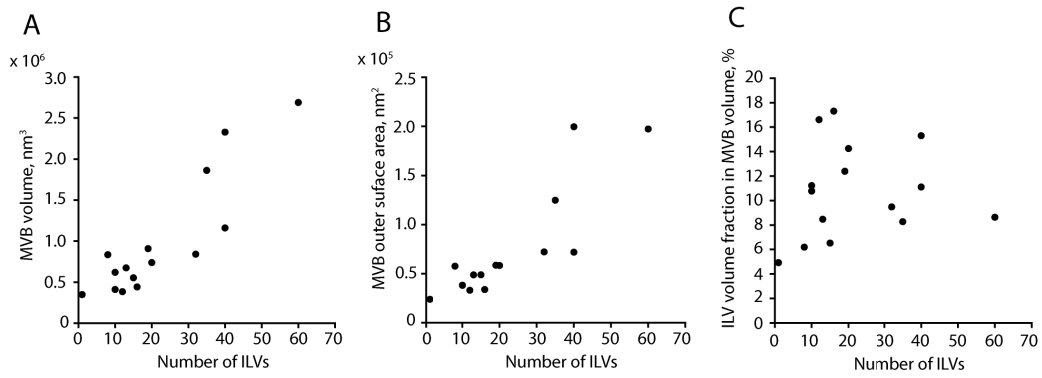

Fig. 3.5. Quantification of 3D-modelled MVB parameters. Data for the selected population of MVBs, which are completely, or almost completely contained within the section (A) Scatter plot of MVB volume against the number of ILVs. (B) Scatter plot of MVB surface area against the number of ILVs. (C) Scatter plot of the relation between the number of ILVs and their fraction in the total MVB volume.

linearly with the increasing number of ILVs (Fig. 3.5A,B). The ILV volume ratio did not show any clear dependence on the ILV number (Fig. 3.5C). Our dataset includes MVBs with just few ILVs, but they are proportionally smaller than large MVBs indicating that ILVs form very quickly during the MVB biogenesis, not leaving 'unused' any outer MVB membrane that can be sorted to the ILVs.

3.3.5 The geometrical model of MVB formation

We propose a simple geometrical model, which can help to study ILV formation in maturing MVBs (Fig. 3.6A). We make the following assumptions. Significant amounts of water do not cross membranes during the organelle biogenesis. This means that changing the organelle volume without changing

membrane surface area is not possible. Membrane components are not synthetized *de novo* in the endosomal system. This means that changing membrane surface area without changing the organelle volume is also not possible as well. A perfectly spherical organelle cannot form an outward as well as an inward bud and has the highest possible luminal volume to outer surface ratio because the membrane is not stretchable. Two spherical organelles can fuse and make a non-spherical organelle, which can form buds again. MVBs form mostly from the endocytic vesicle-derived membranes. Endocytic vesicles fuse and form an endosome with total volume $V_{EV}\times N_{EV}$ and surface area $S_{EV}\times N_{EV}$, where N_{EV} is the number of vesicles and V_{EV} and S_{EV} are volume and surface area of one vesicle respectively. According to Kukulski *et al.* (2012a) yeast endocytic vesicles are ellipsoids (not spheres) with mean volume 4.3×10^5 nm^3 and surface area 6.4×10^3 nm^2. When several ILVs (N_{ILV}) are budding inwards, the volume of the whole organelle is increasing (ILV is filled with cytoplasm during budding) and the resulting MVB will have the volume

$$V_{MVB} = V_{EV}N_{EV} + N_{ILV}V_{ILV} \qquad (1)$$

where V_{ILV} is the mean volume of one ILV (calculated from the mean radius assuming these are spheres, Fig. 3.4B). Outer surface area (S_{MVB}) of an MVB decreases after the ILV formation (the total MVB surface area is $S_{EV}\times N_{EV}$ and remains constant):

$$S_{MVB} = S_{EV}N_{EV} - N_{ILV}S_{ILV} \qquad (2)$$

ILV budding can go on until the outer membrane of the MVB becomes spherical. This means that for the certain volume, achieved by the MVB, the minimal surface area is

$$S_{MVBmin} = 4\pi\left(\frac{3}{4\pi}V_{MVB}\right)^{\frac{2}{3}} \qquad (3)$$

Expressions (1) and (2) define a plane in the space with axes V_{MVB}, S_{MVB} and N_{ILVs}:

$$0 = \mathbf{V_{MVB}} - \frac{V_{EV}}{S_{EV}}\mathbf{S_{MVB}} - (V_{ILV} + \frac{V_{EV}S_{ILV}}{S_{EV}})\mathbf{N_{ILVs}} \qquad (4)$$

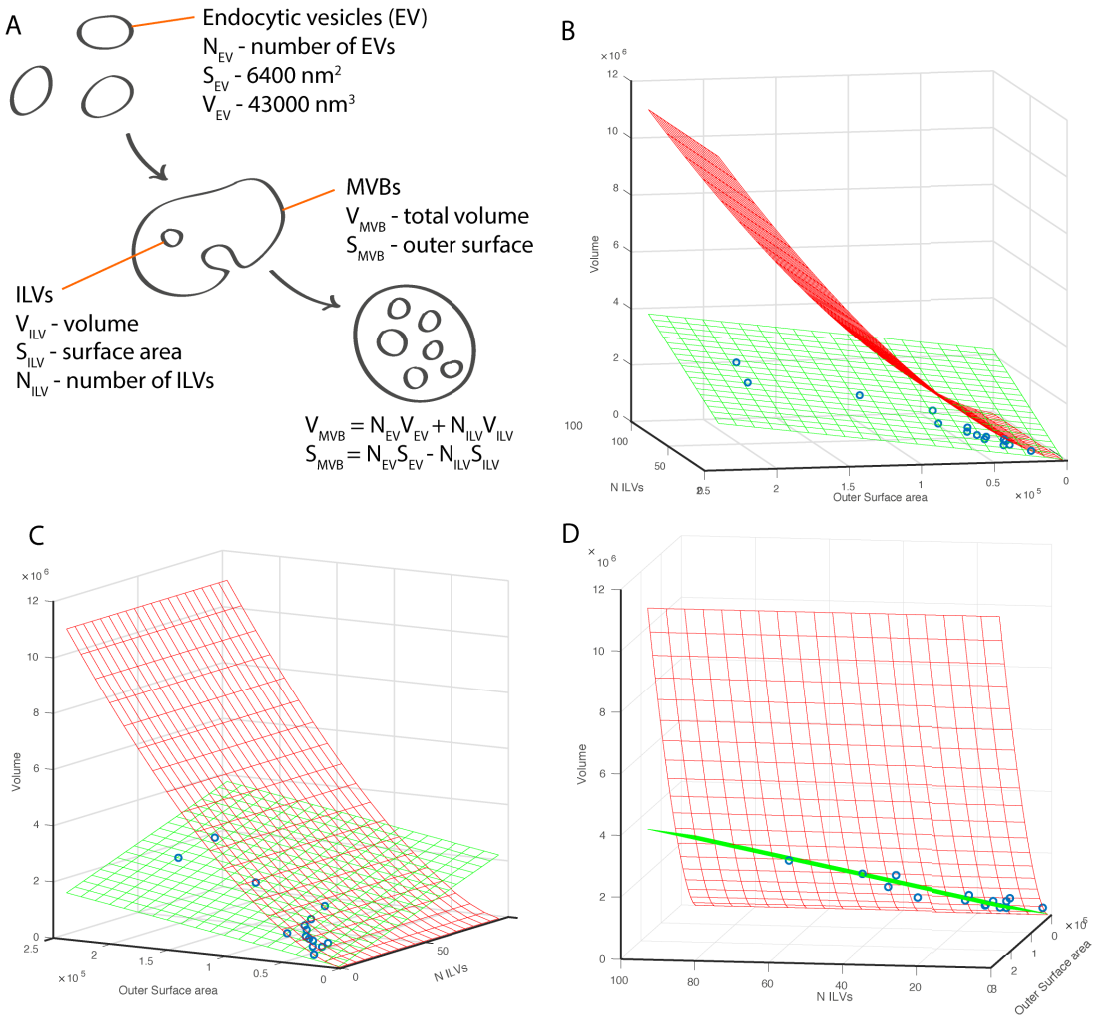

Fig. 3.6. Geometrical model of MVB maturation. (A) Schematic depiction of MVB formation from endocytic vesicles; names of variables and parameters are denoted; see text for additional explanation. (B-D) Different views on 3D scatter plot of MVB outer surface area, total volume and number of ILVs; experimental data points are shown in blue; plane that is defined by surface areas and volumes of endocytic vesicles and ILVs is shown in green; surface separating forbidden outer surface to volume ratio (less than a sphere) is shown in red and does not depend on ILV number; additional discussion is available in the text.

Coefficients for the plane are defined by the sizes and surface to volume ratios of the endocytic vesicles and the ILVs. This plane can be plotted in 3D (Fig. 4B-D, shown in green). The "restricted" area ("more spherical than a sphere") can be depicted according to (3). The border of this area is shown as the red curved plane on Fig. 3.4B-D. All structures formed by the fusion of endocytic vesicles, budding of ILVs and subsequent fusion of the resulting structures should lie on the green plane outside of the area cut out by the red plane. Movement along the green plane in different directions represents either

fusion of MVBs (increase of V_{MVB}, S_{MVB} and N_{ILVs}), endocytic vesicles (increase of V_{MVB}, S_{MVB}), or ILV budding (increase in V_{MVB} and N_{ILVs}, decrease of S_{MVB}). An ILV budding event brings the data point closer to the red plane.

We plotted the morphological data of the MVBs described in section 3.3.4 along with the model (Fig. 4B-D). Most of the points are concentrated close to the axis origin and it is difficult to determine, how well they fit the plane. However points corresponding to larger structures demonstrate a good agreement with the model. Interestingly, smaller MVBs are closer to spherical shape (close to the intersection of red and green planes), while larger MVBs are further from it. At this dataset size, our data show consistency with the proposed model, but a larger dataset is needed for further validation of the model.

3.4 Discussion

3.4.1 The role of Vps4 in the MVB biogenesis

Using correlative light microscopy and electron tomography, we visualized morphology of the maturing MVBs in budding yeast cells. On average, MVBs in our dataset had 0.7 invaginations in the limiting membrane. Accounting for the missing wedge artifact, which by our estimates obscures the morphology of 20-30% of the MVB limiting membrane and does not allow detection of any invaginations on the 'top' and 'bottom' surfaces, we can estimate this number as close to 1, indicating that most of MVBs in our dataset are actively maturing and sorting cargo in their lumen. An average number of one invagination per MVB and the small number of MVBs with more than one invaginations suggests that in most of the MVBs ILV formation occurs in sequential manner. Light microscopy resolution and correlation precision were not high enough to correlate the presence of Vps4 with the particular budding stage.

Our finding that Vps4-positive MVBs are forming invaginations and sort cargos to the ILVs was used to complement the live tracking of individual

Vps4-positive spots produced in the D. Teis laboratory. Live tracking showed that Vps4 formed two types of spots in the yeast cytoplasm. The first type was highly mobile and contained around 20 Vps4 molecules. The second type of spot contained more Vps4 molecules (20-70), was localized near the vacuoles and was less mobile (Migliano, 2017). Simultaneous live tracking of Vps4 and the ESCRT complex components showed that they are recruited to the endosomal membrane, not sequentially, but at the same time and demonstrate a high exchange rate with the cytoplasmic pool of the ESCRT components and Vps4. Our CLEM experiments were used to confirm that the EGFP-tagged Vps4 fully retains its functions and localizes to the MVBs, actively forming ILVs and performing protein sorting. The live imaging experiments complemented with our CLEM data lead to the conclusion that Vps4 acts during the whole process of bud formation by actively remodeling the ESCRT-III filaments, similar to the proposed role of Vps4 in cell division, and contrary to the previous hypothesis suggesting that Vps4 is a disassembly factor for the ESCRT machinery acting at the end of the ILV budding process (Mierzwa *et al.*, 2017; Migliano, 2017).

3.4.2 Yeast endosome maturation and morphology

Most of the MVBs we visualized using correlative microscopy of the fluorescently labeled Vps4 were close to spherical shape, and contained ILVs. We did not find neither any tubular-vesicular compartments described in the immuno-EM studies as early endosomes (Prescianotto-Baschong and Riezman, 2002; Griffith and Reggiori, 2009), nor any possible morphological intermediates between such tubular-vesicular endosomes and round MVBs (Fig. 3.7A). By live imaging, Vps4 was found on the early endosomes very shortly after the endocytosis (Arlt *et al.*, 2015), so the absence of tubular-vesicular early endosomes in our CLEM dataset is not explained by the absence of fluorescent Vps4 on them. We propose two possible explanations. Either Vps4-EGFP signal of the early endosomes is not retained after the resin

embedding, or the early endosomes do not have the morphology we expect based on the immuno-EM studies.

The lack of early endosome-like compartments in our data can be explained by relatively low fluorescent signal preservation after the resin embedding. It is reasonable to assume that most of the signals that survived the embedding and were imaged by CLEM belong to the second class of brighter, immobile Vps4-EGFP spots described by live imaging (see section 3.4.1). The mean amount of EGFP molecules found in mobile spots by live microscopy (around 20) is right on the edge of the sensitivity of the in-resin CLEM method we used (Kukulski *et al.*, 2011). The overrepresentation of immobile, perivacuolar Vps4 spots in our dataset is confirmed by the observation that most of the MVB clusters we imaged are localized in close proximity to the vacuole (Table 3.1). We reasoned that we could localize the structures missed by the CLEM analysis, purely based on their morphology, since the presence of intraluminal vesicles is an unambiguous feature. We analyzed the whole tomographic dataset and found additional structures containing ILVs but not having any detectable Vps4-EGFP signal. The morphology of these structures was not distinguishable from the other MVBs in our dataset and all of them had mostly round shape. This prompted us to hypothesize that either; the tubular vesicular endosomes quickly fuse directly with the MVBs without undergoing the long maturation process (the EE-MVB fusion hypothesis, Fig. 3.7B), or the large early endosomes described by immuno-EM do not form under our experimental conditions (Fig. 3.7C).

The EE-MVB fusion hypothesis suggests that there is no intermediate compartment between the tubular-vesicular EE, but the tubular-vesicular EE can associate with more mature MVBs and quickly fuse with them (Fig. 3.7B). The contacts between MVBs and unknown cisternae we observed can represent such intermediates (Fig. 3.3B-E).

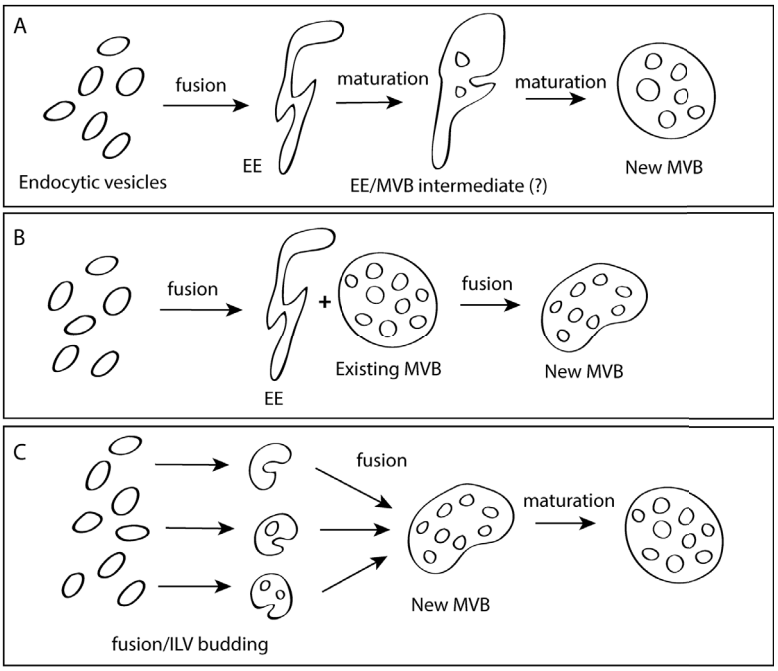

Fig. 3.7. Possible maturation routes of yeast endosomes. (A) Large tubular-vesicular endosomes (200-400 nm long) gradually mature by forming ILVs to become rounded MVBs. (B) Large tubular-vesicular endosomes quickly fuse with already formed MVBs (C) Endocytic vesicles start fusing with each other and form ILVs as soon as there is enough outer membrane, and later fuse to form large MVBs that continue slow maturation by forming ILV at relatively slow speed.

The second hypothesis we propose, suggests that relatively large (200-400 nm long) early endosomes described in the earlier immune-EM studies do not form under our experimental conditions. In immuno-EM studies that accurately follow the progression of gold nanoparticles inside the cells, endocytosis was blocked by low temperature and then resumed by shifting the temperature back to normal (Prescianotto-Baschong and Riezman, 1998, 2002). This could cause a temporary increase in the size of the early endosomes. We propose that under normal early log phase growth conditions used in our study, fused endocytic vesicles form ILVs as soon as the resulting endosome has enough bounding membrane to be internalized, and become round relatively quickly without forming large tubular-vesicular compartments (Fig. 3.7C). This hypothesis is supported by a relatively linear increase of the MVB size with the increase of ILV number we observed, and by the presence of small round MVBs in our dataset.

It is also possible that yeast endosome maturation process can represent a combination of the maturation paths represented on Fig. 3.7. Depending on

the physiological state the endosome maturation can preferentially take different paths determining the morphology of the early endosomes and MVBs.

We developed a geometrical model to characterize the morphology and maturation route of the MVBs. Our model takes into account surface areas and volumes of the fusing endocytic vesicles, as well as of the ILVs, and predicts that all structures formed by the means of fusion of the endocytic vesicles, ILV budding and fusion of resulting MVBs will lie on a certain plane in the coordinate system of number of ILVs, outer MVB surface area, and full MVB volume. The model also suggests that there is a limit to the outer surface to volume ratio, when the outer surface of the MVB is spherical and cannot form an invagination any more. We compared the parameters of the MVBs in our dataset and found that at this dataset size they are consistent with the model predictions. We also found that the subpopulation of the small MVBs have the outer membrane surface shape close to spherical while larger MVBs with more ILVs tend to be less spherical.

The surface areas of the MVBs in our dataset are comparable with the surface areas of the maturing endosomes determined by super-resolution light microscopy (Puchner *et al.*, 2013). Interestingly, small round MVBs (close to spherical shape, Fig. 3.4B-D) in our dataset correspond to the size of Vps21 positive endosomes in the super-resolution study (surface area below 1×10^5 nm^2), while larger MVBs from our dataset with less spherical shape are closer to the size of Ypt7-positive endosomes from the super-resolution study. This is consistent with the model proposed by Puchner *et al*. 2013 in which Vps21-positive endosomes undergo the transition to Ypt7-positive and generate larger compartments by fusion with each other. How this transition occurs and how it is linked with the early morphology remains unclear and requires further investigation. We believe that the model we introduced can be useful for the visualization of the morphological transitions occurring during MVB maturation and can help to reveal the role of ILV budding, MVB-MVB fusion, and MVB-endosome fusion in this process. In Chapter 2 we found that the total volume of MVBs can be dramatically different in different strains. We

believe that the question of how this parameter is regulated during MVB biogenesis can be also addressed using the model we described combined with CLEM and live imaging experiments.

Chapter 4. *In situ* structural analysis of the *Chlamydomonas reinhardtii* COPI coat

4.1 Introduction

The transport of components between cellular compartments by vesicular trafficking is one of the central mechanisms of eukaryotic cells. Three conserved archetypal protein coats, COPI, COPII and clathrin, mediate the formation and function of trafficking vesicles in the endocytic-secretory pathway (Bonifacino and Glick, 2004). These coats share organizational and functional principles and are likely to have diverged from an ancestral coat prior to the last common eukaryotic ancestor. The COPII coat is responsible for transporting synthetized proteins from the endoplasmic reticulum (ER) to the Golgi apparatus, clathrin acts in endocytosis and in cargo trafficking from the trans-Golgi network (TGN), and the COPI coat mediates intra-Golgi trafficking and retrieval of ER-resident proteins back to the Golgi (Malhotra *et al.*, 1989; Letourneur *et al.*, 1994).

COPI is recruited to the membrane as heptameric complex, coatomer, by interaction with the small GTPase Arf1 (Fig. 4.1). By analogy with the clathrin and COPII coats, coatomer incorporates a coat-like and an adaptor-like subcomplex. The coat-like subcomplex of COPI consists of ε, α, and β subunits, the latter two of which have a "proto-coatomer" architecture characterized by N-terminal β–propellers combined with extended α–solenoids. This combination, thought to represent an ancestral coat module, is also found in the clathrin heavy chain, the Sec31 COPII coat subunits, and some nuclear

pore components (Devos *et al.*, 2004; Promponas *et al.*, 2016). The COPI adaptor-like subcomplex consists of γ, ζ, β, and δ subunits and is a homolog of AP1 and AP2 clathrin adaptor complexes (Schledzewski *et al.*, 1999). Extensive crystallographic studies of coat subunits confirmed these similarities (Watson *et al.*, 2004; Yu *et al.*, 2009, 2012; Hsia and Hoelz, 2010; Lee and Goldberg, 2010; Jackson *et al.*, 2012; Ma and Goldberg, 2013; Lunev *et al.*, 2017). Cryo-electron tomography (cryo-ET) and subtomogram averaging (Briggs, 2013) has been applied to study COPI-coated vesicles assembled *in vitro* resulting in a complete molecular model of the coat assembly (Faini *et al.*, 2012; Dodonova *et al.*, 2015). Within the assembled coat, three copies of coatomer and six copies of Arf1 form a three-fold triad structure in which the coat-like and adaptor-like subunits form intertwined arches. This arrangement is not consistent with a functional-subdivision of coatomer into coat and adaptor. Triads are clustered together on the membrane surface to form vesicles with variable size and shape.

Disassembly of the coat after budding is triggered by GTP hydrolysis catalyzed by Arf1 and regulated by the GTPase activating proteins (GAPs). Three ArfGAPs found in mammalian cells have been assigned partially overlapping functions. ArfGAP1 was suggested to play a role in vesicle assembly, cargo sorting, and uncoating while ArfGAP2/3 were suggested to be important mostly for the uncoating process (Weimer *et al.*, 2008; Hsu *et al.*, 2009; Popoff *et al.*, 2011). The dynamics of disassembly are poorly understood and open questions include: what is the timing of GTP hydrolysis relative to budding; do membrane dissociation of Arf1 and disassembly of coatomer occur simultaneously; and does the coat disassemble gradually or en masse (Fig. 4.1).

COPI-mediated transport is essential for maintaining the polarized structure of the Golgi apparatus that ensures directional processing and sorting of secretory cargos (Bonifacino and Glick, 2004; Beck *et al.*, 2009; Glick and Nakano, 2009; Popoff *et al.*, 2011). Traditionally the Golgi apparatus is subdivided into *cis*, *medial*, and *trans* regions. The Golgi architecture can vary between different species (Mironov *et al.*, 2016). The diversity of COPI

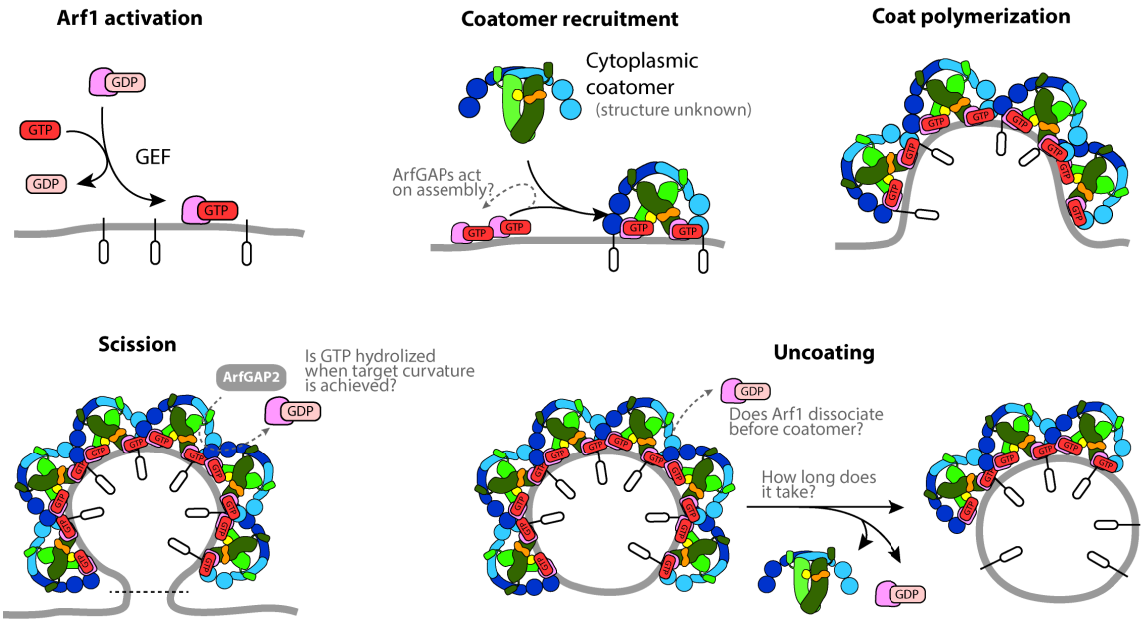

Fig. 4.1. COPI vesicle lifecycle and open questions. COPI bud formation starts with recruitment of Arf1 small GTPase (pink) to the membrane. Arf1 bound to GTP is activated by exchanging GDP with GTP. Arf1-GTP can bind membranes. At the membrane Arf1 recruits COPI complex from the cytoplasm, where it already exists as heptamer. Both subcomplexes ('coat subcomplex', which consists of α-COP, ε-COP, and β'-COP, shown in blue, and 'adaptor subcomplex', which consists of β-COPI and γ-COP (green), and ζ-COP and δ-COP, shown in yellow and orange) are recruited at the same time and bind cargo molecules. Coat polymerization occurs when multiple coatomer complexes bind the membrane. Coat induces curvature and a bud is produced. It was proposed that at this stage GTP can be hydrolyzed induced by ArfGAP2 sensing membrane curvature. Mechanism of bud neck scission is not fully understood. Vesicle undergoes uncoating, kinetic and order of this process is not fully understood.

function, including retrieval of ER resident proteins from the *cis* Golgi back to the ER, retrograde transport of Golgi resident proteins within the stack, and a suggested role in anterograde trafficking (Yang *et al.*, 2011; Day *et al.*, 2013; Lavieu *et al.*, 2013; Jackson, 2014; Papanikou and Glick, 2014; Mironov *et al.*, 2016) has lead to the hypothesis that there are different types of COPI vesicles. Biochemical and microscopic studies have grouped COPI vesicles based on their donor compartment, cargo load, possible transport direction, isoform composition, and morphology (Orci *et al.*, 1997; Lanoix *et al.*, 2001; Malsam *et al.*, 2005; Donohoe *et al.*, 2007, 2013; Moelleken *et al.*, 2007; Bouchet-Marquis *et al.*, 2008). Analysis of the Golgi apparatus in the green alga *Scherfellia dubia* using electron microscopy of cryo-fixed, freeze-substituted, stained, plastic-embedded samples, revealed two types of COPI vesicles (Donohoe *et al.*, 2007, 2013). Vesicles termed COPIa had a lightly stained content and surrounded the *cis*-region of the stack. COPIb vesicles

were found near the *medial* region, and had a strongly stained lumen, reflecting the strongly stained lumen of medial cisternae. The TGN and *trans* Golgi region in *S. dubia* contained translucent cisterna and round translucent vacuoles. Vesicles budded from the last cisternae were characterized as separate secretory type basing on their morphology (Donohoe *et al.*, 2007). Cryo-electron microscopy of vitreous sections of mammalian cells did not reveal COPIa and COPIb subgroups. Instead, one group of vesicles and buds were observed to have a 'spiky' coat morphology while another group had a smoother, more homogeneous coat (Bouchet-Marquis *et al.*, 2008). Coat morphology was not related to position within the Golgi.

Cryo focused ion beam (cryo-FIB) can be used for milling of vitrified samples to generate thin lamella through the centers of cells which are accessible for cryo-electron microscopy (Rigort *et al.*, 2012b). By imaging these lamellae by cryo-electron tomography, 3D reconstructions of crowded cellular environment can be produced, revealing the positions and relationships of cellular components (Lučić *et al.*, 2005; Asano *et al.*, 2015a; Beck *et al.*, 2016). This approach has been previously applied to image the Golgi apparatus of *Chlamydomonas reinhardtii*, revealing the presence of ordered intracisternal arrays that may help maintain Golgi structure (Engel *et al.*, 2015). Here we have combined cryo-FIB milling, cryo-ET, and subtomogram averaging to study the structure, distribution, and variability of the COPI coat within the Golgi apparatus. In this way, we have determined the structure of the COPI coat *de novo,* from within intact cells. The structure validates the previously determined *in vitro* structure and extends it by revealing how COPI vesicle heterogeneity reflects the polarized structure of the Golgi apparatus. This work was performed in collaboration with Ben Engel (Max Planck Institute of Biochemistry, Martinsried). Sample preparation, data collection, and tomographic reconstruction were performed by B.Engel, M.Schaffer, and S.Albert. I performed all COPI structural analysis described in this Chapter and wrote the text.

4.2 Results

4.2.1 The structure of the assembled COPI coat in cells

Chlamydomonas reinhardtii cells were vitrified on electron microscopy grids by plunging into liquid ethane. Flat and thin (100-200 nm) lamellae were machined from the cells using cryo-FIB milling, and cryo-electron tomograms were collected at positions where the lamella contained Golgi stacks. In this way, we generated three-dimensional reconstructions of the Golgi, within cells in their near-native state.

We selected tomograms in which the ultrastructure of the Golgi apparatus could be seen (Fig. 4.2A). The arrangement of the *C. reinhardtii* Golgi is very stereotypic. On the *cis* side, the Golgi opposes the ER. On the *trans* side, the Golgi cisternae transform into round vesicular structures which we assign as trans-Golgi network (TGN). The archetypal protein coats can all be visually

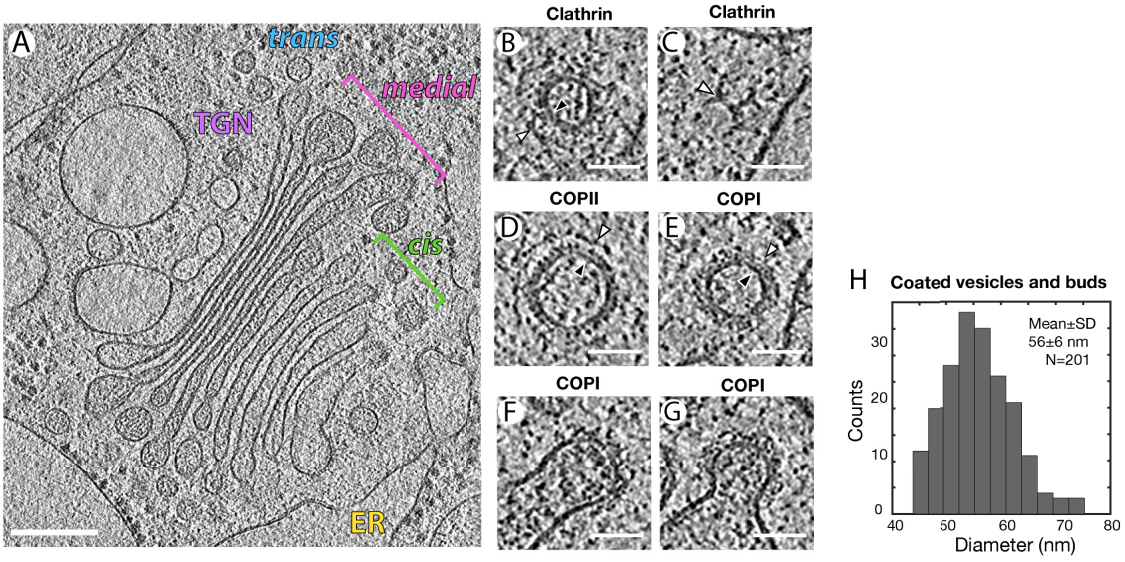

Fig. 4.2. The morphology of the *Chlamydomonas* Golgi apparatus and transport vesicles revealed by cryo-FIB and cryo-ET. (A) A slice through a tomogram of a representative Golgi apparatus: endoplasmic reticulum (ER) is on the *cis* side, TGN is on the *trans* side, cisternae are labeled *cis*, *medial*, or *trans* based on morphology and position. (B - G) Slices through transport vesicles within the tomograms. Empty arrowheads mark the extent of the coat on the cytoplasmic side, filled arrowheads mark the vesicle membrane: (B) clathrin coated vesicle central slice, (C) clathrin coated vesicle coat triskelion, (D) COPII vesicle. (E) COPI vesicle (F) Example of a COPI bud at the intermediate stage. (G) Example of a COPI bud at the late budding stage with a clearly visible neck. (H) Membrane diameter distribution for COPI late buds and vesicles. Scale bars are 200 nm in A, and 50 nm in B-G

identified in the tomogram: clathrin coated vesicles can be found in the vicinity of the TGN (Fig. 4.2B,C), while ER exit sites with COPII buds and vesicles can be distinguished by their two-layered coat (Fig. 4.2E). Multiple COPI coated vesicles and buds are found around the edges of the Golgi cisternae and can be discriminated from clathrin and COPII coated ones by the presence of a dense uniform coat.

From 29 tomograms, we identified 267 buds and vesicles showing extensive COPI coats (Fig. 4.2D-F). We measured the diameters of late buds (have necks, Fig. 4.2F) and vesicles, and compared the diameter distribution with that previously measured from cryo-ET of *in vitro* reconstituted COPI budding reactions. In the cell, the mean (±SD) diameter to the membrane was 56 ± 6 nm, approximately 10 nm larger than reported *in vitro* (Fig. 4.2H).

We next aimed to determine the COPI coat structure within the cells. We applied a reference-free subtomogram averaging workflow as previously described (Faini *et al.*, 2012) to determine the structure *ab initio*, without making use of structures previously determined *in vitro*. We selected 64 buds and vesicles with the most complete coats (judging by visual inspection). We divided them into two half-datasets and processed each half independently. Subtomograms extracted at arbitrary positions on the surfaces of vesicles were averaged to generate a smooth starting model, and the subtomograms were iteratively aligned and averaged until the references in the two separate datasets stopped changing (Fig. 4.3A) (see Materials and Methods for further details). The two final independent references contained the same approximately three-fold symmetrical structural feature in a different position and orientation. After centering the structures and applying threefold symmetry the two references looked the same and were similar to the structure of the COPI coat obtained *in vitro*. We divided all remaining buds and vesicles between the two half datasets, and performed further iterations of alignment and averaging. The resulting structures were compared by Fourier shell correlation and averaged to generate a final structure with a resolution of 20 Å (Fig. 4.3B) from 3579 subtomograms (10737 asymmetric units).

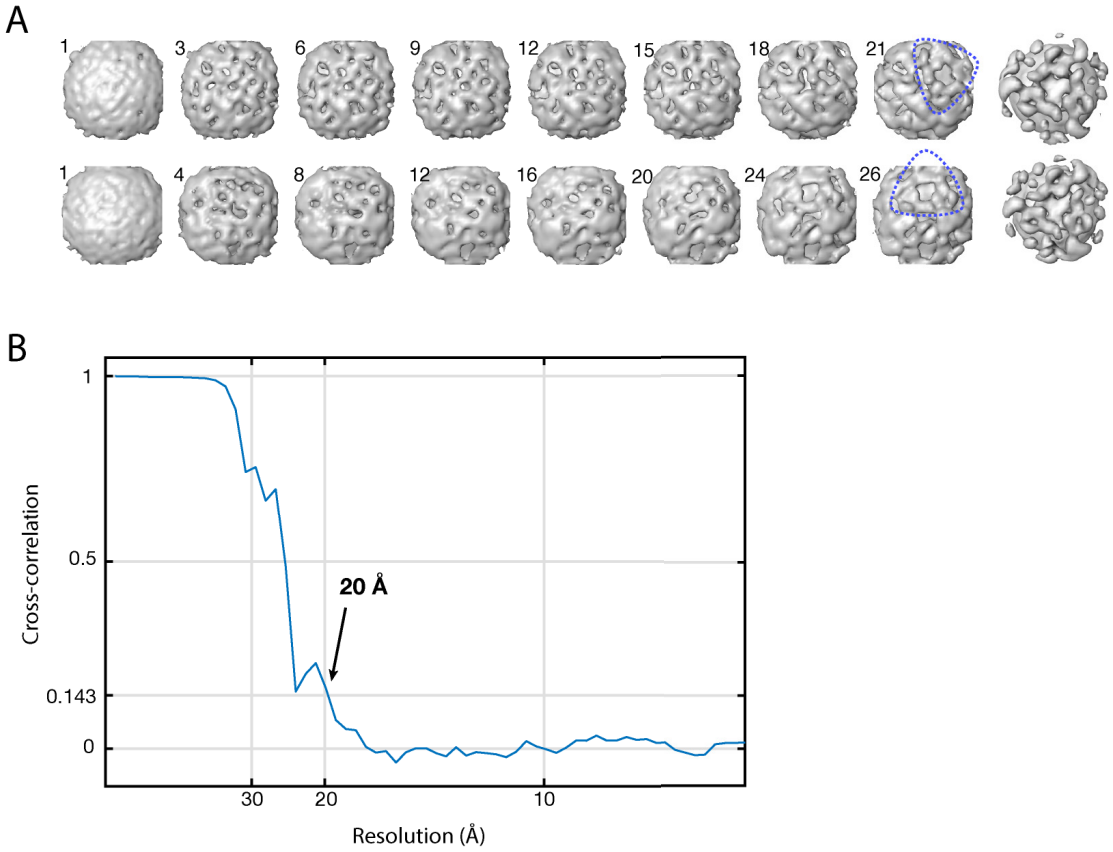

Fig. 4.3. *De novo* termination of the COPI coat structure. (A) Illustration of the convergence of reference-free reconstruction of the coat from two independent subsets of data. Iteration number is marked for each reference. After appearance of the triad structure (blue dashed line), it was centered and symmetry was applied before further iteration to give the structures at the right. (B) Fourier shell correlation curve for the final COPI structure; the FSC between two independent half-datasets is shown, marking the resolution at the 0.143 criterion.

We compared the structure of the COPI coat determined in cells with those previously determined from *in vitro* reconstituted COPI budding reactions (Fig. 4.4) (Faini *et al.*, 2012; Dodonova *et al.*, 2015). The structures are strikingly similar. The pseudoatomic model built on the basis of the *in vitro* structure fits in our in-cell structure as a rigid body (Fig. 4.4A,B,D,E). The architecture of the COPI coat described *in vitro*, in which the adaptor-like and coat-like subcomplexes do not form two layers, but rather form an intertwined, trimeric assembly, is the architecture present within cells.

A closer comparison of the *in vitro* structure and the in-cell structure reveals one clear difference. The in-cell map has an additional density positioned on the luminal side of the membrane below the N-terminal β–propeller of the β'–COP subunit (Fig. 4.4B,D,E). This position of this density, directly below the

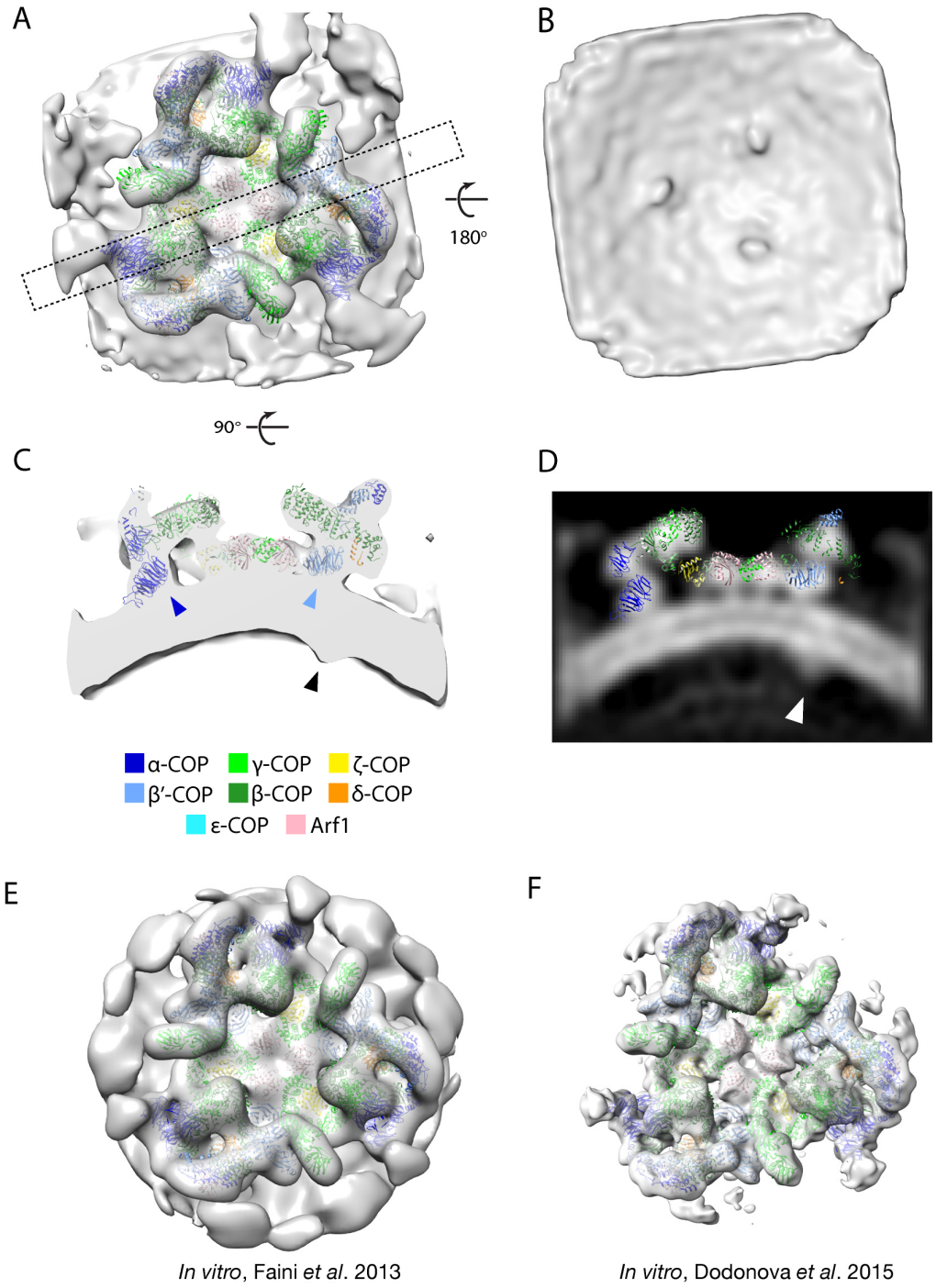

Fig. 4.4. *In situ* COPI coat structure compared to *in vitro* structures. (A) Isosurface view of the final density map (cytoplasmic side) determined within the cell, dashed rectangle shows the cut out region shown in panel C. (B) View of the same map from the luminal side. (C) Sliced isosurface view of the final map, highlighting positions of N-terminal β–propellers of α–COP (dark blue arrowhead) and β'-COP (light blue arrowhead), and additional cargo density (black arrowhead). (D) An orthographic slice through the final map with the cargo density highlighted (white arrowhead). (E) The low resolution structure of the triad previously determined from *in vitro* reconstituted vesicles, EMDB:2084 (Faini *et al.*, 2012) with PDB 5A1U fitted as a rigid body. (F) The structure of the triad previously determined from *in vitro* reconstituted vesicles, EMDB:2985 (Dodonova *et al.*, 2015) with PDB 5A1U fitted as a rigid body. Color code for the COPI subunits is given in panel C.

cargo-binding site in β'–COP, and its absence in the *in vitro* system where there is no cargo, suggests that it corresponds to the bound cargo transported by vesicles. Interestingly, we found no additional density below the homologous N-terminal β–propeller of α–COP, which also contains a cargo-binding site, suggesting that the two domains have different cargo binding specificities in the cell. This is consistent with previously reported observations using X-ray crystallography, biochemical experiments, and live cell assays, which also showed differences in the cargo binding specificity of the two β–propellers (Jackson *et al.*, 2012; Ma and Goldberg, 2013).

4.2.2 The arrangement of the COPI coat on buds and vesicles

The combination of cryo-electron tomography and subtomogram averaging also provides information on the positions and orientations of the protein complex within the cell. We visualized this information by placing a triangle in the position and orientation of each COPI triad in the analyzed vesicles and buds (Fig. 4.5A). Consistent with observations made *in vitro*, the vesicle coats are pleomorphic and the arrangement of the triads does not conform to any kind of global symmetry.

In vitro, triads were observed to contact each other in four defined patterns called linkages (Faini *et al.*, 2012; Dodonova *et al.*, 2015). Linkage III has a high inherent curvature and was previously observed to be present mainly in small vesicles (Faini *et al.*, 2012). Because the average diameter of vesicles observed in cells is larger than that observed *in vitro*, this arrangement of triads was only found in a few small vesicles. For the other three linkages we determined their structures, which showed generally good agreement with the results previously obtained *in vitro* (Fig. 4.5B-D). We previously found linkage I appears with approximately three-fold symmetric at low resolution (Faini *et al.*, 2012), but is asymmetric at higher-resolution (Dodonova *et al.*, 2015). Here we were unable to resolve the asymmetry, and the structure is similar to that previously determined at low resolution. The structure of

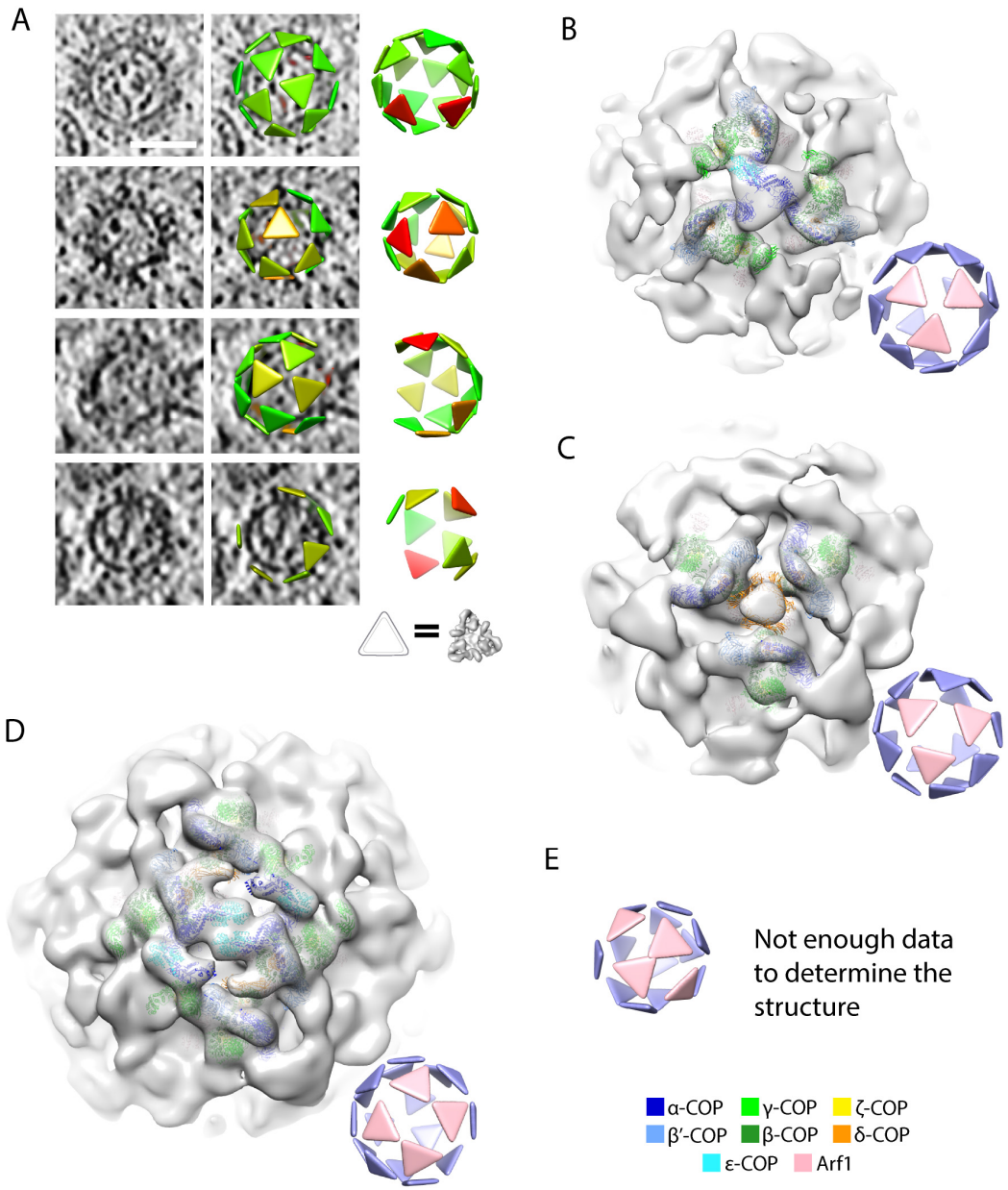

Fig. 4.5. COPI coat arrangement on vesicles and buds, and triad linkages. (A) Examples of coat arrangement on vesicles and buds, in each row: left – tomographic slice; middle – tomographic slice overlaid with triangles at the position and orientation of each triad, colored according to similarity to the final reference (green - high to red - low) (The correspondence between triangle and structure is illustrated below the panel); right – view of the triad arrangement rotated to place the budding scar towards the viewer. The vesicle in the lowest row has an incomplete coat likely to represent an intermediate stage of uncoating. (B - D) Structures of the triad linkages I,II, and IV as isosurfaces. Insets show the pattern of triads contributing to each linkage. (B) Linkage I structure, with PDB 5A1V fitted. (C) Linkage II structure, with PDB 5A1W fitted. (D) Linkage IV structure, with PDB 5A1Y fitted. (E) Linkage III, is rare, no structure was determined. Color code for the subunits is given in Fig. 4.4C. Scale bar 50 nm.

linkage II is also similar to that observed at low resolution. The density from the μ-homology domains of δ-COP located at the center of the pattern is not well resolved suggesting these domains are flexible in their position. Linkage

IV, in which interactions between triads involves ε-COP and the C-terminal domain of α–COP, is well resolved. Although functional studies suggesting that ε-COP are dispensable for COPI function (Arakel *et al.*, 2016), this observation indicates it forms a rigid, defined interaction in the coat. We observed no additional density in the pattern structures that might correspond to bound cargo apart from the one found below the β'-COP subunit.

No complete vesicles were found. Some of the vesicles are not completely contained within the lamella and in other cases, some triads may not have been successfully identified during the alignment procedure. For other vesicles, we can confirm that the coat is incomplete in the cell, either because areas of the uncoated membrane are clearly visible in the tomogram, or because the arrangement of triads would not allow the coat to be closed by the addition of further triads (Fig. 4.5A). The absence of any complete vesicle coats could reflect rapid partial uncoating after budding, or result from a budding scar, where the vesicle is never completed at the bud neck. The absence of complete vesicles in *in vitro* reconstitution reactions (Faini *et al.*, 2012), which are performed in the presence of non-hydrolysable GTP analogs, suggests that the gap in the coat represents a budding scar.

4.2.3 Budding and uncoating of COPI vesicles

We observed vesicles with varying degrees of coat completeness, as well as a large population of uncoated vesicles within the ribosome-exclusion zone surrounding the Golgi (Fig. 4.6). The luminal density of these vesicles was similar to that of COPI coated vesicles, and the diameter distribution (Fig. 4.6C, 58 ± 5 nm, n=109) was the same as that of COPI coated vesicles (Fig2H, 56 ± 6nm). These observations suggest that they are uncoated COPI vesicles. In five selected Golgi stacks we identified 36 coated vesicles and 109 vesicles without coat. We estimated the coat completeness of each vesicle in an XY slice through the center of the vesicle (Fig. 4.7). If we assume that our data represent a steady-state sample of the COPI vesicle population, the

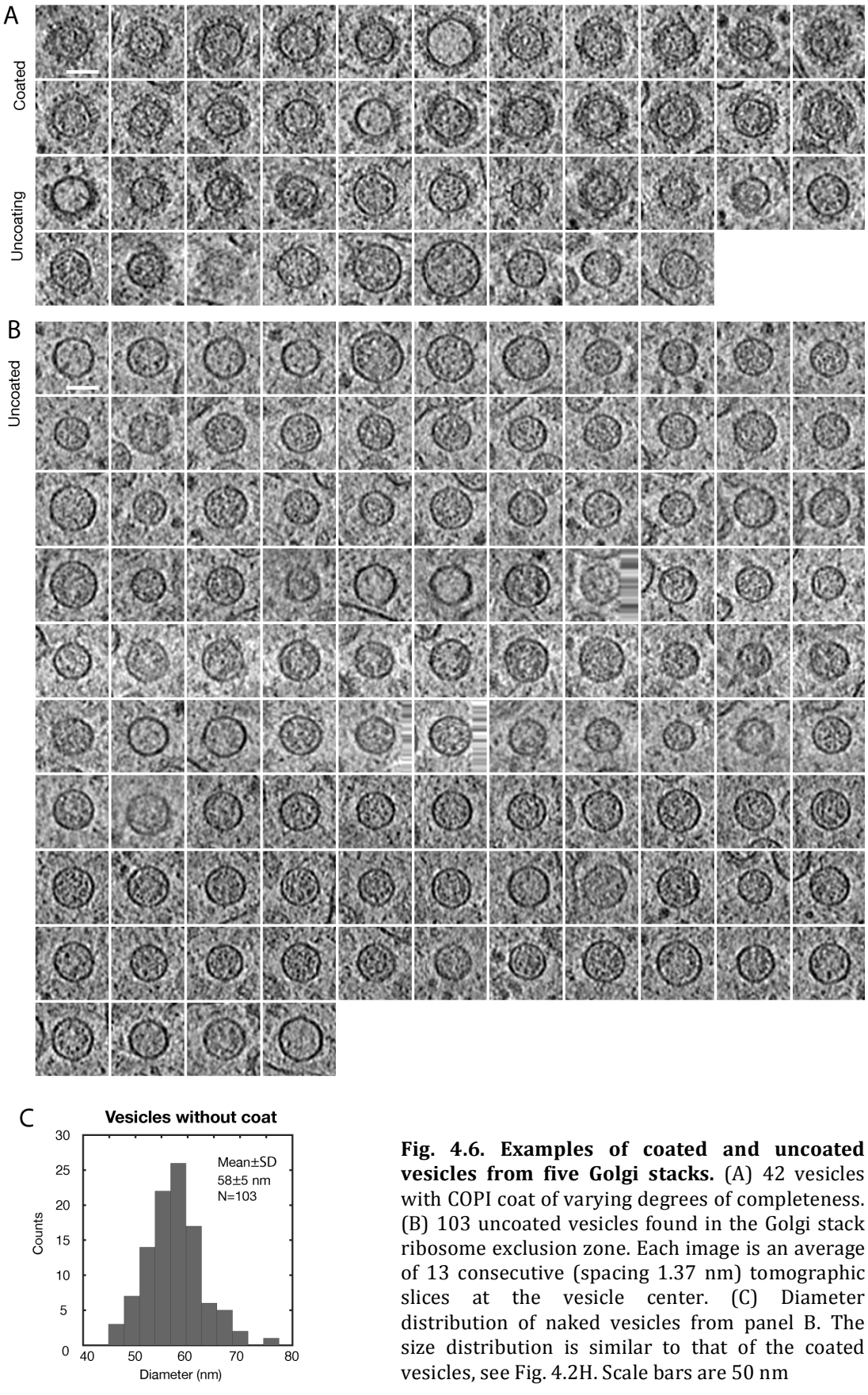

Fig. 4.6. Examples of coated and uncoated vesicles from five Golgi stacks. (A) 42 vesicles with COPI coat of varying degrees of completeness. (B) 103 uncoated vesicles found in the Golgi stack ribosome exclusion zone. Each image is an average of 13 consecutive (spacing 1.37 nm) tomographic slices at the vesicle center. (C) Diameter distribution of naked vesicles from panel B. The size distribution is similar to that of the coated vesicles, see Fig. 4.2H. Scale bars are 50 nm

distribution of coat completeness reveals the uncoating dynamics. After budding, there is a short delay, followed by rapid uncoating that is completed after approximately ⅓ of the average vesicle lifetime.

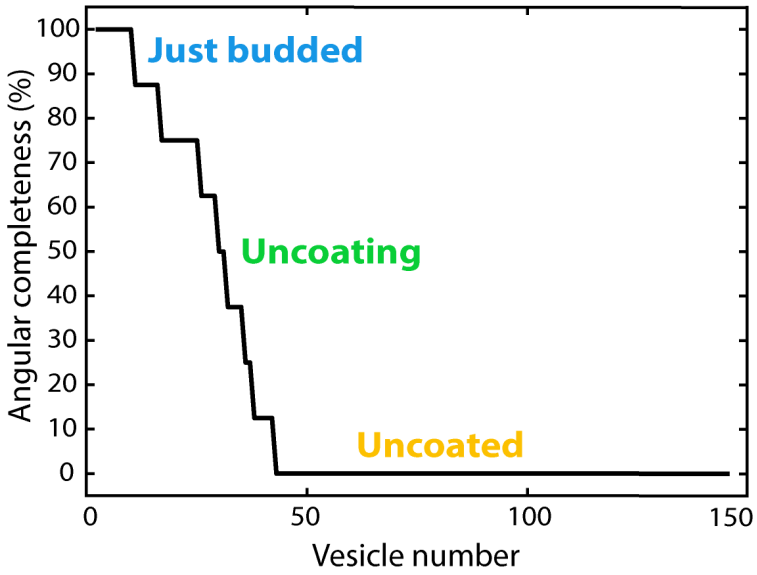

Fig. 4.7. Ranked plot of vesicle completeness as representation of uncoating process. Vesicles were sorted according to the angular completeness of the coat viewed in central slices. We note that there are no complete vesicles in the dataset, but that mostly complete vesicles may appear to be complete in a central slice. The measurements can systematically overestimate the completeness of mostly-complete vesicles, and underestimate the completeness of mostly-incomplete vesicles.

Knowing the positions of individual COPI complexes in the cell permits us to sort the complexes into spatially distinct subpopulations and generate separate structures. To assess whether there are any changes in the presence of individual COPI coat subunits during budding or initial uncoating, we calculated separate density maps for buds and vesicles, for both triads and linkages. We did not detect any substantial differences in the structures (Fig. 4.8). These observations suggest that the stoichiometry of coatomer subunits and of Arf1 are the same during assembly, and in the released vesicle. This would not be the case if GTP hydrolysis led to the loss of Arf1 from the coat either during or shortly after budding, or if there were changes in the position or presence of any coatomer subunits during or after budding.

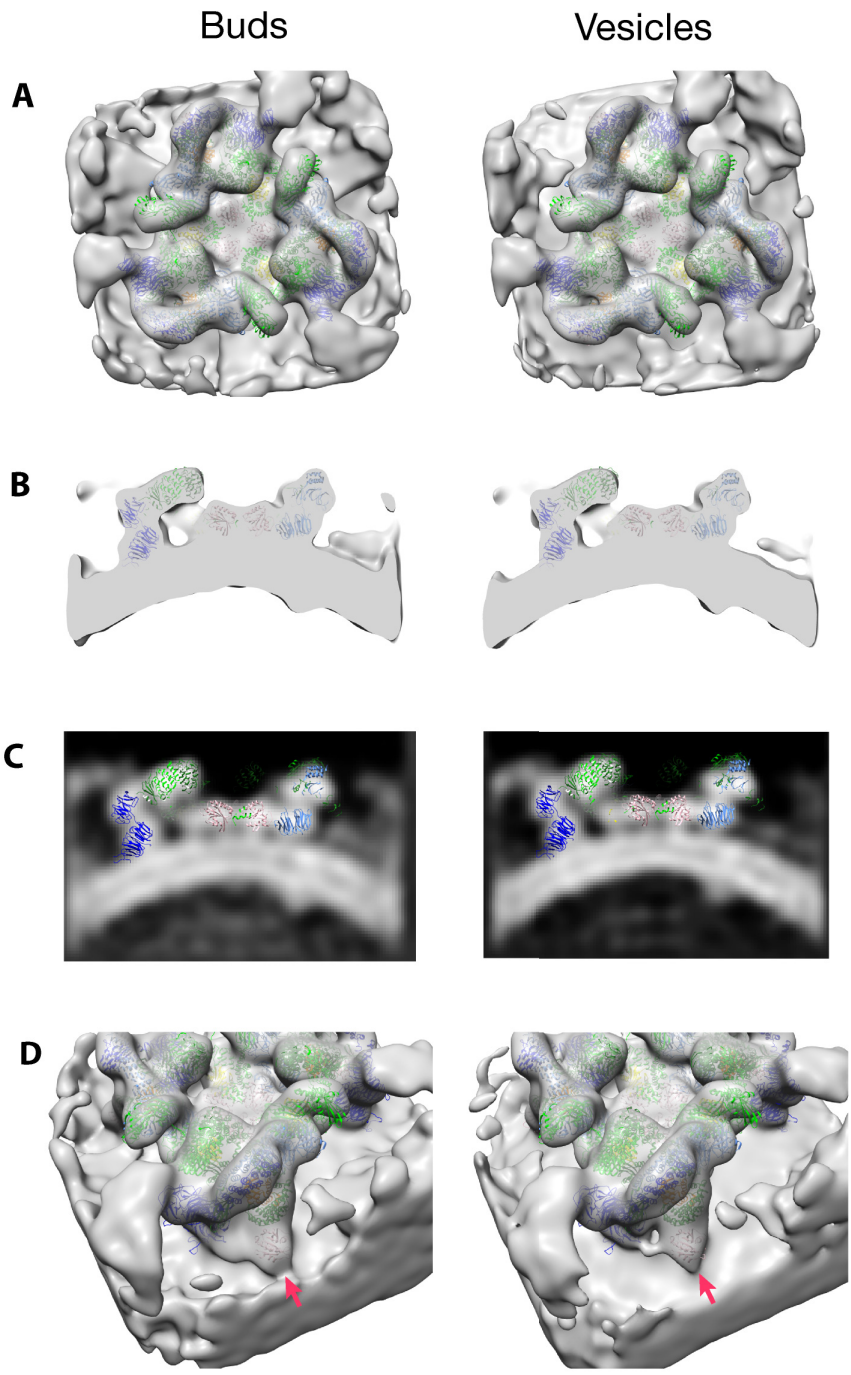

Fig. 4.8. Comparison of the structures derived from buds and from vesicles. (A) Isosurface overview of the triad viewed from the cytoplasmic side (B) Sliced isosurface view perpendicular to the membrane. (C) Orthographic slice view as in B (D) Isosurface view indicating the 'outer' Arf1 (red arrow). Color scheme: Arf1 – pink, α-COP – dark blue, β-COP – dark green, β'-COP – light blue, γ-COP – light green, δ-COP – orange, ζ-COP – yellow. Maps are shown at the same isosurface threshold, PDB 5A1U is fit as a rigid body. We note a slight difference in density between the Arf1 molecule bound to β–COP and the neighboring N-terminal β–propeller of. This is likely the result of the vesicle dataset containing a larger fraction of triads that are at the edge of the lattice. This is the position of a flexible loop region in α–COP and shows similar variability when the structures of different patterns are compared (Dodonova *et al.*, 2017)

4.2.4 Variations of vesicle and cisternae morphology in the Golgi

Most Golgi stacks in our dataset contain nine cisternae. In a typical stack, the first 3-4 cisternae are characterized by a low-density lumen and rather uniform thickness, these we refer to as the *cis* Golgi (Fig. 4.2A, Fig. 4.9A). After the third cisterna, there are one or two cisternae of intermediate morphology before the *medial* Golgi cisternae, which are characterized by increased luminal density, a thin central stacked region, and swollen cisternal edges. The *medial* Golgi usually contains 4-5 cisternae. The final cisterna in the stack, the *trans* Golgi, is always translucent and is followed by a set of rounded, translucent, TGN compartments. Intermediate transitional structures are sometimes seen between the final stacked cisterna and the TGN. COPI coated structures are found throughout the Golgi, including on the TGN. We observed changes in the appearance of COPI coated vesicles through the Golgi stack. We observed a gradual transition from lighter to darker luminal density in vesicles from *cis* to *medial* Golgi, followed by an abrupt change to a translucent lumen in *trans* Golgi vesicles. The luminal density of the buds in *cis* and *medial* Golgi was similar to that in the donor cisterna. Interestingly, while translucent buds are found on the translucent round compartments, buds on the translucent flattened *trans* cisterna had a darker lumen similar to *medial* Golgi vesicles (Fig. 4.9B-D, Fig. 4.10B). In contrast to plastic section EM, where the density of staining is heavily influenced by the properties of the molecules present, the density observed by cryo-EM reflects the density of molecules present. The increase and decrease in luminal density of COPI vesicles through the Golgi stack therefore reflects an increase and then decrease in the amount of soluble material being transported.

We also measured the diameter of buds and vesicles through the Golgi (Fig. 4.9E) and observed a gradual increase from *cis* through the medial Golgi. Translucent vesicles, primarily derived from the TGN, had a more variable diameter distribution than vesicles derived from the Golgi stacks.

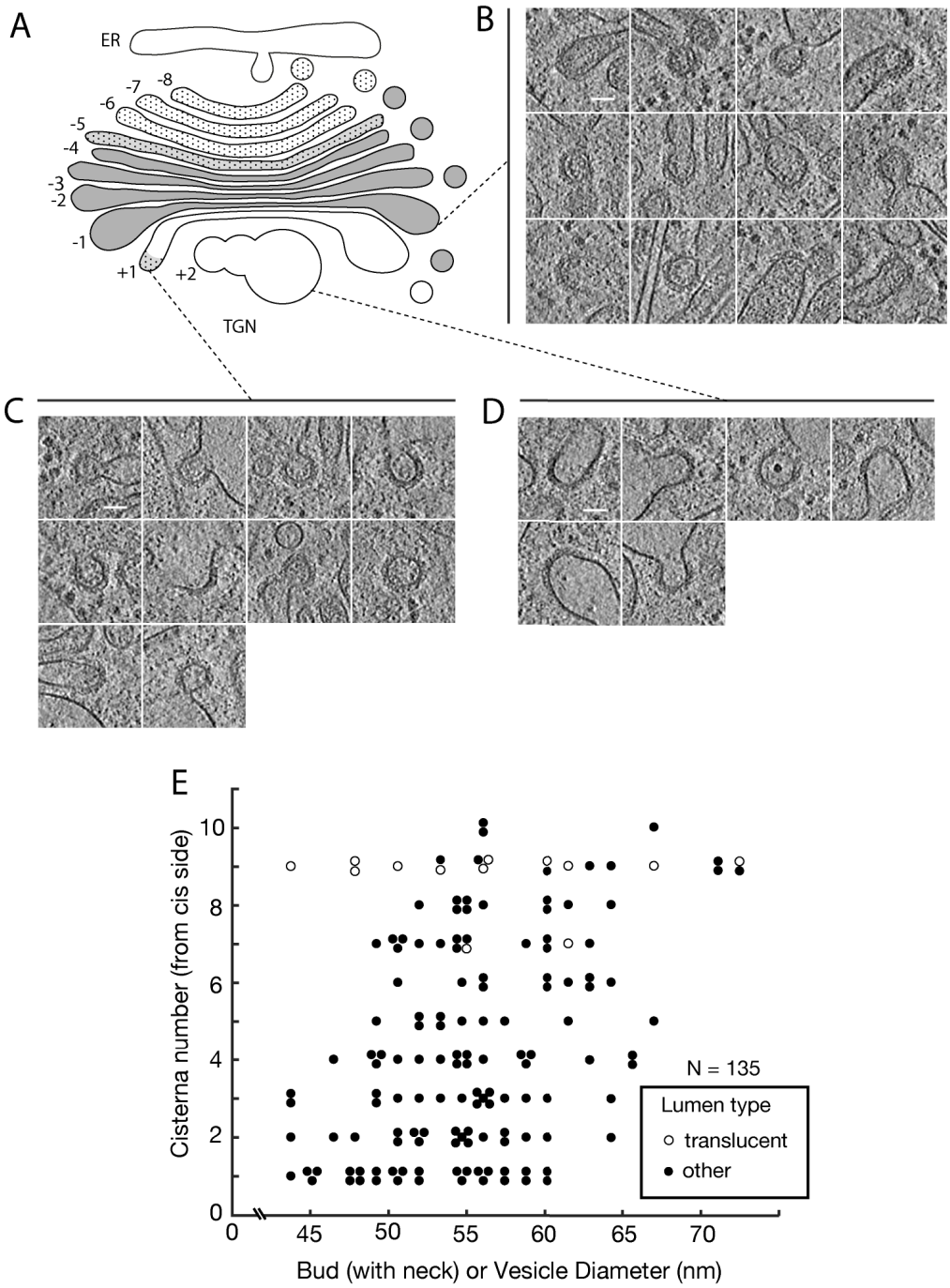

Fig. 4.9. Bud and vesicle morphology variation across the Golgi stack. (A) Schematic of the *C. reinhardtii* Golgi stack; cisternae are marked relative to the morphological transition occurring between the last medial cisterna and the trans cisterna. All cisternae before the transition have negative numbers, after – positive numbers. Examples are shown of buds from (B) the last *medial* cisterna where the buds have the same lumen density as cisternae itself; (C) the *trans* cisterna where the buds typically have a darker lumen than the translucent donor cisternae; (D) from the rounded TGN compartments where the buds have a translucent lumen similar to the donor compartment. (E) Vesicle and late bud diameter variation across the Golgi stack; the diameter of vesicles and late buds, measured to the membrane, is plotted against position in the stack based on cisternae number counting from the *cis* face. Scale bars 50 nm.

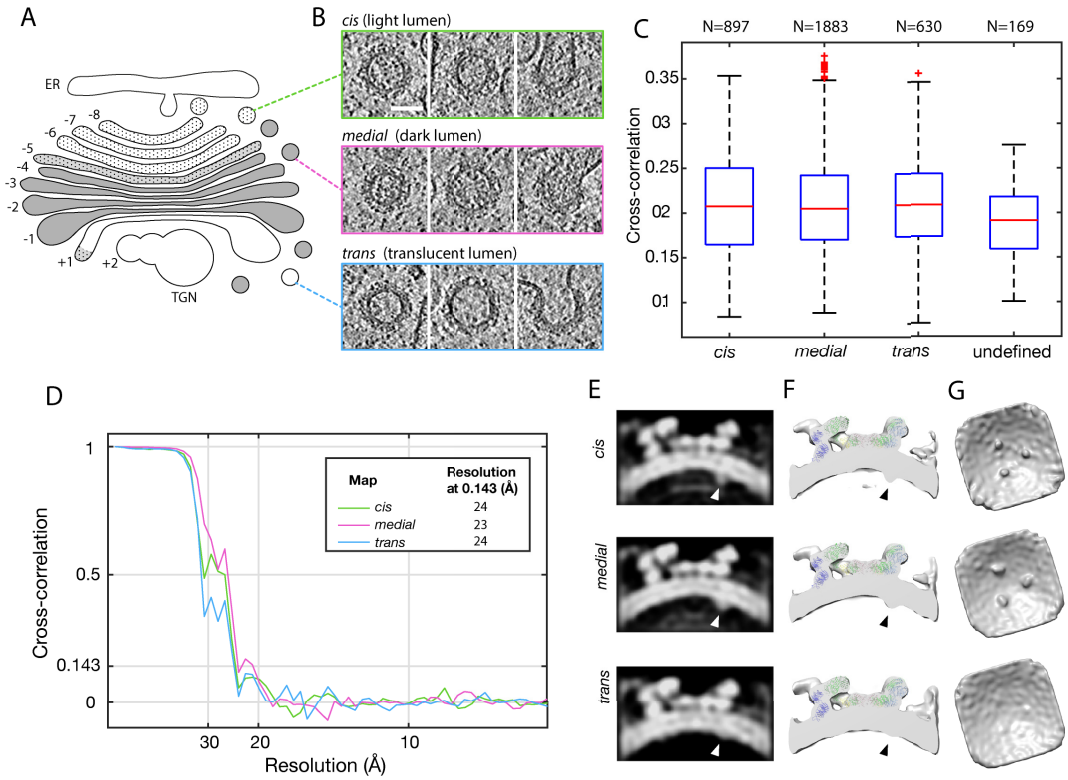

Fig. 4.10. COPI coat structure variability within the Golgi apparatus. (A) Schematic of the *C. reinhardtii* Golgi stack. See caption in Fig. 4.10. (B) Examples of buds and vesicles from different regions of the stack. (C) Cross correlation coefficients to the common reference of individual subtomograms from different Golgi regions; the boxes show 25,50, and 75 percentiles, outliers shown as red crosses are calculated with default settings of the Matlab *boxplot* function, number of subtomograms (N) for each group is given above the figure. (D) Fourier shell correlation curves for averages from different Golgi regions, resolutions are given in the legend. (E - G) Structures of the coat determined from different Golgi regions: *cis* – top row, *medial* – medium row, *trans* – bottom row. (C) Orthographic slice through the averages, cargo position is highlighted with an arrowhead. (D) Sliced isosurface views, cargo position is highlighted with an arrowhead. (E) Views of the structures from the inside of the vesicle.

4.2.5 Structural variation of the COPI coat across the Golgi

We separated vesicles and buds into three categories (*cis*, *medial*, and *trans*) based on position and morphology (Fig. 4.10A,B; see Methods for exact definitions). There was no difference in the distribution of cross-correlation values between subtomograms in each category and the average structure (Fig. 4.10C), suggesting that there are no large changes in the coat organization through the Golgi. We averaged the subtomograms in each category to determine the structure of the assembled COPI density coat separately for *cis*, *medial*, and *trans* regions, obtaining three structures at approximately 24 Å resolution (Fig. 4.10D-G). The coat structure is highly

similar in the three categories except for their luminal density, which is less prominent in the average obtained from *trans* Golgi, suggesting *trans* Golgi-derived vesicles contain less cargo, or it is less bulky.

4.2.6 Measurement of bilayer leaflet separation in COPI vesicles, and buds

Comparison of orthographic slices through the *cis, medial* and *trans* structures suggested that there are differences in membrane bilayer thickness and in membrane curvature through the Golgi. We analyzed the membrane thickness change in more detail by generating the density profile through 'flattened' references (see Methods for details) (Fig. 4.11A). Two peaks of bilayer density can be resolved. Measurement of the distance

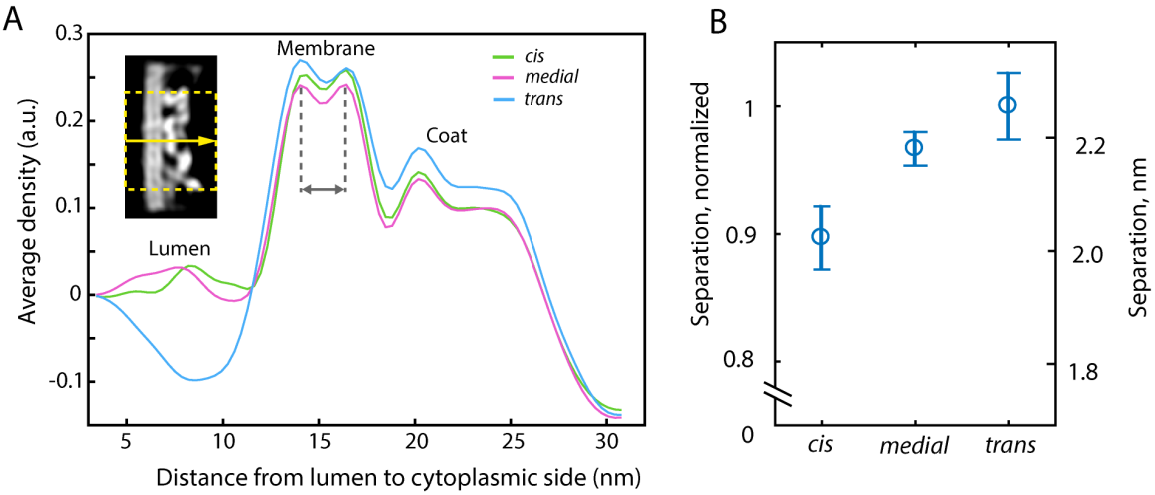

Fig. 4.11. Changes in membrane bilayer leaflet separation in COPI averages from different Golgi regions. (A) Density profile through the COPI coated membrane, measured from the structures in Fig. 4.10; inset shows an example XY orthographic slice through the flattened structure, dashed yellow rectangle and an arrow define the region averaged and the direction of the profile. (B) The bootstrapped mean bilayer leaflet separation measured for *cis*, *medial*, and *trans* averages, error bars denote bootstrapped SD (see Materials and Methods for details).

between the peaks confirmed the visual observations made on orthographic slices and showed a gradual increase of membrane thickness from *cis* to *trans* Golgi (Fig. 4.11B) (we note that absolute bilayer thickness cannot be measured from this data). This is in good agreement with the known increase in secretory pathway membranes thickness from ER towards the plasma membrane (Mitra *et al.*, 2004; Sharpe *et al.*, 2010). To further investigate the

increase in thickness, we generated averages only from buds appearing on cisterna whose position in the Golgi and morphology could be clearly defined according to the scheme depicted in Fig. 4.10A. We observed an increase in bilayer separation throughout the *medial* Golgi and on the transition to the *trans* Golgi (Fig. 4.12).

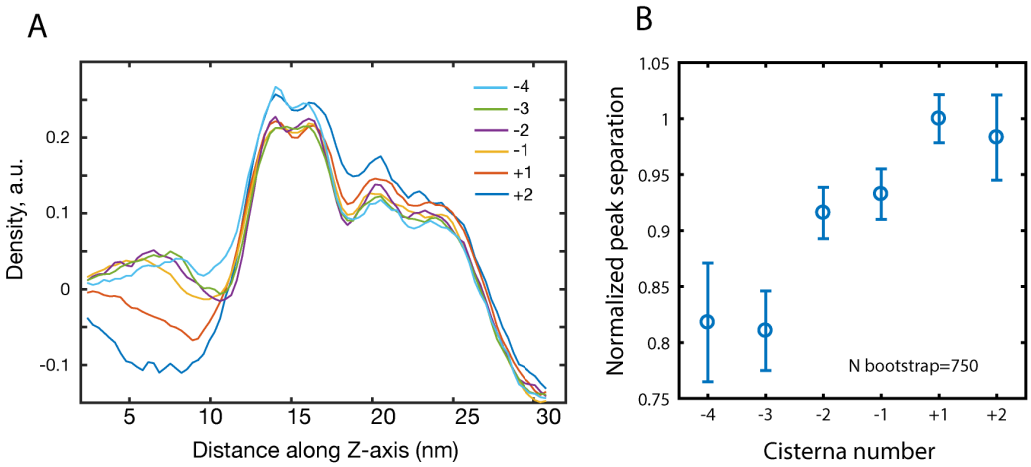

Fig. 4.12. Membrane bilayer separation change in COPI buds on cisternae with different morphologies. (A) Density profiles trough the averages derived from buds in individual *trans* and *medial* Golgi cisternae; donor cisternae morphology is marked by numbers according to Fig. 4.11A. (B) Mean bilayer thickness from the COPI coated bud density profiles shown in panel A, mean and error bars (SD) are derived using bootstrapping (see Methods).

4.2.7 Measurement of bilayer leaflet separation in uncoated Golgi membranes

We next took advantage of the fact that some Golgi stacks were imaged perpendicular to the XY plane of the sample throughout the whole tomographic volume (Fig. 4.13A). In these tomograms, the bilayers could be directly observed (Fig. 4.13B). We took individual slices from the reconstructed tomograms, and aligned and averaged 2D images of the bilayer for each of the stacked cisternae (FIG. 4.13B,C). The averaged profiles showed that the membrane thickness increases in the *medial* Golgi and the *trans* cisterna has the thickest membrane (Fig. 4.13D-H).

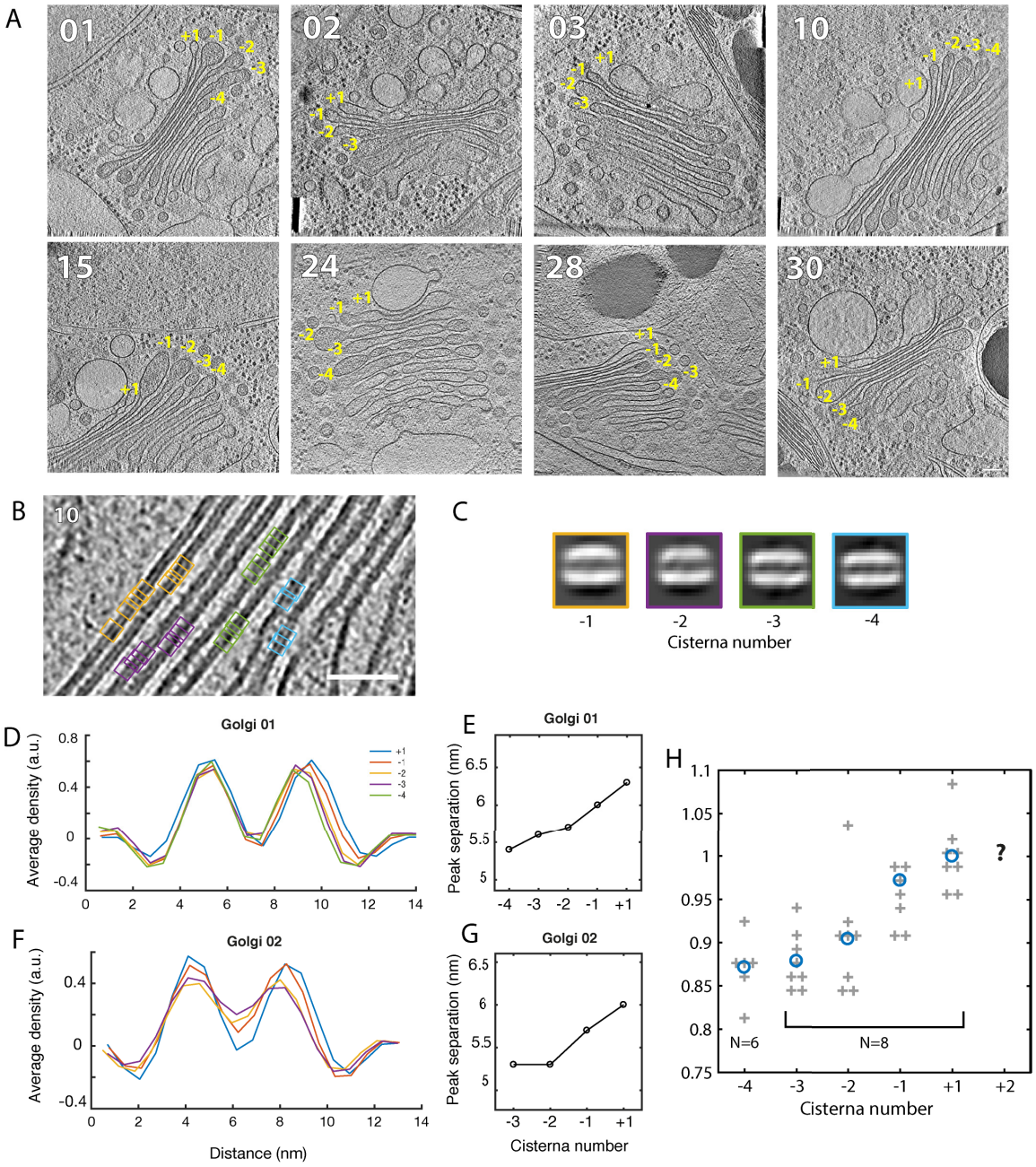

Fig. 4.13. Membrane bilayer separation of uncoated Golgi membranes. (A) Tomographic slices through 8 Golgi stacks with membranes of *trans* and *medial* Golgi positioned perpendicular to the XY plane; cisternae morphology is classified according to Fig. 4.10A (B) Slice through Golgi 10 demonstrating bilayers visible by eye; Example of particle boxing is shown by colored squares; color corresponds to cisterna number assigned by morphology, see panel A. (C) Averages derived for individual cisternae of Golgi 10. (D,F) Density profiles through cisterna bilayer averages in Golgi 01 (D), and Golgi 02 (F). (E,G) Distance between the density peaks for each cisterna average for Golgi 01 (E), and Golgi 02 (F) measured from plots on panels (D,F). (H) Normalized distance between the peaks for all cisternae of all measured Golgi stacks. Values are divided by the mean value for cisterna +1. Measurements for cisterna +2 (round TGN compartments) could not be obtained because of small amount of membranes strictly perpendicular to the XY plane. Scale bar 100 nm in A and 50 nm in B.

4.3 Discussion

4.3.1 *In vitro* reconstitution of COPI budding mimics the structure determined in cell

The structure of coatomer determined *ab initio* within the *Chlamydomonas* cell, as well as the relative arrangements of triads on vesicles and buds, are the same as those determined in vitro at similar resolutions using coatomer from mouse (Faini *et al.*, 2012; Dodonova *et al.*, 2015). The higher-order structure of coatomer is therefore highly conserved across species. Furthermore, the *in vitro* reconstituted budding reaction generates vesicles that faithfully mimics those found within the cell, giving confidence in the interpretation of higher-resolution structural details revealed by *in vitro* studies.

4.3.2 The morphology of COPI coated vesicles changes through the stack, but the structure does not

We observed changes in luminal density, cisternae morphology, and membrane thickness, between different cisternae in the Golgi stack. The increasing membrane thickness towards the *trans* Golgi is consistent with the increased sphingomyelin (SM) and cholesterol content towards the plasma membrane and has been suggested to play a role in transmembrane protein sorting (van Meer *et al.*, 2008; Sharpe *et al.*, 2010). Luminal density and membrane thickness changes in COPI vesicles and buds generally followed the changes occurring in the donor cisternae throughout the Golgi with a notable exception: buds from the last translucent cisterna have a darker lumen than the donor compartment. We consider it likely that the change in vesicle size reflects the changes in the morphology of the cisternae rims (and therefore changes in the curvature of the donor membrane) through the Golgi. Membrane lipid composition and cargo density may also modulate vesicle curvature.

Our observation of specifically bound cargo under the cargo-binding site in β'–COP beta propellers, as well as the dark lumen of buds on the trans-cisterna, confirm biochemical studies showing that the composition of the COPI vesicle is not identical to that of its donor membrane (Brügger *et al.*, 2000). Nevertheless, the majority of variability in vesicle morphology that we observe can be explained by changes in donor compartment morphology. These changes are reflected in differences in luminal density, membrane thickness, and size, for COPI coated vesicles at different positions throughout the Golgi, based on which vesicles have previously been grouped into different subtypes (Donohoe *et al.*, 2007). We found, however, that the COPI coat structure is the same in all of these vesicles. We find no indication of structurally distinct subclasses of COPI buds and vesicles.

4.3.3 The assembly and disassembly cycle of the COPI coated vesicle

Our analysis of bud and vesicle completeness showed that complete vesicles are never formed. After budding, the coat disassembles, and naked vesicles remain in the cytoplasm for an extended period before fusing with their target membrane. We cannot exclude that individual coatomer molecules remain associated with the naked vesicles. Comparison of the structures derived from buds and vesicles suggest that Arf1 and coatomer disassemble simultaneously. These observations confirm and refine the generally accepted model of COPI vesicle life cycle. COPI is recruited by activated Arf1 leading to membrane bending and bud formation. After scission, a small area (the budding scar) remains uncoated. Arf1 is a structural component of the coat throughout this process. Vesicles remain coated for a short time after budding before GTP hydrolysis leads to disassembly of the coat. Later, uncoated vesicles fuse with their target membrane. At any one time, there are more uncoated vesicles present than coated vesicles.

4.3.4 The power of *in situ* structural biology

FIB-milling allows the cell interior to be studied in a close to native state otherwise inaccessible to TEM (Rigort *et al.*, 2012b; Harapin *et al.*, 2015; Schaffer *et al.*, 2016). Together with improved electron detectors (McMullan *et al.*, 2014), it helps to generate high-quality cryo-electron tomograms that can be analyzed by subtomogram averaging. Here we have demonstrated that this allows the determination of the structure of the COPI coat, can be directly determined, *ab initio*, within the cell. Because information on the spatial distribution of molecules in maintained, it was also possible to separately analyze COPI complexes on buds and vesicles as well as to address the coat structure in different regions of the Golgi. We are optimistic that increased use of these technologies will have a major impact on our understanding of cellular mechanisms.

4.4 Materials and Methods

4.4.1 Sample preparation and electron tomography

Cell culture, sample preparation, FIB milling and cryo-electron tomography were performed by B.Engel and coworkers in Max Planck Institute of Biochemistry. The dataset analyzed here consisted of 29 tomograms, including 9 described in previously published studies of the Golgi intracisternal arrays (Engel *et al.*, 2015). Cell culture and sample preparation was performed as previously described (Engel *et al.*, 2015). The *Clamydomonas reinhardtii* strain *mat3-4* characterized by smaller cell size was grown with constant light and normal atmosphere aeration in Tris-acetate-phosphate (TAP) medium. Plunge-freezing and cryo-focused ion beam milling was performed as previously described (Schaffer *et al.*, 2015). Cells were applied on carbon-coated 200-mesh copper grids (Quantifoil Micro Tools), which were plunged into liquid ethane-propane mixture using Vitrobot Mark 4 (FEI). After freezing grids were mounted into modified Autogrids (FEI) and loaded either into Scios FIB/SEM microscope (FEI) or in

Quanta 3D FEG FIB/SEM microscope (FEI). Samples were coated with thin layer of organometallic platinum using the in situ gas injection system (GIS, FEI). Thin lamellas were milled using the Ga^+ beam at 30 kV and shallow angle of 8°-12°. Tomograms were collected at 300 kV using Titan Krios (FEI) controlled by SerialEM software (Mastronarde, 2005), equipped with a postcolumn energy filter (968 Quantum, Gatan) and K2 Summit direct electron detector (Gatan). Most of the tilt series were collected in the angular range of -60 to +60 degrees using a 2 degree increment, bi-directional tilt scheme, electron dose was kept under 100 $e^-/Å^2$, pixel size was 3.42 Å, and defocus ranged from -4 to -6 um.

4.4.2 Subtomogram averaging

Subtomogram averaging was performed essentially as described previously, in a reference-free manner on two independent half-datasets (Faini *et al.*, 2012; Dodonova *et al.*, 2015). Cumulative electron dose-dependent low-pass filters were applied to the tilt series before processing. Exposure filters were calculated as previously determined assuming uniformly distributed total dose of $60e^-/Å^2$ (Grant and Grigorieff, 2015). CTF correction of individual tilt images was performed using *ctfphaseflip* implemented in IMOD (Xiong *et al.*, 2009). Tilt series were aligned in IMOD using patch-tracking and reconstructed using weighted backprojection (Kremer *et al.*, 1996). Tilt series alignment was performed by B. Engel and coworkers. All other processing steps described here were performed by the author of this thesis.

Tomograms were visualized in Amira software (FEI). We localized 267 COPI vesicles and buds, measured their diameters at the level of membrane and determined central coordinates. Subtomogram alignment and averaging was performed using Matlab (Mathworks) scripts derived from the TOM (Nickell *et al.*, 2005) and Av3 (Förster *et al.*, 2005) toolboxes essentially as described (Dodonova *et al.*, 2015). Vesicle and bud diameters, and coordinates were used to define starting positions and orientations of subtomograms. The positions were placed as evenly distributed points (spacing 10 nm) on the

surface of the sphere defined by vesicle center and diameter. Initial psi and theta angles (define out of plane rotation) were assigned as normal to the sphere surface. Phi angles defining in-plane rotation were assigned randomly.

To generate the initial reference we selected 64 vesicles and late buds, which were completely embedded in ice, had close to average diameter, and extensive coat. This set was split in two independent halves that were processed separately. Subtomograms were extracted from binned volumes with pixel size 13.68 Å. Initial smooth averages were generated based on the assigned Euler angles and subtomograms were aligned to them iteratively. After convergence the approximately three-fold symmetrical feature identical between two independent references was brought to the center of both references and additional alignments were performed with three-fold symmetry applied. References were then rotated to the same orientation and used as the starting references for alignment of the full dataset.

The remaining vesicles and buds were then divided between the two half datasets. Subtomograms were extracted as described above and aligned to the starting references. After alignment we removed subtomograms with low cross-correlation coefficient to the reference. Overlapping subtomograms were removed based on the distance threshold of 17.7 nm (13 pixels). The final datasets had 1713 and 1866 subtomograms (5139 and 5598 asymmetric units). The structures were further refined by processing subtomograms extracted from binned (pixel size 6.84 Å) and unbinned (pixel size 3.42 Å) volumes. Prior to the resolution measurement each reference was masked with soft-edged cylindrical mask excluding the membrane. Resolution was measured using mask-corrected phase-randomized Fourier shell correlation (FSC) (Chen *et al.*, 2013). The final density map was obtained by averaging the structures from the two half-datasets. The final structures was low-pass filter to the determined resolution, reweighted by division by the sum of its CTFs, and sharpened with a B-factor of -2000 (Rosenthal and Henderson, 2003). Map visualization and PDB fitting were performed using Chimera software (Pettersen *et al.*, 2004). The pseudoatomic model 5A1U from the *in vitro* study was fit as rigid body in Chimera.

4.4.3 Lattice map and linkage structure analysis

Triad positions and orientations were visualized using a custom chimera plugin. Identification of linkage positions and structure determination was performed as described (Faini *et al.*, 2012). Triad positions were visualized and example sets of triads representing each linkage were picked. These sets were used to calculate the relative rotations and translations between the triads in a linkage and search the dataset for positions matching these patterns. Subtomograms were extracted from binned volumes (pixel size 6.84 Å), at these positions and divided in two half-sets. Euler angles were assigned to each pattern. We randomized the third Euler angle and ran an in-plane iterative rotational alignment on the first half dataset, regenerating the linkage structure. This reference was low-pass filtered to 55 Å and used as a starting reference to align the second half dataset. Resolution was measured as described above and was determined to be 33 Å, the same for all linkages. PDB pseudoatomic models 5A1V, 5A1W, 5A1Y from the *in vitro* study were used for fitting.

4.4.4 Measurement of vesicle coat completeness

To measure the distribution of vesicle coat completeness, we identified 42 coated vesicles and 103 uncoated vesicles in five selected Golgi stacks (Fig. 4.6). 13 tomographic slices around the vesicle center were averaged, and the resulting image was overlaid with a mask dividing it into eight sectors. The number of sectors containing coated membrane was recorded for each vesicle and used to calculate the angular completeness. While there are no complete vesicles in the dataset, mostly-complete vesicles may appear to be complete in a central slice. Thus, the measurements can systematically overestimate the completeness of mostly-complete vesicles, and underestimate the completeness of mostly-incomplete vesicles. The ratio of vesicles with coat to uncoated vesicles was ~1:2. We estimated the lifetime of coated vesicles as 1/3 of the total vesicle lifetime.

4.4.5 Morphological annotation and structure variation analysis

The dataset of 267 vesicles and buds was visually annotated. Each vesicle or bud was assessed for budding stage (early bud, late bud with neck, vesicle), luminal density and position within the Golgi stack. Cisternal morphology was defined according to the scheme shown in Fig. 4.9A. Only vesicles and buds whose positions could be confidently defined were used for generating separate averages from the *cis*, *medial*, and *trans* regions. For structural analysis across the Golgi stack, we aimed to separate vesicles and buds into three groups that had maximal morphological and positional variation. For the '*cis*' average, we included all buds on the cisternae with *cis* morphology and position (usually the first four cisternae from *cis* side, which had uniform thickness and light luminal density) and all vesicles residing near the first two cisternae of the Golgi stack and between the Golgi and ER. For the '*medial*' average, we took all buds from cisternae with *medial* morphology (narrow region at the cisterna center, swollen periphery, dense lumen) and all vesicles not assigned to the '*cis*' and '*trans*' classes. Most of the buds on the last *trans* cisterna were included in the '*medial*' average due to their dark luminal density (Fig. 4.9C). For the '*trans*' average, we took vesicles and buds with a characteristic translucent lumen. These selected buds mostly emanated from TGN compartments. '*Trans*' vesicles resided near the *trans* Golgi and TGN, and were easily distinguished from '*medial*' vesicles by lumen density. To measure membrane thickness in buds from individual cisternae, we defined the cisterna number relative to the first compartment with a translucent lumen, as diagrammed in Fig. 4.9A. This compartment, which normally corresponded to the *trans* cisterna but occasionally the TGN (Fig. 4.13A), was numbered +1. Preceding cisterna were labeled according to their position as -1, -2, -3, -4, -5. Translucent compartments that followed +1, corresponding to swollen and heterogeneously shaped TGN, were labeled +2.

4.4.6 Measurement of membrane thickness in vesicles and buds

Comparison of orthographic slices through the *cis, medial* and *trans* structures suggested that there are differences in membrane bilayer thickness and curvature through the Golgi. We analyzed the membrane thickness change in more detail by generating a density profile through 'straightened' references. The membrane thickness was measured from straightened subtomogram averages of the vesicle/bud groups defined above: *cis*, *medial*, and *trans* (Fig. 4.10E), as well as averages of buds from individual cisternae of the *medial* and *trans* Golgi (Fig. 4.9A-D, Fig. 4.12A). The averages were low-pass filtered to 25 Å and sharpened with a B-factor of -2000. Volumes were straightened using radial orthographic projection as previously described (de Marco *et al.*, 2010), and the average density profile was determined along the perpendicular vector to the straightened reference's membrane (Fig. 4.4F, top left inset). The distance between the two peaks of the membrane bilayer was measured. For each subset, we then applied a bootstrap approach in which we repeated the procedure described above (from averaging to measurement) 750 times on sets of subtomograms equal in size to the original subset but randomly sampled from it with replacements. From these 750 profiles we determined the mean and standard deviation of the membrane thickness. Data analysis was performed in Matlab (Mathworks).

4.4.7 Measurement of membrane thickness in Golgi cisternae

To measure the membrane thickness in stacked, non-coated Golgi cisternae, we selected eight Golgi stacks in which the bilayers could be clearly observed and the cisternae were perpendicular to the imaging plane throughout the tomographic volume (Fig. 4.13A). We extracted XY slices from the tomogram, then extracted 20x20 boxes along a bilayer, which were aligned and averaged using elements of the RELION helical reconstruction workflow (He and Scheres, 2016) to obtain a well-resolved 2D bilayer average (Fig. 4.13B,C) for each cisterna. The number of particles for each average ranged from 100 to

300. The membrane density profile along the perpendicular vector to the bilayer was extracted using Fiji (Schindelin *et al.*, 2012) and the peak-peak distance was measured (Fig. 4.13D-G). The membrane profile is modulated by a number of effects that are difficult to assess including the contrast transfer function of the microscope, the charge gradient across the bilayer, the presence or absence of associated proteins and the exact orientation of bilayer relative to the beam (in case of 2D average). For this reason, while measurements can be compared within one experiment, it is important to note that the peak-peak distance does not correspond to the absolute bilayer thickness and cannot be compared to measurements performed in different ways such as those from the subtomogram averages.

Chapter 5. Conclusions and perspectives

Historically, electron microscopy was one of the key techniques revealing compartmentalization and complexity of the eukaryotic cells. The rapid progress in the method and instrumentation development makes EM a multipurpose and powerful tool to address various questions of membrane biology in the modern age. During my Ph.D., I applied different electron microscopy methods to the studies of the endocytic-secretory pathway from structural to morphological level. In Chapter 2, I described a method to increase throughput of 2D EM of plastic embedded yeast and studied MVB morphology in different strains. A more detailed MVB morphology analysis is described in Chapter 3, which was performed using CLEM and tomography. Finally, using *in situ* cryo-ET and subtomogram averaging I determined the structure of the COPI coat and studied its variability within the cells of *Chlamydomonas reinhardtii*.

5.1 Increasing throughput of plastic EM

I developed a method to increase the sample-wise throughput of the conventional 2D electron microscopy of plastic embedded budding yeast cells. This method relies on fluorescent barcoding of individual cell populations pooled and processed together to reduce time spent on the sample preparation. The developed protocol allows combination up to 31 yeast strains or experimental conditions in one sample. An additional

advantage of this approach is that inclusion of all the cells in one sample eliminates the variability of morphology arising between different samples during fixation and embedding. Control cell strains can be included in the same sample. I demonstrated the application of the barcoding approach to parallelize a conventional CLEM experiment with fluorescent protein fusions and to compare general morphology and morphology of the MVBs in different yeast strains and deletion mutants.

The number of applications for the fluorescent barcoding method can be further extended. It can be used to parallelize a wide range of different experiments such as drug screenings, experiments with inducible systems when a drug is added to activate or stop gene expression or degrade the gene product. With additional throughput, some mutation screenings normally omitted to save time, could be preformed. For example, a systematic set of deletions and amino acid substitutions can be generated within one gene and effects of these deletions on the organelle morphology can be tested. Parallelization together with systematic gene labeling can be used for immuno-EM experiments. The feasibility of such an approach was tested and demonstrated by our collaborators in the Maya Schuldiner laboratory (Weizmann Institute of Science). Using one genetically engineered label and many strains within one sample can simplify the quantification of immunolabeling data.

The fluorescent barcoding protocol application can be widened with further technological developments. Together with our collaborators (M. Schuldiner laboratory) we are working on finalizing easy-to use software tools, so that barcoding can be used by cell biologists without experience in image processing. The barcoding approach we used for yeast can be extended to other organelles. In a series of preliminary experiments we showed that bacterial cells can be labeled in a similar way and development of such a strategy for mammalian cells seems feasible because of the wide range of fluorescent probes available for this system. Additional imaging strategies, like multi-step analysis at different magnifications can be developed to make experiments more effective and not limited by the electron microscope

imaging speed. Finally, a large amount of data generated by the electron microscope can be analyzed and mined using the recent developments in image processing.

5.2 MVB morphology by CLEM tomography

As a part of collaborative project with the David Teis laboratory (Innsbruck Medical University) I performed correlative microscopy and electron tomography analysis of Vps4-positive multivesicular bodies in budding yeast cells. My analysis complemented the live imaging data from the Teis laboratory by confirming that Vps4 tagged with fluorescent protein performs its functions normally and that MVBs in yeast cells usually form one intraluminal vesicle at one time. Additionally to that I analyzed the morphology of the population of MVBs and proposed how MVB maturation can occur from the morphological perspective. I developed a simple geometrical model that can help to describe this process more accurately.

Further, more detailed tomographic analysis can help to validate the model I proposed, and help to elucidate the role of ILV formation and endosome fusion/fission processes in the molecular mechanism of transition from early to late endosomes. Electron tomography is a unique method providing precise information on shape, surface areas and volume of cellular compartments. Such quantitative information can be combined with more advanced mathematical modeling to describe the relationship between shape and function which remains poorly understood for the majority of organelles.

5.3 *In situ* structural analysis of the COPI coat

In final part of this thesis I described the structure of the COPI coat determined *in situ* in collaboration with Benjamin Engel (Max Planck Institute of Biochemistry). Applying a reference-free subtomogram averaging approach I generated the structure of the COPI complex *de novo* validating

earlier *in vitro* studies. Using the information about the position of individual COPI complexes, I addressed the variability of the complex and found it to be very stable during the uncoating process and in different Golgi region, while membrane and cargo composition within the COPI-coated vesicles and buds was variable. Many questions about COPI vesicle biogenesis and function remain unanswered and can be further addressed by *in vitro* and *in situ* subtomogram averaging. These questions include: What is the functional difference between the Arf1 GTPase molecules bound in different parts of the coat? Which parts of the coat determine its polymerization and how does it occur? What is the role of different cofactors in this process?

The *in situ* structural biology approach became possible with the recent developments in the instrumentation and bears a big potential in the future as the hardware and software rapidly develops. The majority of structural data is currently acquired from *in vitro* reconstituted assemblies. Many macromolecular complexes and reactions are difficult to reconstitute *in vitro* because they tend to loose physiologically relevant cofactors and conformations. In my thesis I showed that *in vitro* data can be not only successfully validated *in situ* but also new structures can be discovered *in situ* without any previous knowledge. Cryogenic electron tomograms of the native cellular environment contain a lot of information that can be extracted using computational methods. The use of the phase plate technology can provide dramatic enhancement of the tomographic data contrast, making detection and averaging of macromolecular complexes easier. New methods for mining and classification of such data will allow discovery of new macromolecular complexes, confirmations and cofactors which were previously inaccessible for in vitro studies. Structural details visualized in cells can be further studied and analyzed in the context of the native crowded environment so that cell biology can be bridged with structural techniques directly.

5.4 The future of correlative microscopy

Correlative light and electron microscopy aims to combine the two imaging modalities and complement their strong sides. In this thesis I used correlative microscopy of plastic embedded yeast to characterize the morphology of the maturing endosomes. Light microscopy imaging of the plastic EM samples allowed increasing the throughput of the screening experiment (Chapter 2), and targeting the tomographic acquisition to the organelles of interest (Chapter 3). I also used *in situ* structural biology approach to analyze the structure of the COPI coated vesicles in the context of vitrified cells at cryogenic conditions. Structural biology approach can also benefit from the application of correlative techniques.

Cryogenic light microscopy required for correlative workflows at cryo-conditions is rapidly developing (reviewed in Chapter 1). A wide array of setups have been developed and some of them are available commercially. Some efforts were made to increase the resolution of cryogenic light microscopy by applying super-resolution imaging techniques. Further development in this area will require more detailed study of the photophysical properties of the fluorophores at cryogenic conditions and improvement in the instrumentation to reduce sample drift and heating.

Tomographic analysis of lamella produced by the cryo-FIB technique is still only partially compatible with correlative microscopy: light microscopy can be used to approximately target the FIB-milling to include the organelle of interest in the lamella, but more accurate correlations are not possible.

The vitreous sectioning technique is fully compatible with light microscopy which can be used both for targeting of the EM acquisition to rare organelles and structures, and for high-precision correlations using fluorescent fiducials. The level of native structure preservation in vitreous sections is lower than in FIB-lamella due to the sectioning artifacts, and the quality of tomographic reconstruction is lower leading to the poorer resolution. This disadvantages are compensated by a much larger areas available on vitreous sections for EM imaging and correlative analysis.

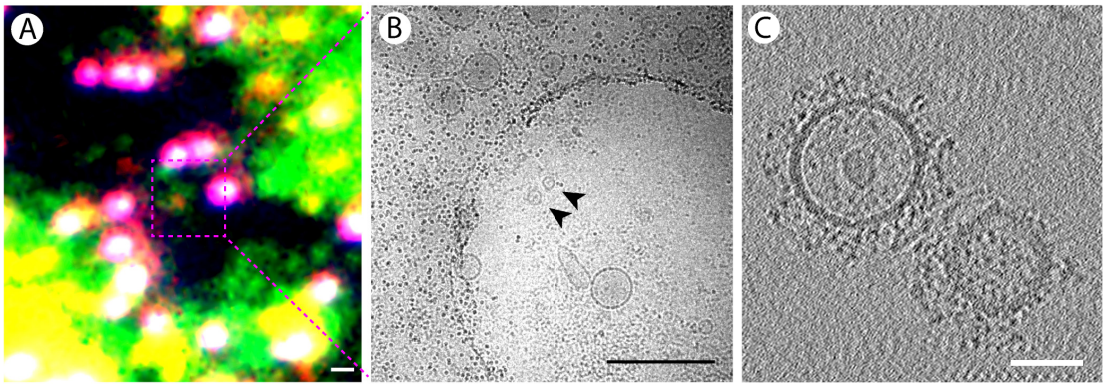

Fig. 5.1. Application of cryo-CLEM to identify endocytic vesicles in a crude preparation of cellular vesicles. (A) Cryogenic fluorescence microscopy of plunge frozen crude vesicular fraction from the cells expressing clathrin light chain labeled with EGFP and AP-2 labeled with TagRFP; Clathrin signal is in green, AP-2 signal is in red, fiducials used for correlation are fluorescent in all channels and appear in white and magenta; the region shown in panel B is highlighted by the dashed rectangle. (B) Medium magnification EM map region correlation to the light micrograph with the spot-like clathrin/AP-2 signal region highlighted in panel A; two vesicles imaged by high-resolution tomography are shown with arrowheads. (C) Tomographic slice of the two clathrin vesicles localized using CLEM. Scale bars are 1 μm in A and B, and 50 nm in C.

An interesting intermediate approach between *in vitro* reconstitution systems and *in situ* studies of vitrified cells is to use correlative microscopy to analyze crude cell fractions. This can provide higher resolution and throughput than *in situ* techniques but give access to the organelles and macromolecular complexes that are difficult to reconstitute *in vitro*. I explored this approach in a series of experiments not included in this thesis and performed together with Ori Avinoam (Fig. 5.1). Using cryo-CLEM we managed to identify clathrin coated vesicles containing an endocytic adaptor protein AP-2 in a crude vesicle preparation and acquire high-quality electron tomographic data. This approach is a potential way to validate data obtained *in vitro* and to perform additional biochemical experiments on more native structures. Cryo-CLEM can be also applied to the in vitro reconstituted reactions. Further development of cryogenic light microscopy towards single-molecule fluorescence-based techniques (super-resolution microscopy, FRET, *etc.*) can provide a link between structural data and biophysical and biochemical assays.

In the future, electron microscopy will move towards being a multifunctional tool of cell biologists. EM can deliver an integrated view of the crowded cellular environment. Improvement of throughput and automation of imaging

and image processing workflow can make electron microscopy of plastic embedded specimens a versatile screening tool. The wide introduction of correlative microscopy at cryogenic conditions can provide a valuable link between *in vitro* assays and data obtained *in situ*. Finally, the field of the *in situ* structural biology will continue to develop. The introduction of the direct electron detectors revolutionized structural studies done by electron microscopy. New detectors with even higher contrast, combined with FIB-milling, electron tomography, and phase plate technology, will allow localizing and characterizing smaller molecules in the crowded cellular environment. New conformations and cofactors can be described and analyzed within the cellular context. Further improvements that will help to broaden the application of electron microscopy methods are automation of sample preparation, microscope alignment, and image processing. The introduction of new instrumentation, software and workflows bridging different techniques will help biologists to build an integrated molecular model of the cell with unprecedented resolution.

List of Figures

Fig. 1.1. EM sample preparation workflow with various strategies for LM incorporation……**12**

Fig. 2.1. Electron microscopy sample preparation workflow and its limitations……**28**

Fig. 2.2. Correlative light and electron microscopy with our fluorescent barcoding workflow……**29**

Fig. 2.3. Barcodes imaged by light microscopy……**33**

Fig. 2.4. Image processing and correlation workflow……**40**

Fig. 2.5. Image processing for cell and barcode identification……**41**

Fig. 2.6. Barcode determination and verification……**42**

Fig. 2.7. A gallery of yeast cell sections from different strains and experimental conditions……**44**

Fig. 2.8. Abnormal mitochondria phenotype in the SFB2 strain……**45**

Fig. 2.9. Multivesicular body ultrastructure variation……**46**

Fig. 2.10. Quantitative analysis of MVB morphology……**48**

Fig. 3.1. Overview of the endosome maturation process based on yeast data……**62**

Fig. 3.2. Correlative light microscopy and electron tomography of Vps4-EGFP……**70**

Fig. 3.3. Contacts made by MVBs……**71**

Fig. 3.4. Morphology of MVB membrane buds and ILVs……**72**

Fig. 3.5. Quantification of 3D-modelled MVB parameters……**73**

Fig. 3.6. Geometrical model of MVB maturation……**75**

Fig. 3.7. Possible maturation routes of yeast endosomes……**79**

Fig. 4.1. COPI vesicle lifecycle and open questions……**85**

Fig. 4.2. The morphology of the *Chlamydomonas* Golgi apparatus and transport vesicles revealed by cryo-FIB and cryo-ET……**87**

Fig. 4.3. *De novo* termination of the COPI coat structure……**89**

Fig. 4.4. *In situ* COPI coat structure compared to *in vitro* structures……**90**

Fig. 4.5. COPI coat arrangement on vesicles and buds, and triad linkages……**92**

Fig. 4.6. Examples of coated and uncoated vesicles from five Golgi stacks……**94**

Fig. 4.7. Ranked plot of vesicle completeness as representation of uncoating process……**95**

Fig. 4.8. Comparison of the structures derived from buds and from vesicles……**96**

Fig. 4.9. Bud and vesicle morphology variation across the Golgi stack……..**98**

Fig. 4.10. COPI coat structure variability within the Golgi apparatus……..**99**

Fig. 4.11. Changes in membrane bilayer leaflet separation in COPI averages from different Golgi regions……..**100**

Fig. 4.12. Membrane bilayer separation change in COPI buds on cisternae with different morphologies……..**101**

Fig. 4.13. Membrane bilayer separation of uncoated Golgi membranes……**102**

Fig. 5.1. Application of cryo-CLEM to identify endocytic vesicles in a crude preparation of cellular vesicles……..**117**

List of Tables

Table 2.1. List of fluorescent dyes tested for labeling of yeast organelles……**32**

Table 2.2. An example of intermediate 5× con a stocks composition……..**37**

Table 2.3. Combinatorial mixing of the working staining solutions……..**37**

Table 2.4. A scheme of staining of a 24-well plate with the working solutions of combinatorial labels……..**37**

Table 2.5. Yeast strains used in this work and their characteristics……..**52**

Table 2.6. Freeze-substitution and Lowicryl HM20 embedding protocol for the Leica AFS2 machine used in this study……..**55**

Table 2.7. Fluorescent microscopes and filters used in this study……..**55**

Table 3.1. Statistics of the CLEM dataset……..**69**

List of publications

I. Bykov, Y.S., M. Cortese, J.A.G. Briggs, and R. Bartenschlager. 2016. Correlative light and electron microscopy methods for the study of virus–cell interactions. *FEBS Lett.* 590:1877–1895. doi:10.1002/1873-3468.12153.

My contribution to this paper was writing the part reviewing CLEM methods. This part was included in the Chapter 1 of this thesis. The formal permission was obtained from Wiley and Sons (license number 4187230475800).

II. Bertipaglia, C., S. Schneider, A.J. Jakobi, A.K. Tarafder, Y.S. Bykov, A. Picco, W. Kukulski, J. Kosinski, W.J. Hagen, A.C. Ravichandran, M. Wilmanns, M. Kaksonen, J.A. Briggs, and C. Sachse. 2016. Higher-order assemblies of oligomeric cargo receptor complexes form the membrane scaffold of the Cvt vesicle. *EMBO Rep*. 17:1044–1060. doi:10.15252/embr.201541960.

My contribution to this paper was performing a CLEM experiment with plastic embedded sample, analyzing the data and writing part of the manuscript. These results were not included in this thesis.

III. Schorb, M., L. Gaechter, O. Avinoam, F. Sieckmann, M. Clarke, C. Bebeacua, Y.S. Bykov, A.F.-P. Sonnen, R. Lihl, and J.A.G. Briggs. 2017. New hardware and workflows for semi-automated correlative cryo-fluorescence and cryo-electron microscopy/tomography. *J. Struct. Biol.* 197:83–93. doi:10.1016/j.jsb.2016.06.020.

My contribution to this paper was the participation in cryo-CLEM protocol testing and performing test experiments with vitreous sections of yeast cells. The results are not included in this thesis.

The following manuscripts were submitted and were undergoing review process at time of this thesis completion:

Adell, M.A.Y., S. M. Migliano, S. Upadhyayula, Y.S. Bykov, S. Spenger, M. Pakdel, G.F. Vogel, G. Jih, W. Skillern, M. Babst, O. Schmidt, M.W. Hess, J.A.G. Briggs, T. Kirchhausen, and D. Teis. 2017. Recruitment dynamics of ESCRT-III and Vps4 to endosomes and implications for reverse membrane budding.

My contribution was performing CLEM experiments, analyzing and interpreting the data, and writing part of the manuscript. The results and detailed description of my contribution is included in Chapter 3.

Bykov, Y.S., M. Schaffer M., S.O. Dodonova, S. Albert, J.M. Plitzko, W. Baumeister, B.D. Engel, and J.A.G. Briggs. 2017. The structure of the COPI coat determined within the cell.

My contribution was performing subtomogram averaging, data analysis and interpretation, and writing the manuscript. The results and detailed description of my contribution is described in Chapter 4 of this thesis.

The results described in Chapter 2 will form the basis of the manuscript "High-throughput correlative microscopy of budding yeast by fluorescent barcoding" which is currently under preparation.

References

Adell, M. A. Y., Vogel, G. F., Pakdel, M., Müller, M., Lindner, H., Hess, M. W., and Teis, D. (2014). Coordinated binding of Vps4 to ESCRT-III drives membrane neck constriction during MVB vesicle formation. J. Cell Biol. 205, 33–49.

Adrian, M., Dubochet, J., Lepault, J., and McDowall, a W. (1984). Cryo-electron microscopy of viruses. Nature *308*, 32–36.

Al-Amoudi, A., Chang, J.-J., Leforestier, A., McDowall, A., Salamin, L. M., Norlén, L. P. O., Richter, K., Blanc, N. S., Studer, D., and Dubochet, J. (2004). Cryo-electron microscopy of vitreous sections. EMBO J. *23*, 3583–3588.

Al-Amoudi, A., Dubochet, J., and Studer, D. (2002). Amorphous solid water produced by cryosectioning of crystalline ice at 113 K. J. Microsc. *207*, 146–153.

Al-Amoudi, A., Studer, D., and Dubochet, J. (2005). Cutting artefacts and cutting process in vitreous sections for cryo-electron microscopy. J. Struct. Biol. *150*, 109–121.

Arakel, E. C., Richter, K. P., Clancy, A., and Schwappach, B. (2016). δ-COP contains a helix C-terminal to its longin domain key to COPI dynamics and function. Proc. Natl. Acad. Sci. *113*, 6916–6921.

Arlt, H., Auffarth, K., Kurre, R., Lisse, D., Piehler, J., and Ungermann, C. (2015). Spatiotemporal dynamics of membrane remodeling and fusion proteins during endocytic transport. Mol. Biol. Cell *26*, 1357–1370.

Asano, S., Engel, B. D., and Baumeister, W. (2015a). In situ cryo-electron tomography: A post-reductionist approach to structural biology. J. Mol. Biol., 1–12.

Asano, S., Fukuda, Y., Beck, F., Aufderheide, A., Forster, F., Danev, R., and Baumeister, W. (2015b). A molecular census of 26S proteasomes in intact neurons. Science (80-.). *347*, 439–442.

Babst, M., Katzmann, D. J., Snyder, W. B., Wendland, B., and Emr, S. D. (2002). Endosome-associated complex, ESCRT-II, recruits transport machinery for protein sorting at the multivesicular body. Dev. Cell *3*, 283–289.

Babst, M., Sato, T. K., Banta, L. M., and Emr, S. D. (1997). Endosomal transport

function in yeast requires a novel AAA-type ATPase, Vps4p. EMBO J. *16*, 1820–1831.

Balderhaar, H. J. k., and Ungermann, C. (2013). CORVET and HOPS tethering complexes - coordinators of endosome and lysosome fusion. J. Cell Sci. *126*, 1307–1316.

Barr, F., and Lambright, D. G. (2010). Rab GEFs and GAPs. Curr. Opin. Cell Biol. *22*, 461–470.

Beck, M. *et al.* (2016). Cryo-Electron Tomography: Can it Reveal the Molecular Sociology of Cells in Atomic Detail? Trends Cell Biol. *0*, 291–294.

Beck, R., Ravet, M., Wieland, F. T., and Cassel, D. (2009). The COPI system : Molecular mechanisms and function. FEBS Lett. *583*, 2701–2709.

Betzig, E., Patterson, G. H., Sougrat, R., Lindwasser, O. W., Olenych, S., Bonifacino, J. S., Davidson, M. W., Lippincott-Schwartz, J., and Hess, H. F. (2006). Imaging Intracellular Fluorescent Proteins at Nanometer Resolution. Science (80-.). *313*, 1642–1645.

Bonifacino, J. S., and Glick, B. S. (2004). The mechanisms of vesicle budding and fusion. Cell *116*, 153–166.

Bouchet-Marquis, C., Starkuviene, V., and Grabenbauer, M. (2008). Golgi apparatus studied in vitreous sections. J. Microsc. *230*, 308–316.

Bowers, K., and Stevens, T. H. (2005). Protein transport from the late Golgi to the vacuole in the yeast Saccharomyces cerevisiae. Biochim. Biophys. Acta - Mol. Cell Res. *1744*, 438–454.

Bozzola, J. J. (2014). Conventional Specimen Preparation Techniques for Transmission Electron Microscopy of Cultured Cells. In: Electron Microscopy, 1–19.

Braet, F., Cheng, D., Huynh, M., Henriquez, J., Shami, G., and Lampe, M. (2014). Combining Wide-Field Super-Resolution Microscopy and Electron Tomography, Elsevier Inc.

Breker, M., Gymrek, M., Moldavski, O., and Schuldiner, M. (2014). LoQAtE - Localization and Quantitation ATlas of the yeast proteomE. A new tool for multiparametric dissection of single-protein behavior in response to biological perturbations in yeast. Nucleic Acids Res. *42*, 1–5.

Briegel, A., Chen, S., Koster, A. J., Plitzko, J. M., Schwartz, C. L., and Jensen, G. J. (2010). Correlated Light and Electron Cryo-Microscopy. In: Methods in Enzymology, 317–341.

Briggs, J. A. G. (2013). Structural biology in situ-the potential of subtomogram averaging. Curr. Opin. Struct. Biol. *23*, 261–267.

Brügger, B., Sandhoff, R., Wegehingel, S., Gorgas, K., Malsam, J., Helms, J. B., Lehmann, W. D., Nickel, W., and Wieland, F. T. (2000). Evidence for segregation of sphingomyelin and cholesterol during formation of COPI-coated vesicles. J. Cell Biol. *151*, 507–517.

Bykov, Y. S., Cortese, M., Briggs, J. A. G., and Bartenschlager, R. (2016). Correlative light and electron microscopy methods for the study of virus–cell interactions. FEBS Lett. *590*, 1877–1895.

Cabrera, M., Arlt, H., Epp, N., Lachmann, J., Griffith, J., Perz, A., Reggiori, F., and Ungermann, C. (2013). Functional separation of endosomal fusion factors and the class C core vacuole/endosome tethering (corvet) complex in endosome biogenesis. J. Biol. Chem. *288*, 5166–5175.

Cardona, A., Saalfeld, S., Schindelin, J., Arganda-Carreras, I., Preibisch, S., Longair, M., Tomancak, P., Hartenstein, V., and Douglas, R. J. (2012). TrakEM2 Software for Neural Circuit Reconstruction. PLoS One *7*, e38011.

Chan, Y.-H. M., and Marshall, W. F. (2012). How cells know the size of their organelles. Science *337*, 1186–1189.

Chang, Y.-W., Chen, S., Tocheva, E. I., Treuner-Lange, A., Löbach, S., Søgaard-Andersen, L., and Jensen, G. J. (2014). Correlated cryogenic photoactivated localization microscopy and cryo-electron tomography. Nat. Methods *11*, 737–739.

Chen, S., McMullan, G., Faruqi, A. R., Murshudov, G. N., Short, J. M., Scheres, S. H. W., and Henderson, R. (2013). High-resolution noise substitution to measure overfitting and validate resolution in 3D structure determination by single particle electron cryomicroscopy. Ultramicroscopy *135*, 24–35.

Cherfils, J., and Zeghouf, M. (2013). Regulation of small GTPases by GEFs, GAPs, and GDIs. Physiol. Rev. *93*, 269–309.

Chudakov, D. M., Matz, M. V, Lukyanov, S., and Lukyanov, K. A. (2010). Fluorescent proteins and their applications in imaging living cells and tissues. Physiol. Rev. *90*, 1103–1163.

Cohen, Y., and Schuldiner, M. (2011). Advanced Methods for High-Throughput Microscopy Screening of Genetically Modified Yeast Libraries. ed. G. Cagney, and ed. A. Emili, Totowa, NJ: Humana Press, 127–159.

Collinet, C. *et al.* (2010). Systems survey of endocytosis by multiparametric image analysis. Nature *464*, 243–249.

Contento, A. L., and Bassham, D. C. (2012). Structure and function of endosomes in plant cells. J. Cell Sci. *125*, 3511–3518.

Day, K. J., Staehelin, L. A., and Glick, B. S. (2013). A three-stage model of Golgi structure and function. Histochem. Cell Biol. *140*, 239–249.

Denk, W., and Horstmann, H. (2004). Serial Block-Face Scanning Electron Microscopy to Reconstruct Three-Dimensional Tissue Nanostructure. PLoS Biol. *2*, e329.

Devos, D., Dokudovskaya, S., Alber, F., Williams, R., Chait, B. T., Sali, A., and Rout, M. P. (2004). Components of coated vesicles and nuclear pore complexes share a common molecular architecture. PLoS Biol. *2*, e380.

Dodonova, S. O., Appen, A. Von, Hagen, W. J. H., Beck, R., Beck, M., Wieland, F., and Briggs, J. A. G. (2015). A structure of the COPI coat and the role of coat

proteins in membrane vesicle assembly. Science *349*, 195–198.

Donohoe, B. S., Kang, B.-H., and Staehelin, L. A. (2007). Identification and characterization of COPIa- and COPIb-type vesicle classes associated with plant and algal Golgi. Proc. Natl. Acad. Sci. U. S. A. *104*, 163–168.

Donohoe, B. S., Kang, B. H., Gerl, M. J., Gergely, Z. R., Mcmichael, C. M., Bednarek, S. Y., and Staehelin, L. A. (2013). Cis-Golgi Cisternal Assembly and Biosynthetic Activation Occur Sequentially in Plants and Algae. Traffic *14*, 551–567.

Dubochet, J., Zuber, B., Eltsov, M., Bouchet-Marquis, C., Al-Amoudi, A., and Livolant, F. (2007). How to "Read" a Vitreous Section. Methods Cell Biol. *2007*, 385–406.

Engel, B. D., Schaffer, M., Albert, S., Asano, S., Plitzko, J. M., and Baumeister, W. (2015). In situ structural analysis of Golgi intracisternal protein arrays. Proc. Natl. Acad. Sci. *112*, 201515337.

Faini, M., Prinz, S., Beck, R., Schorb, M., Riches, J. D., Bacia, K., Brugger, B., Wieland, F. T., and Briggs, J. A. G. (2012). The Structures of COPI-Coated Vesicles Reveal Alternate Coatomer Conformations and Interactions. Science (80-.). *336*, 1451–1454.

Förster, F., Medalia, O., Zauberman, N., Baumeister, W., and Fass, D. (2005). Retrovirus envelope protein complex structure in situ studied by cryo-electron tomography. Proc. Natl. Acad. Sci. U. S. A. *102*, 4729–4734.

Frankl, A., Mari, M., and Reggiori, F. (2015). Electron microscopy for ultrastructural analysis and protein localization in Saccharomyces cerevisiae. Microb. Cell, 1–17.

Fukaminato, T. (2011). Single-molecule fluorescence photoswitching: Design and synthesis of photoswitchable fluorescent molecules. J. Photochem. Photobiol. C Photochem. Rev. *12*, 177–208.

Gallone, B. *et al.* (2016). Domestication and Divergence of Saccharomyces cerevisiae Beer Yeasts. Cell *166*, 1397–1410.e16.

Gan, L., and Jensen, G. J. (2012). Electron tomography of cells. Q. Rev. Biophys. *45*, 27–56.

Gary, J. D., Wurmser, A. E., Bonangelino, C. J., Weisman, L. S., and Emr, S. D. (1998). Fab1p is essential for PtdIns(3)P 5-kinase activity and the maintenance of vacuolar size and membrane homeostasis. J. Cell Biol. *143*, 65–79.

Ghaemmaghami, S., Huh, W.-K., Bower, K., Howson, R. W., Belle, A., Dephoure, N., O'Shea, E. K., and Weissman, J. S. (2003). Global analysis of protein expression in yeast. Nature *425*, 737–741.

Giaever, G. *et al.* (2002). Functional profiling of the Saccharomyces cerevisiae genome. Nature *418*, 387–391.

Giaever, G., and Nislow, C. (2014). The Yeast Deletion Collection: A Decade of Functional Genomics. Genetics *197*, 451–465.

Glick, B. S., and Nakano, A. (2009). Membrane traffic within the Golgi apparatus. Annu. Rev. Cell Dev. Biol. *25*, 113–132.

Grant, T., and Grigorieff, N. (2015). Measuring the optimal exposure for single particle cryo-EM using a 2.6 Å reconstruction of rotavirus VP6. Elife *4*, e06980.

Griffith, J., and Reggiori, F. (2009). Ultrastructural analysis of nanogold-labeled endocytic compartments of yeast Saccharomyces cerevisiae using a cryosectioning procedure. J. Histochem. Cytochem. *57*, 801–809.

Griffiths, G. (1993). Fine Structure Immunocytochemistry, Berlin, Heidelberg: Springer Berlin Heidelberg.

Le Gros, M. a., McDermott, G., Uchida, M., Knoechel, C. G., and Larabell, C. a. (2009). High-aperture cryogenic light microscopy. J. Microsc. *235*, 1–8.

Gruska, M., Medalia, O., Baumeister, W., and Leis, A. (2008). Electron tomography of vitreous sections from cultured mammalian cells. J. Struct. Biol. *161*, 384–392.

Ha, T., and Tinnefeld, P. (2012). Photophysics of fluorescent probes for single-molecule biophysics and super-resolution imaging. Annu. Rev. Phys. Chem. *63*, 595–617.

Hanson, P. I., and Cashikar, A. (2012). Multivesicular body morphogenesis. Annu. Rev. Cell Dev. Biol. *28*, 337–362.

Harapin, J., Börmel, M., Sapra, K. T., Brunner, D., Kaech, A., and Medalia, O. (2015). Structural analysis of multicellular organisms with cryo-electron tomography. Nat. Methods *12*, 634–636.

Hayles, M. F., de Winter, D. A. M., Schneijdenberg, C., Meeldijk, J. D., Luecken, U., Persoon, H., de Water, J., de Jong, F., Humbel, B. M., and Verkleij, A. J. (2010). The making of frozen-hydrated, vitreous lamellas from cells for cryo-electron microscopy. J. Struct. Biol. *172*, 180–190.

Hayworth, K., Kasthuri, N., Schalek, R., and Lichtman, J. (2006). Automating the Collection of Ultrathin Serial Sections for Large Volume TEM Reconstructions. Microsc. Microanal. *12*, 86–87.

He, S., and Scheres, S. H. W. (2016). Helical reconstruction in RELION. J. Struct. Biol., 1–27.

Hellström, K., Vihinen, H., Kallio, K., Jokitalo, E., and Ahola, T. (2015). Correlative light and electron microscopy enables viral replication studies at the ultrastructural level. Methods *90*, 49–56.

Henne, W. M., Buchkovich, N. J., and Emr, S. D. (2011). The ESCRT Pathway. Dev. Cell *21*, 77–91.

Heymann, J. A. W., Hayles, M., Gestmann, I., Giannuzzi, L. A., Lich, B., and Subramaniam, S. (2006). Site-specific 3D imaging of cells and tissues with a dual beam microscope. J. Struct. Biol. *155*, 63–73.

Heymann, J. a W., Shi, D., Kim, S., Bliss, D., Milne, J. L. S., and Subramaniam, S.

(2009). 3D Imaging of mammalian cells with ion-abrasion scanning electron microscopy. J. Struct. Biol. *166*, 1–7.

Hohmann, S., Krantz, M., and Nordlander, B. (2007). Yeast Osmoregulation, Elsevier Masson SAS.

Howard, C. V., and Reed, M. G. (2005). Unbiased Stereology, Garland Science/BIOS scientific publishers.

Hsia, K.-C., and Hoelz, A. (2010). Crystal structure of alpha-COP in complex with epsilon-COP provides insight into the architecture of the COPI vesicular coat. Proc. Natl. Acad. Sci. U. S. A. *107*, 11271–11276.

Hsu, V. W., Lee, S. Y., and Yang, J.-S. (2009). The evolving understanding of COPI vesicle formation. Nat. Rev. Mol. Cell Biol. *10*, 360–364.

Huh, W.-K., Falvo, J. V, Gerke, L. C., Carroll, A. S., Howson, R. W., Weissman, J. S., and O'Shea, E. K. (2003). Global analysis of protein localization in budding yeast. Nature *425*, 686–691.

Huotari, J., and Helenius, A. (2011). Endosome maturation. EMBO J. *30*, 3481–3500.

Hutagalung, A., and Novick, P. (2011). Role of Rab GTPases in Membrane Traffic and Cell Physiology. Physiol. Rev. *25*, 414–419.

Jackson, L. P. (2014). Structure and mechanism of COPI vesicle biogenesis. Curr. Opin. Cell Biol. *29*, 67–73.

Jackson, L. P., Lewis, M., Kent, H. M., Edeling, M. A., Evans, P. R., Duden, R., and Owen, D. J. (2012). Molecular Basis for Recognition of Dilysine Trafficking Motifs by COPI. Dev. Cell *23*, 1255–1262.

Jahn, R., and Scheller, R. H. (2006). SNAREs--engines for membrane fusion. Nat. Rev. Mol. Cell Biol. *7*, 631–643.

Johnson, E., Seiradake, E., Jones, E. Y., Davis, I., Grünewald, K., and Kaufmann, R. (2015). Correlative in-resin super-resolution and electron microscopy using standard fluorescent proteins. Sci. Rep. *5*, 9583.

Karreman, M. A., Mercier, L., Schieber, N. L., and Solecki, G. (2015). Fast and precise targeting of single tumor cells in vivo by multimodal correlative microscopy.

Karreman, M. a, Mercier, L., Schieber, N. L., Shibue, T., Schwab, Y., and Goetz, J. G. (2014). Correlating intravital multi-photon microscopy to 3D electron microscopy of invading tumor cells using anatomical reference points. PLoS One *9*, e114448.

Katzmann, D. J., Babst, M., and Emr, S. D. (2001). Ubiquitin-dependent sorting into the multivesicular body pathway requires the function of a conserved endosomal protein sorting complex, ESCRT-I. Cell *106*, 145–155.

Katzmann, D. J., Stefan, C. J., Babst, M., and Emr, S. D. (2003). Vps27 recruits ESCRT machinery to endosomes during MVB sorting. J. Cell Biol. *162*, 413–423.

Kaufmann, R., Hagen, C., and Grünewald, K. (2014). Fluorescence cryo-microscopy: current challenges and prospects. Curr. Opin. Chem. Biol. *20C*, 86–91.

Kobayashi, K., Cheng, D., Huynh, M., Ratinac, K. R., Thordarson, P., and Braet, F. (2012). Imaging Fluorescently Labeled Complexes by Means of Multidimensional Correlative Light and Transmission Electron Microscopy: Practical Considerations. In: Methods in Cell Biology, Elsevier, 1–20.

Kolotuev, I., Bumbarger, D. J., Labouesse, M., and Schwab, Y. (2012). Targeted Ultramicrotomy. In: BS:MCB, Elsevier, 203–222.

Kopek, B. G., Shtengel, G., Xu, C. S., Clayton, D. A., and Hess, H. F. (2012). Correlative 3D superresolution fluorescence and electron microscopy reveal the relationship of mitochondrial nucleoids to membranes. Proc. Natl. Acad. Sci. *109*, 6136–6141.

Kozankiewicz, B., and Orrit, M. (2014). Single-molecule photophysics, from cryogenic to ambient conditions. Chem. Soc. Rev. *43*, 1029–1043.

Kremer, J. R., Mastronarde, D. N., and McIntosh, J. R. (1996). Computer visualization of three-dimensional image data using IMOD. J. Struct. Biol. *116*, 71–76.

Krutzik, P. O., and Nolan, G. P. (2006). Fluorescent cell barcoding in flow cytometry allows high-throughput drug screening and signaling profiling. Nat. Methods *3*, 361–368.

Kukulski, W., Schorb, M., Kaksonen, M., and Briggs, J. a G. (2012a). Plasma membrane reshaping during endocytosis is revealed by time-resolved electron tomography. Cell *150*, 508–520.

Kukulski, W., Schorb, M., Welsch, S., Picco, A., Kaksonen, M., and Briggs, J. a G. (2011). Correlated fluorescence and 3D electron microscopy with high sensitivity and spatial precision. J. Cell Biol. *192*, 111–119.

Kukulski, W., Schorb, M., Welsch, S., Picco, A., Kaksonen, M., and Briggs, J. a G. (2012b). Precise, correlated fluorescence microscopy and electron tomography of lowicryl sections using fluorescent fiducial markers. Methods Cell Biol. *111*, 235–257.

Ladinsky, M. S. (2010). Micromanipulator-assisted vitreous cryosectioning and sample preparation by high-pressure freezing, Elsevier Masson SAS.

Lanoix, J., Ouwendijk, J., Stark, A., Szafer, E., Cassel, D., Dejgaard, K., Weiss, M., and Nilsson, T. (2001). Sorting of Golgi resident proteins into different subpopulations of COPI vesicles: A role for ArfGAP1. J. Cell Biol. *155*, 1199–1212.

Lavieu, G., Zheng, H., and Rothman, J. E. (2013). Stapled Golgi cisternae remain in place as cargo passes through the stack. Elife *2013*, 1–19.

Lee, C., and Goldberg, J. (2010). Structure of Coatomer Cage Proteins and the Relationship among COPI, COPII, and Clathrin Vesicle Coats. Cell *142*, 123–132.

Lee, Y. M., Kim, E., An, J., Lee, Y., Choi, E., Choi, W., Moon, E., and Kim, W. (2017). Dissection of the HOG pathway activated by hydrogen peroxide in Saccharomyces cerevisiae. Environ. Microbiol. *19*, 584–597.

Letourneur, F., Gaynor, E. C., Hennecke, S., Démollière, C., Duden, R., Emr, S. D., Riezman, H., and Cosson, P. (1994). Coatomer is essential for retrieval of dilysine-tagged proteins to the endoplasmic reticulum. Cell *79*, 1199–1207.

Leunissen, J. L. M., and Yi, H. (2009). Self-pressurized rapid freezing (SPRF): A novel cryofixation method for specimen preparation in electron microscopy. J. Microsc. *235*, 25–35.

Liu, B. *et al.* (2015). Three-dimensional super-resolution protein localization correlated with vitrified cellular context. Sci. Rep. *5*, 13017.

Livet, J., Weissman, T. A., Kang, H., Draft, R. W., Lu, J., Bennis, R. A., Sanes, J. R., and Lichtman, J. W. (2007). Transgenic strategies for combinatorial expression of fluorescent proteins in the nervous system. Nature *450*, 56–62.

Lucas, M. S., Guenthert, M., Gasser, P., Lucas, F., and Wepf, R. (2014). Correlative 3D imaging: CLSM and FIB-SEM tomography using high-pressure frozen, freeze-substituted biological samples. Methods Mol. Biol. *1117*, 593–616.

Lučić, V., Förster, F., and Baumeister, W. (2005). STRUCTURAL STUDIES BY ELECTRON TOMOGRAPHY: From Cells to Molecules. Annu. Rev. Biochem. *74*, 833–865.

Lunev, S., Semmelink, M. F. W., Xian, J. L., Ma, K. Y., Leenders, A. J. A., Dömling, A. S. S., Shtutman, M., and Groves, M. R. (2017). Crystal structure of truncated human coatomer protein complex subunit ζ1 (Copζ1). Acta Crystallogr. Sect. F Struct. Biol. Commun. *73*, 1–8.

Ma, W., and Goldberg, J. (2013). Rules for the recognition of dilysine retrieval motifs by coatomer. EMBO J. *32*, 926–937.

Maco, B., Holtmaat, A., Cantoni, M., Kreshuk, A., Straehle, C. N., Hamprecht, F. a., and Knott, G. W. (2013). Correlative In Vivo 2 Photon and Focused Ion Beam Scanning Electron Microscopy of Cortical Neurons, Elsevier Inc.

Mahamid, J., Pfeffer, S., Schaffer, M., Villa, E., Danev, R., Kuhn Cuellar, L., Forster, F., Hyman, A. A., Plitzko, J. M., and Baumeister, W. (2016). Visualizing the molecular sociology at the HeLa cell nuclear periphery. Science (80-.). *351*, 969–972.

Mahamid, J., Schampers, R., Persoon, H., Hyman, A. A., Baumeister, W., and Plitzko, J. M. (2015). A focused ion beam milling and lift-out approach for site-specific preparation of frozen-hydrated lamellas from multicellular organisms. J. Struct. Biol. *192*, 262–269.

Malhotra, V., Serafini, T., Orci, L., Shepherd, J. C., and Rothman, J. E. (1989). Purification of a novel class of coated vesicles mediating biosynthetic protein transport through the Golgi stack. Cell *58*, 329–336.

Malsam, J., Satoh, A., Pelletier, L., and Warren, G. (2005). Golgin tethers define subpopulations of COPI vesicles. Science *307*, 1095–1098.

de Marco, A., Müller, B., Glass, B., Riches, J. D., Kräusslich, H. G., and Briggs, J. A. G. (2010). Structural analysis of HIV-1 maturation using cryo- electron tomography. PLoS Pathog. *6*.

Mari, M., Geerts, W. J. C., and Reggiori, F. (2014). Immuno- and correlative light microscopy-electron tomography methods for 3D protein localization in yeast. Traffic *15*, 1164–1178.

Mastronarde, D. N. (2005). Automated electron microscope tomography using robust prediction of specimen movements. J. Struct. Biol. *152*, 36–51.

Mattera, R., Yien, C. T., Weissman, A. M., and Bonifacino, J. S. (2006). The Rab5 guanine nucleotide exchange factor Rabex-5 binds ubiquitin (Ub) and functions as a Ub ligase through an atypical Ub-interacting motif and a zinc finger domain. J. Biol. Chem. *281*, 6874–6883.

McDonald, K. (2007). Cryopreparation methods for electron microscopy of selected model systems. Methods Cell Biol. *79*, 23–56.

McDonald, K. L. (2009). A review of high-pressure freezing preparation techniques for correlative light and electron microscopy of the same cells and tissues. J. Microsc. *235*, 273–281.

McDonald, K., Schwarz, H., Müller-Reichert, T., Webb, R., Buser, C., and Morphew, M. (2010). "Tips and tricks" for high-pressure freezing of model systems, Elsevier Inc.

McMullan, G., Faruqi, A. R., Clare, D., and Henderson, R. (2014). Comparison of optimal performance at 300keV of three direct electron detectors for use in low dose electron microscopy. Ultramicroscopy *147*, 156–163.

van Meer, G., Voelker, D. R., and Feigenson, G. W. (2008). Membrane lipids: where they are and how they behave. Nat. Rev. Mol. Cell Biol. *9*, 112–124.

Mierzwa, B. E. *et al.* (2017). Dynamic subunit turnover in ESCRT-III assemblies is regulated by Vps4 to mediate membrane remodelling during cytokinesis. Nat. Cell Biol. *19*, 787–798.

Migliano, S. M. (2017). Molecular mechanism of ESCRT membrane protein degradation and consequences of failure. Medical University Innsbruck.

Mironov, A. A., Sesorova, I. S., Seliverstova, E. V., and Beznoussenko, G. V. (2016). Different Golgi ultrastructure across species and tissues: Implications under functional and pathological conditions, and an attempt at classification. Tissue Cell.

Mitra, K., Ubarretxena-Belandia, I., Taguchi, T., Warren, G., and Engelman, D. M. (2004). Modulation of the bilayer thickness of exocytic pathway membranes by membrane proteins rather than cholesterol. Proc. Natl. Acad. Sci. *101*, 4083–4088.

Moelleken, J. *et al.* (2007). Differential localization of coatomer complex isoforms within the Golgi apparatus. Proc. Natl. Acad. Sci. U. S. A. *104*,

4425–4430.

Moerner, W. E. (1999). Illuminating Single Molecules in Condensed Matter. Science (80-.). *283*, 1670–1676.

Monaghan, P., Perusinghe, N., and Müller, M. (1998). High-pressure freezing for immunocytochemistry. J. Microsc. *192*, 248–258.

Moor, H. (1987). Theory and Practice of High Pressure Freezing. In: Cryotechniques in Biological Electron Microscopy, ed. R. A. Steinbrecht, and ed. K. Zierold, Berlin, Heidelberg: Springer Berlin Heidelberg, 175–191.

Mund, M., Kaplan, C., and Ries, J. (2014). Localization microscopy in yeast. Methods Cell Biol. *123*, 253–271.

Murk, J. L. a N., Posthuma, G., Koster, a. J., Geuze, H. J., Verkleij, a. J., Kleijmeer, M. J., and Humbel, B. M. (2003). Influence of aldehyde fixation on the morphology of endosomes and lysosomes: Quantitative analysis and electron tomography. J. Microsc. *212*, 81–90.

Nickell, S., Förster, F., Linaroudis, A., Del Net, W., Beck, F., Hegerl, R., Baumeister, W., and Plitzko, J. M. (2005). TOM software toolbox: Acquisition and analysis for electron tomography. J. Struct. Biol. *149*, 227–234.

Nickerson, D. P., West, M., Henry, R., and Odorizzi, G. (2010). Regulators of Vps4 ATPase Activity at Endosomes Differentially Influence the Size and Rate of Formation of Intralumenal Vesicles. *21*, 1023–1032.

Nixon, S. J., Webb, R. I., Floetenmeyer, M., Schieber, N., Lo, H. P., and Parton, R. G. (2009). A single method for cryofixation and correlative light, electron microscopy and tomography of zebrafish embryos. Traffic *10*, 131–136.

Nordmann, M., Cabrera, M., Perz, A., Bröcker, C., Ostrowicz, C., Engelbrecht-Vandré, S., and Ungermann, C. (2010). The Mon1-Ccz1 complex is the GEF of the late endosomal Rab7 homolog Ypt7. Curr. Biol. *20*, 1654–1659.

Novo, M. *et al.* (2009). Eukaryote-to-eukaryote gene transfer events revealed by the genome sequence of the wine yeast Saccharomyces cerevisiae EC1118. Proc. Natl. Acad. Sci. U. S. A. *106*, 16333–16338.

Ohya, Y. *et al.* (2005). High-dimensional and large-scale phenotyping of yeast mutants. Proc. Natl. Acad. Sci. U. S. A. *102*, 19015–19020.

Orci, L., Stamnes, M., Ravazzola, M., Amherdt, M., Perrelet, A., Söllner, T. H., and Rothman, J. E. (1997). Bidirectional Transport by Distinct Populations of COPI-Coated Vesicles. Cell *90*, 335–349.

Paez-Segala, M. G. *et al.* (2015). Fixation-resistant photoactivatable fluorescent proteins for CLEM. Nat. Methods *12*, 215–218.

Papanikou, E., and Glick, B. S. (2014). Golgi compartmentation and identity. Curr. Opin. Cell Biol. *29C*, 74–81.

Peddie, C. J., Blight, K., Wilson, E., Melia, C., Marrison, J., Carzaniga, R., Domart, M.-C., O'Toole, P., Larijani, B., and Collinson, L. M. (2014). Correlative and

integrated light and electron microscopy of in-resin GFP fluorescence, used to localise diacylglycerol in mammalian cells. Ultramicroscopy *143*, 3–14.

Peddie, C. J., and Collinson, L. M. (2014). Exploring the third dimension: Volume electron microscopy comes of age. Micron *61*, 9–19.

Pelham, H. R. B. (2002). Insights from yeast endosomes. Curr. Opin. Cell Biol. *14*, 454–462.

Perkovic, M. *et al.* (2014). Correlative Light- and Electron Microscopy with chemical tags. J. Struct. Biol. *186*, 205–213.

Pettersen, E. F., Goddard, T. D., Huang, C. C., Couch, G. S., Greenblatt, D. M., Meng, E. C., and Ferrin, T. E. (2004). UCSF Chimera--a visualization system for exploratory research and analysis. J. Comput. Chem. *25*, 1605–1612.

Piao, H., Maclean Freed, J., and Mayinger, P. (2012). Metabolic Activation of the HOG MAP Kinase Pathway by Snf1/AMPK Regulates Lipid Signaling at the Golgi. Traffic *13*, 1522–1531.

Pierson, J., Fernández, J. J., Bos, E., Amini, S., Gnaegi, H., Vos, M., Bel, B., Adolfsen, F., Carrascosa, J. L., and Peters, P. J. (2010). Improving the technique of vitreous cryo-sectioning for cryo-electron tomography: Electrostatic charging for section attachment and implementation of an anti-contamination glove box. J. Struct. Biol. *169*, 219–225.

Polishchuk, R. S., Polishchuk, E. V., and Luini, A. (2012). Visualizing Live Dynamics and Ultrastructure of Intracellular Organelles with Preembedding Correlative Light-Electron Microscopy, Elsevier.

Popoff, V., Adolf, F., Brugger, B., and Wieland, F. (2011). COPI Budding within the Gogli Stack. Cold Spring Harb. Perspect. Biol., 1–20.

Poteryaev, D., Datta, S., Ackema, K., Zerial, M., and Spang, A. (2010). Identification of the switch in early-to-late endosome transition. Cell *141*, 497–508.

Prescianotto-Baschong, C., and Riezman, H. (1998). Morphology of the Yeast Endocytic Pathway. Mol. Biol. Cell *9*, 173–189.

Prescianotto-Baschong, C., and Riezman, H. (2002). Ordering of compartments in the yeast endocytic pathway. Traffic *3*, 37–49.

Promponas, V. J., Katsani, K. R., Blencowe, B. J., and Ouzounis, C. A. (2016). Sequence evidence for common ancestry of eukaryotic endomembrane coatomers. Sci. Rep. *6*, 22311.

Puchner, E. M., Walter, J. M., Kasper, R., Huang, B., and Lim, W. A. (2013). Counting molecules in single organelles with superresolution microscopy allows tracking of the endosome maturation trajectory. Proc. Natl. Acad. Sci. *110*, 16015–16020.

R Core Team (2013). R: A language and environment for statistical computing.

Raymond, C. K., I, H.-S., Vater, C. A., and Stevens, T. H. (1992). Morphological

classification of the yeast vacuolar protein sorting mutants: evidence for a prevacuolar compartment in class E vps mutants. Mol. Biol. Cell *3*, 1389–1402.

Rieder, C. L., and Bowser, S. S. (1985). Correlative immunofluorescence and electron microscopy on the same section of epon-embedded material. J Histochem Cytochem *33*, 165–171.

Rigort, A., Bauerlein, F. J. B., Villa, E., Eibauer, M., Laugks, T., Baumeister, W., and Plitzko, J. M. (2012a). Focused ion beam micromachining of eukaryotic cells for cryoelectron tomography. Proc. Natl. Acad. Sci. *109*, 4449–4454.

Rigort, A., Villa, E., Bäuerlein, F. J. B., Engel, B. D., and Plitzko, J. M. (2012b). Integrative Approaches for Cellular Cryo-electron Tomography, Elsevier.

Rink, J., Ghigo, E., Kalaidzidis, Y., and Zerial, M. (2005). Rab conversion as a mechanism of progression from early to late endosomes. Cell *122*, 735–749.

Rosenthal, P. B., and Henderson, R. (2003). Optimal determination of particle orientation, absolute hand, and contrast loss in single-particle electron cryomicroscopy. J. Mol. Biol. *333*, 721–745.

Russell, M. R. G., Shideler, T., Nickerson, D. P., West, M., and Odorizzi, G. (2012). Class E compartments form in response to ESCRT dysfunction in yeast due to hyperactivity of the Vps21 Rab GTPase. J. Cell Sci. *125*, 5208–5220.

Schaffer, M., Engel, B. D., Laugks, T., Mahamid, J., Plitzko, J. M., and Baumeister, W. (2015). Cryo-focused Ion Beam Sample Preparation for Imaging Vitreous Cells by Cryo-electron Tomography. Bio-Protocol *5*, 1–12.

Schaffer, M., Mahamid, J., Engel, B. D., Laugks, T., Baumeister, W., and Plitzko, J. M. (2016). Optimized cryo-focused ion beam sample preparation aimed at in situ structural studies of membrane proteins. J. Struct. Biol.

Schaffer, M., Mahamid, J., Engel, B. D., Laugks, T., Baumeister, W., and Plitzko, J. M. (2017). Optimized cryo-focused ion beam sample preparation aimed at in situ structural studies of membrane proteins. J. Struct. Biol. *197*, 73–82.

Schindelin, J. *et al.* (2012). Fiji: an open-source platform for biological-image analysis. Nat. Methods *9*, 676–682.

Schledzewski, K., Brinkmann, H., and Mendel, R. R. (1999). Phylogenetic analysis of components of the eukaryotic vesicle transport system reveals a common origin of adaptor protein complexes 1, 2, and 3 and the F subcomplex of the coatomer COPI. J. Mol. Evol. *48*, 770–778.

Schur, F. K. M., Obr, M., Hagen, W. J. H., Wan, W., Jakobi, A. J., Kirkpatrick, J. M., Sachse, C., Kräusslich, H., and Briggs, J. A. G. (2016). An atomic model of HIV-1 capsid-SP1 reveals structures regulating assembly and maturation. Science *353*, 506–508.

Scott, C. C., Vacca, F., and Gruenberg, J. (2014). Endosome maturation, transport and functions. Semin. Cell Dev. Biol. *31*, 2–10.

Shaner, N. C. *et al.* (2013). A bright monomeric green fluorescent protein derived from Branchiostoma lanceolatum. Nat. Methods *10*, 407–409.

Sharpe, H. J., Stevens, T. J., and Munro, S. (2010). A Comprehensive Comparison of Transmembrane Domains Reveals Organelle-Specific Properties. Cell *142*, 158–169.

Sitte, H., Edelmann, L., and Neumann, K. (1987). Cryofixation Without Pretreatment at Ambient Pressure. In: Cryotechniques in Biological Electron Microscopy, Berlin, Heidelberg: Springer Berlin Heidelberg, 87–113.

Sjollema, K. a, Schnell, U., Kuipers, J., Kalicharan, R., and Giepmans, B. N. G. (2012). Correlated light microscopy and electron microscopy. Methods Cell Biol. *111*, 157–173.

Sochacki, K. a, Shtengel, G., van Engelenburg, S. B., Hess, H. F., and Taraska, J. W. (2014). Correlative super-resolution fluorescence and metal-replica transmission electron microscopy. Nat. Methods *11*, 305–308.

Sommer, C., Straehle, C., Kothe, U., and Hamprecht, F. a (2011). Ilastik: Interactive learning and segmentation toolkit. In: 2011 IEEE International Symposium on Biomedical Imaging: From Nano to Macro, IEEE, 230–233.

Spiegelhalter, C., Laporte, J. F., and Schwab, Y. (2014). Correlative light and electron microscopy: from live cell dynamic to 3D ultrastructure. Methods Mol. Biol. *1117*, 485–501.

Steinbrecht, R. A., and Müller, M. (1987). Freeze-Substitution and Freeze-Drying. In: Cryotechniques in Biological Electron Microscopy, Berlin, Heidelberg: Springer Berlin Heidelberg, 149–172.

Stepanek, L., and Pigino, G. (2016). Microtubule doublets are double-track railways for intraflagellar transport trains. Science (80-.). *352*, 721–724.

Studer, D., Klein, A., Iacovache, I., Gnaegi, H., and Zuber, B. (2014). A new tool based on two micromanipulators facilitates the handling of ultrathin cryosection ribbons. J. Struct. Biol. *185*, 125–128.

Suresh, H. G., da Silveira Dos Santos, A. X., Kukulski, W., Tyedmers, J., Riezman, H., Bukau, B., and Mogk, A. (2015). Prolonged starvation drives reversible sequestration of lipid biosynthetic enzymes and organelle reorganization in Saccharomyces cerevisiae. Mol. Biol. Cell *26*, 1601–1615.

Tokuyasu, K. T. (1973). A Technique for Ultracryotomy of Cell Suspensions and Tissues. J. Cell Biol. *57*, 551–565.

Valm, A. M., Mark Welch, J. L., and Borisy, G. G. (2012). CLASI-FISH: Principles of combinatorial labeling and spectral imaging. Syst. Appl. Microbiol. *35*, 496–502.

Valm, A. M., Mark Welch, J. L., Rieken, C. W., Hasegawa, Y., Sogin, M. L., Oldenbourg, R., Dewhirst, F. E., and Borisy, G. G. (2011). Systems-level analysis of microbial community organization through combinatorial labeling and spectral imaging. Proc. Natl. Acad. Sci. U. S. A. *108*, 4152–4157.

Verkade, P. (2008). Moving EM: The Rapid Transfer System as a new tool for correlative light and electron microscopy and high throughput for high-pressure freezing. J. Microsc. *230*, 317–328.

Villaseñor, R., Nonaka, H., Del Conte-Zerial, P., Kalaidzidis, Y., and Zerial, M. (2015). Regulation of EGFR signal transduction by analogue-to-digital conversion in endosomes. Elife *4*, 1–32.

Wacker, I., and Schroeder, R. R. (2013). Array tomography. J. Microsc. *252*, 93–99.

Walker, J. M. (2014). Electron Microscopy. Methods in Molecular Biology Volume 1117, Totowa, NJ: Humana Press.

Wan, W., and Briggs, J. A. G. (2016). Cryo-Electron Tomography and Subtomogram Averaging. Methods Enzymol. *579*, 329–367.

Watanabe, S., Lehmann, M., Hujber, E., Fetter, R. D., Richards, J., Söhl-Kielczynski, B., Felies, A., Rosenmund, C., Schmoranzer, J., and Jorgensen, E. M. (2014). Nanometer-resolution fluorescence electron microscopy (nano-EM) in cultured cells. Methods Mol. Biol. *1117*, 503–526.

Watanabe, S., Punge, A., Hollopeter, G., Willig, K. I., Hobson, R. J., Davis, M. W., Hell, S. W., and Jorgensen, E. M. (2011). Protein localization in electron micrographs using fluorescence nanoscopy. Nat. Methods *8*, 80–84.

Watson, P. J., Frigerio, G., Collins, B. M., Duden, R., and Owen, D. J. (2004). Gamma-COP appendage domain - structure and function. Traffic *5*, 79–88.

Weimer, C., Beck, R., Eckert, P., Reckmann, I., Moelleken, J., Brügger, B., and Wieland, F. (2008). Differential roles of ArfGAP1, ArfGAP2, and ArfGAP3 in COPI traffi cking. J. Cell Biol. *183*, 725–735.

Weissman, T. A., and Pan, Y. A. (2015). Brainbow: New resources and emerging biological applications for multicolor genetic labeling and analysis. Genetics *199*, 293–306.

White, I. J., Bailey, L. M., Aghakhani, M. R., Moss, S. E., and Futter, C. E. (2006). EGF stimulates annexin 1-dependent inward vesiculation in a multivesicular endosome subpopulation. EMBO J. *25*, 1–12.

Xiong, H. *et al.* (2014). Chemical reactivation of quenched fluorescent protein molecules enables resin-embedded fluorescence microimaging. Nat. Commun. *5*, 3992.

Xiong, Q., Morphew, M. K., Schwartz, C. L., Hoenger, A. H., and Mastronarde, D. N. (2009). CTF determination and correction for low dose tomographic tilt series. J. Struct. Biol. *168*, 378–387.

Yang, J.-S. *et al.* (2011). COPI acts in both vesicular and tubular transport. Nat. Cell Biol. *13*, 996–1003.

Yu, W., Lin, J., Jin, C., and Xia, B. (2009). Solution structure of human zeta-COP: direct evidences for structural similarity between COP I and clathrin-adaptor coats. J. Mol. Biol. *386*, 903–912.

Yu, X., Breitman, M., and Goldberg, J. (2012). A Structure-based mechanism for Arf1-dependent recruitment of coatomer to membranes. Cell *148*, 530–542.

Zeigerer, A. *et al.* (2012). Rab5 is necessary for the biogenesis of the endolysosomal system in vivo. Nature *485*, 465–470.

Acknowledgements

I am grateful to my supervisor John Briggs for his professionalism and patience, and also for giving me a chance to work on a wide variety of projects and learn a lot of things. I also would like to acknowledge other members of my Thesis Advisory Committee, Michael Knop, Anne-Claude Gavin, and Yannick Schwab for their patience and fruitful discussions.

The work described in my thesis required a lot of imaging using fluorescence and electron microscopes. This of course would not be possible without the constant support from the EMBL Core facilities. I would like to thank our Advanced Light Microscopy Facility, and especially Yury Belyaev and Stefan Terjung. The Electron Microscopy Core facility was an absolutely great place to work and I would like to thank Rachel Mellwig, Charlotta Funaya, Pedro Machado, Paolo Ronchi, Androniki Kolovou, Martin Schorb, and Yannick Schwab for creating a supportive and friendly atmosphere.

A lot of experiments and projects would not be possible without our great collaborators. I am grateful to Kiran Patil, Natalia Gabrielli Lopez, Matthias Meurer, and Michael Knop for the yeast strains used for the barcoding projects. Additional thanks to Marko Kaksonen and members of his group, especially Tanja Georg and Hetty Manenschijn for introducing me to the yeast universe. Great thanks to Nir Cohen and Maya Schuldiner for their enthusiasm and support of the barcoding project! I am very grateful to Simona Migliano and David Teis for the exciting collaboration on the Vps4 project. I would like to thank Ben Engel for the great opportunity to work on the *in situ* structure of the COPI coat, for his enthusiasm and great discussions.

I would like to thank all present and former members of the Briggs group. That was a pleasure to work next to such amazing colleagues! Great thanks to Wanda for introducing me to CLEM, thanks to Simone and Mairi for their constant support, thanks to Andreas, Oliver, and the other dwellers of the lab office space. I am grateful to Simo, Flo, Kun and Will for their sense of humor and generous sharing of the subtomogram averaging expertise. Thanks to Cecilia and Ori for the great CLEM discussions and collaborations. I would like to thank Sveta for her wisdom and friendliness, for initiating the collaboration with Ben, and for being the most eager organizer of the lab movie nights. Thanks to Wim for his patience in sharing secrets of EM. I would like to thank Julia and Lauren Ann for the help with German and English, Frank and Olexiy for COPI and clathrin discussions, and Dustin for the EM enthusiasm. Great thanks to all the colleagues at the MRC LMB for their friendly attitude after the big move.

I would like to thank my friends for all the fun and for visiting me once in a while. Rodnenkye are the best! And all course I am grateful to my parents Sergey and Elena, and to my sister Marina for their endless support and love.